305
5-19-81

①

WISC

UC.20-f

UNIVERSITY OF WISCONSIN • MADISON, WISCONSIN

MASTER

PLASMA PHYSICS

R4436

Lh. 2656

PLASMA TRANSPORT IN A SIMULATED MAGNETIC-DIVERTOR CONFIGURATION

Clifford M. Strawitch

DOE/ET/53051-20 March 1981

DISTRIBUTION OF THIS DOCUMENT IS UNLIMITED

NSIN

NOTICE

Printed in the United States of America
Available from
National Technical Information Service
U.S. Department of Commerce
5285 Port Royal Road
Springfield, VA 22161

NTIS Price codes
Printed copy: A14
Microfiche copy: A01

PLASMA TRANSPORT IN A SIMULATED MAGNETIC-DIVERTOR CONFIGURATION

by

CLIFFORD M. STRAWITCH

A thesis submitted in partial fulfillment of the
requirements for the degree of

DOCTOR OF PHILOSOPHY
(Nuclear Engineering)

at the

UNIVERSITY OF WISCONSIN-MADISON

1981

Abstract

PLASMA TRANSPORT IN A SIMULATED MAGNETIC DIVERTOR CONFIGURATION

Clifford M. Strawitch

Under the supervision of Professor G.A. Emmert

The transport properties of plasma on magnetic field lines that intersect a conducting plate are studied experimentally in the Wisconsin internal ring D.C. machine. The magnetic geometry is intended to simulate certain aspects of plasma phenomena that may take place in a tokamak divertor.

It is found by a variety of measurements that the cross field transport is non-ambipolar; this may have important implications in heat loading considerations in tokamak divertors. The undesirable effects of nonambipolar flow make it preferable to be able to eliminate it. However, we find that though the non-ambipolarity may be reduced, it is difficult to eliminate entirely. The plasma flow velocity parallel to the magnetic field is found to be near the ion acoustic velocity in all cases. The experimental density and electron temperature profiles are compared to the solutions to a one dimensional transport model that is commonly used in divertor theory. Solutions to both the steady state density, and time dependent coupled density and temperature equations of this model, agree well with the experimental profiles, for cross field diffusion coefficients that scale like the classical coefficients due to ion-neutral collisions, cross field conductivities that scale like the classical conductivities due to electron-neutral collisions, and parallel loss terms that scale like the ion acoustic velocity. The ion-neutral scaling in the convective term of the electron energy equation is believed to be due to an incomplete "shorting" of the ambipolar electric field by the divertor plate.

G.A. Emmert

ACKNOWLEDGEMENTS

First and foremost, I must thank Professor G.A. Emmert for his expert guidance in my thesis research, and my graduate education in general. He has been both a mentor and a friend. His insights and suggestions, coupled with his encouraging the best that I could give throughout my research, are deeply appreciated.

For the summer that he sat in for G. Emmert as my advisor, I thank Professor D. Kerst for his inspirational guidance.

Professor Max Carbon showed me understanding when I needed it most; for this I thank him sincerely.

For sound advice in turbulent times, I must thank Al Mense.

To my fellow graduate students, I owe one and all a debt of gratitude for many helpful suggestions made. Those that were especially helpful, on matters that were not necessarily technical, are Dave Grubb, Mike Makowski, Jon Twichell, Mike Zarnstorff, Evan Rose, Phil Smith, Ted Strait, Alan Biddle, and Skip Garner for talking me into joining the Karate club.

No thesis would be complete, from plasma physics at the U.W., without thanks to Tom Lovell and Paul Nonn. I thank especially Tom for his invaluable technical assistance throughout my thesis research.

Last and certainly not least important, my warmest thanks to Ann L. Powers for the encouragement, understanding, and assistance she gave me while I was carrying on my research.

I dedicate this thesis to the memory of my mother, Ruth A. Strawitch.

TABLE OF CONTENTS

Chapter 1

Introduction

One of the most pressing problems to be faced in the magnetic controlled thermonuclear fusion program is the control of impurities in the next generation of experiments. Whatever confinement concept that one believes will demonstrate fusion feasibility, it is agreed that its success will rest on the implementation of some concept of impurity control. The effects of impurities on Tokamak discharges has received considerable attention, and the proposed methods to control these impurities are many. Because my purpose is to discuss the properties of one such method of control in Tokamaks, I will limit this brief review to impurities in Tokamaks. However, it should be noted that most of the concepts relating to the effects of impurities and their production mechanisms extend easily to other devices. For a much more detailed review of the effects of impurities on Tokamak discharges, and their production mechanisms, than can be presented here, the interested reader is referred to the excellent review paper by McCracken and Stott.[1]

The Effects of Impurities

Perhaps the most severe effect of impurities in a Tokamak discharge is the greatly enhanced energy loss due to line and bremsstrahlung radiation. The energy radiated due to electron bremsstrahlung is[2]

$$E_{loss} \propto T_e^{1/2} n_e \sum_i n_i Z_i^2, \tag{1.1}$$

and due to line radiation is[2]

$$E_{loss} \propto T_e^{-1/2} n_e \sum_i n_i Z_i^4, \tag{1.2}$$

where the sums extend over all the ion species, T_i is the ion temperature, T_e is the electron temperature, n_i is the ion density, and Z_i is the ion atomic number. These equations for radiative energy loss are strictly applicable for coronal equilibrium only. The problem is greatest for those impurity ions that are not completely stripped of electrons. For example, it has been shown[3] that as little as a .1% concentration of tungsten triples the required $n\tau$ for ignition, where n is the fuel ion density and τ the particle confinement time. An increase to only .2% can preclude ignition altogether. These impurity concentrations are not at all unreasonable because in a typical ignition experiment one can expect a 5% niobium concentration in the plasma from the bombarded walls of the vacuum vessel if the walls had been niobium coated. From equations (1.1) and (1.2), the radiation problem is less severe for low-Z impurities especially if they are fully stripped of electrons in which case, of course, there is no line radiation. However, even for a low-Z impurity like carbon only a few percent is allowable before the same problems occur that occur at high-Z.

Due to an effect predicted by neoclassical transport theory, under the right conditions impurities should be transported to the central section of a Tokamak discharge where they will buildup and do the most damage.[4] Even at the discharge center, high-Z impurities will not be fully stripped. This effect has been observed in many experiments[5,6,7,8] from the T-3 Tokamak[5] to, most recently, the ISX-A experiment[4], but only on the outermost flux surfaces of the discharge. Observations on the ST tokamak show no buildup of impurities in the center of the discharge. Radiation measurements on TFR indicate central impurity peaking would not be consistent with the measured power out of the center of the device. The TFR group postulates that only a small fraction of the inward diffusing impurities in the outer layers actually reaches the center, thus impurity recycling occurs only in the outer layers.[7] At present the question of the inward diffusion of impurities is unresolved. Interestingly enough, this same phenomena may, under properly tailored conditions, provide a method of impurity control. This will be discussed in the section on the control of impurities.

Radiation losses are not the only deleterious effect of impurities on a Tokamak discharge. Even a small concentration of highly stripped ions at the center of a discharge can cause a substantial dilution of the nuclear fuel and a consequent increase in the required $n\tau$. Each highly charged impurity ion can take the place of many fuel ions for a given electron density, resulting in a lower fuel ion density as impurities diffuse inward.[1] Furthermore, radiative cooling of the discharge periphery can cause instabilities with attendant enhanced transport, as well as disruptions due to the shrinking of the current channel.[2]

Solutions to the Impurity Problem

To the many problems posed by the presence of impurities in Tokamak discharges have come a variety of answers. One solution is the use of material limiters to define the plasma shape and prevent contact of the hot plasma with the vacuum walls. At present this seems only to move the source of the impurities from the walls to the limiter. With megawatts of power being deposited on the limiter even in present day experiments, severe heating followed by release of impurities is unavoidable.[1] One proposed compromise is to use low-Z coatings on the limiter so that at least the released impurities will be fully stripped.

Another solution is to surround the plasma with a gas blanket to insulate the vacuum walls from the plasma. A similar solution proposed for the JET Tokamak is a cold plasma blanket that is impermeable to charge exchange neutrals and cold enough to be below the sputtering threshold (i.e.:$10\mathrm{eV}<T_e<20\mathrm{eV}$). As of yet the blanket has only been simulated numerically, and there remain questions on the stability of the blanket-plasma interface.

One imaginative solution to the problem of the neoclassical inward transport of impurities was proposed by Ohkawa of General Atomic.[9] Ohkawa showed that in the Pfirsh-Schluter domain of transport, a poloidally asymmetric source of protons can reduce or even reverse the inward transport of impurities. Subsequently, other authors have generalized the theory to include the effect of asymmetric heat sources, lower collisionality regimes and general flux surface geometries.[4,10,11] Theoretical calculations have shown that in the presence of such poloidally asymmetric sources, the radial flux of impurities Γ_I of charge Z_I is[4]

$$\Gamma_I = K\left(\Delta_I\left\{\frac{1}{n_i}\frac{\partial P_i}{\partial r} - \frac{1}{n_I Z_I}\frac{\partial P_I}{\partial r}\right\} - \frac{5}{2}\Delta_2\frac{\partial T_i}{\partial r} - \frac{1}{2} eB_\phi R\left\{ \Delta_1\frac{a_{i1}}{n_i} - \Delta_2\frac{a_{T1}}{P_i}\right\}\right), \tag{1.3}$$

where

$K=2q^2 n_i/(Z_I e B_\phi\ \omega_{ci}\ \tau_{iI})$.

The subscript i(I) refers to the protons(impurities), q is the safety factor, τ_{iI} is the proton-impurity collision time, ω_{ci} is the proton cyclotron frequency, B_ϕ is the toroidal field, R and r the major and minor radii, e the electron charge, and P the pressure. The Δ's are numerical factors of order unity that depend on the collision model used.[11]

The first term in brackets in equation 1.3 is the neoclassical effect responsible for the inward diffusion of impurities, namely the impurities diffusing up the the gradient of main plasma ion species. The second term is responsible for impurities diffusing down their own density gradient. The last two terms are the proton particle source a_{i1}, and the heat source a_{T1}, and show they can effect the direction and magnitude of the impurity flux. These existence of these terms is responsible for the impurity reversal effect.

A poloidally asymmetric source of H_2 gas was therefore installed on the ISX experiment to test these predictions. Results consistent with the theory were obtained for neon injected as an impurity; the inward diffusion of neon was significantly reduced. Similar tests on aluminum as the injected impurity gave inconsistent results. Various explanations, such as the higher thermal velocities of the injected aluminum, have been advanced for this discrepancy.[12] Higher thermal velocities may allow the aluminum to penetrate the layer where the flow reversal effect exists. Attempts to reproduce these results on ISX-B have not, as of this writing, been successful[13], however it would certainly seem that it merits further study. It remains to be seen if actual reversal of the flow can be induced.

Perhaps the one solution with the most promise is the magnetic divertor. The idea of the divertor is to shift the problem of the plasma-wall interaction away from the main containment vessel to an area that can be better equipped to handle the problems. The device was first proposed in 1951 by Lyman Spitzer[14] as a means of preventing contact between plasma and first wall. Fig. 1.1 shows the Spitzer divertor. However, it was soon realized that the device could screen the plasma from wall evolved impurities as well. Coils external to the plasma create a null in one component of the confining field; from the component that is nulled comes the usual name given to the divertor (i.e.:toroidal or poloidal divertor). Field lines inside the

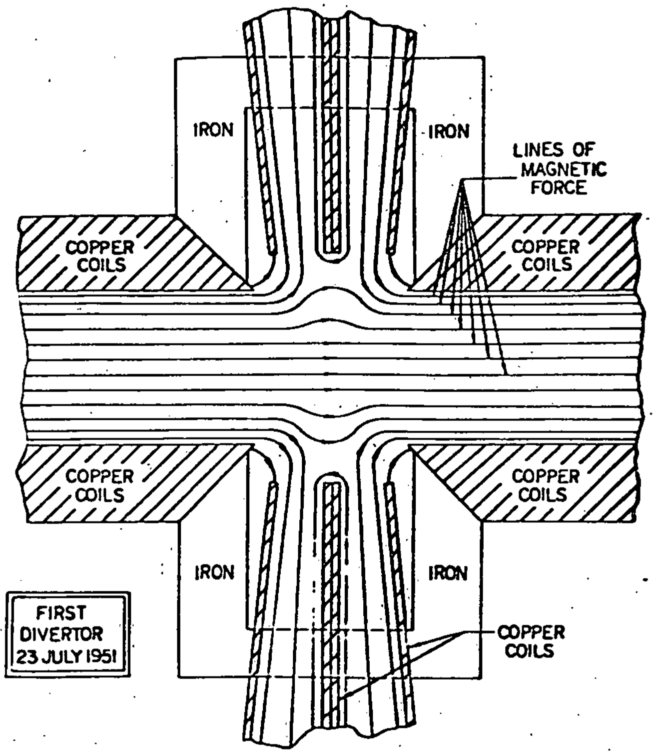

Fig. 1.1 : Schematic representation of the Spitzer divertor.

separatrix remain in the torus, while those outside are conducted to an external chamber with the plasma that is on them (thus the name "scrape-off" zone for these field lines). Fig. 1.1 shows all of these features. Here the plasma is neutralized by allowing it to strike a material plate. Return of the neutralized gas to the main chamber is restricted by reducing the flow conductance. The flow of plasma back to the main discharge may be restricted by ambipolar electric fields.[15] To handle the heat and gas load to the divertor, the neutralizer plate may be cooled and the chamber pumped on by a vacuum pumping system. The heat load per unit area may be reduced by fanning out the field lines with appropriately placed coils. Damage or erosion of the divertor plates may be dealt with by continually refreshing the plate surface by gettering or even mechanical replacement. In all cases one is allowed greater flexibility in handling the plasma wall interaction problem.

The purpose envisioned for divertors then is a threefold one. The first is to be a magnetic limiter that defines the plasma shape. The divertor will not define the plasma edge in the sense that the density will go to zero there, but it will define a boundary layer where the fall off of density and temperature will occur more rapidly than the main discharge. The second function is to take up the plasma flux that would normally hit the first wall and exhaust it to a pumping chamber. The third function is to sweep up wall evolved impurities by the plasma flowing to the divertor and thus prevent them from entering the main discharge. To maximally protect the first wall as in purpose two, one requires a rapid fall off of density to minimize plasma and first wall interaction and its resultant damage and impurity evolution. Purpose three requires a scrape-off layer thick enough to assure a high probability of ionizing an incoming neutral and carrying it to the divertor. Therefore, the last two divertor functions can not be simultaneously optimized and one must settle for some reasonable compromise.[16] Finally the extent to which the divertor can act as a limiter is determined by this tradeoff.

An additional benefit of divertors has been realized. Evacuation of the reaction chamber to the required low pressures will demand presently unattainable pumping speeds. However, if the divertor chamber is designed with a low conductance path to the reaction vessel, the throughput (escaping plasma) can be guided through this low conductance path to the divertor chamber. Thus, in this chamber, higher pressures can be tolerated and maintained with technically feasable pumping speeds.

Divertor Experiments

Shown in Fig. 1.2 is a schematic of the types of divertors that have received experimental attention, and illustrates the salient differences between them. The first experimental test of the divertor was done in 1957 on the B-65 stellarator.[17] This divertor was found to reduce the impurity concentrations by a factor of two to three with an attendant increase in the ion temperature. A divertor was next tested on the model C stellarator in 1963 and found to reduce impurities by an order of magnitude.[18] A major disadvantage of these toroidal

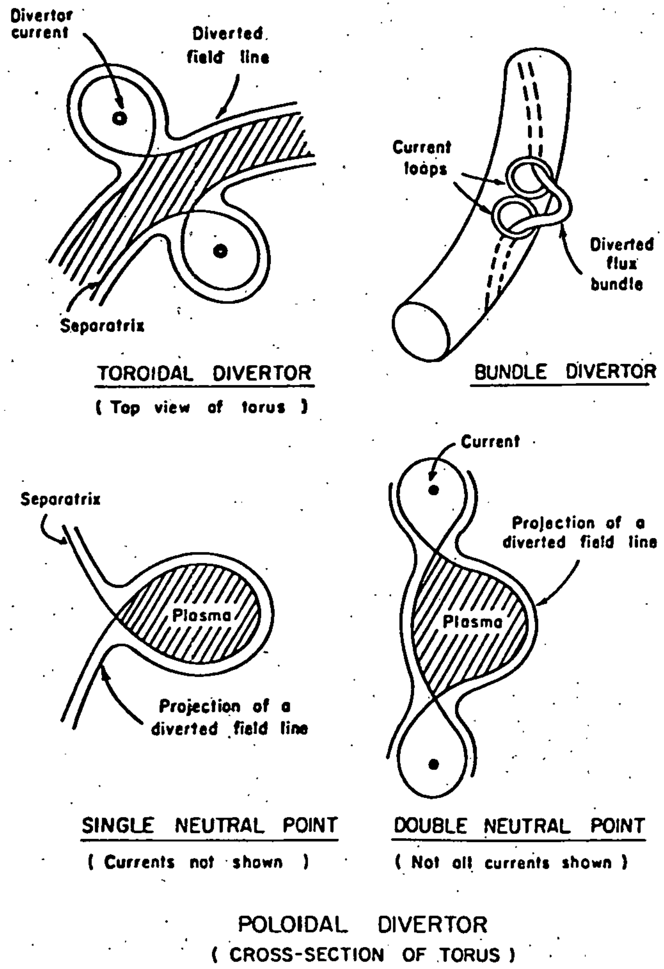

Fig. 1.2: The different types of magnetic divertor that have received experimental attention.

divertors, as with all toroidal divertors, is that they destroy the axisymmetry and cause large field perturbations, both of which can lead to enhanced radial plasma loss.[19,20] Perhaps the sole advantage of a toroidal divertor lies in the fact that it does not require the existence of a plasma current to operate. This point will be expanded upon shortly.

Another divertor of the toroidal type is the so called bundle divertor first reported in the literature in 1972.[21,22] The coils used to divert the "bundle" of toroidal flux are a higher order multipole than those of the above mentioned divertor. As a result the field falls off much faster than in the toroidal case, resulting in magnetic field perturbations on axis of typically a few per cent. In this sense it is an improvement on the toroidal divertor, unfortunately, this device still destroys the toroidal axisymmetry. In addition, to handle the anticipated heat loads in next generation experiments more than one such divertor may be necessary. The first experimental test of the bundle divertor occurred on the D.I.T.E. tokamak and met with encouraging results.[23] The divertor received 50% of the particle flux and 60% of the energy flux that normally hit the walls. The amount of metallic impurities was reduced by a large factor as evidenced by an order of magnitude decrease in the Mo^{+21} radiation and a factor of three reduction in Fe^{+16} radiation. The total radiated power was down by a factor of five to eight. Finally, there is ample evidence of a screening effect from experiments with an injected oxygen impurity.

Figure 1.3 shows a schematic representation of the D.I.T.E. bundle divertor.

A third divertor concept is the poloidal divertor, which was first conceived of in 1956[24] and has received the most attention in recent years. Because the poloidal field in a tokamak is typically a factor of ten smaller than the toroidal field, it follows that the current necessary to drive a poloidal null is smaller than that necessary to drive a toroidal null. Thus the field perturbation problem is smaller. Although the poloidal divertor preserves the axisymmetry of the device, it does require the existence of a plasma current that creates the poloidal field before it can work. It therefore follows that impurities released in the start up phase of a tokamak discharge, before the toroidal current is established, may be free to enter the plasma. A poloidal divertor also differs from a toroidal divertor in the length of a typical field line in the scrape zone before it enters the divertor. In a toroidal divertor a particle is never more than one toroidal circumference away from the pumping chamber. On the other hand, in a poloidal divertor a particle may make several trips around the major axis before being diverted.

The first experimental test of the poloidal divertor occurred on the FM-1 spherator device at the Princeton Plasma Physics Labs. A plasma capture efficiency of 80% was obtained on this device.[25] A poloidal divertor was also tested on the DIVA tokamak.[26] This divertor was found to receive 75% of the energy loss and 33% of the particle loss. The total radiation decreased by a factor of 2 to 4 and

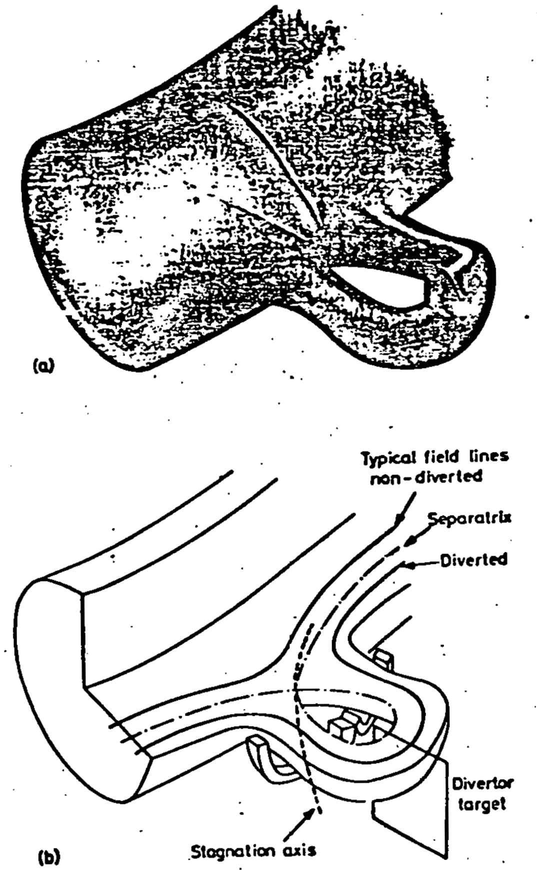

Fig. 1.3: Schematic of the first bundle divertor, as used on the DITE tokamak.

shielding of at least oxygen was observed. The number density of both low and high-Z impurities was decreased by the divertor action.

In the construction and/or initial operation phase are three more large poloidal divertor experiments. PDX at Princeton has begun operation, as has the ASDEX experiment at Garching.[27,28] Initial results from PDX show a significant decrease in the total radiated power over the non-diverted circular case, and a Z_{eff} of one in the diverted case, which is one half that of the circular discharge.[29]

Still another divertor concept was originated here at Wisconsin by D.W. Kerst.[30] It was suggested that an externally applied electric field could be used to produce an $\underline{E}\times\underline{B}$ drift that would augment or initiate plasma flow to the divertor chamber. The existence of this effect was shown in a series of experiments carried out by E. Strait[31] on the large Octupole device. Additionally, an applied electric field in conjunction with a poloidal divertor was demonstrated to reduce the plasma flux to the wall by an extra factor of five from the action of the poloidal divertor alone.

Theories of Divertor Operation

The theoretical problem of plasma transport in a divertor is essentially two dimensional, and the physical processes that govern the cross field and parallel to the magnetic field flow are very different. If one includes the effects of the magnetic geometry the problem is complicated further. The first theoretical attempts to predict such divertor parameters as the density and temperature profiles simplified the problem considerably by adopting a phenomenological approach.[16,32,33] In these analyses the plasma flow into the collectors is modeled by replacing the parallel part of the continuity equation by an "absorption" term, thus reducing the equation to one dimension. Then, depending on one's prejudices about the governing physics in the scrape-off zone, choices are made as to the value of the cross field diffusion coefficient and the form of the parallel "absorption" term. This simple model has proven useful in developing an understanding of the consequences of the various physics assumptions one can make on the operation of a divertor.

As an example, consider a simple slab model divertor as shown in Fig. 1.4. The steady state continuity equation in this geometry, ignoring sources for the moment (a more formal derivation will be given later), can be written as

$$\underline{\nabla}\cdot\underline{\Gamma} = \nabla_\perp\cdot\Gamma_\perp + \nabla_\parallel\cdot\Gamma_\parallel = 0, \tag{1.4}$$

where $_\perp$ and $_\parallel$ refer to x and z in Fig. 1.4. We make the replacement

$$\underline{\nabla}_\parallel\cdot\underline{\Gamma}_\parallel = \Gamma_\parallel/L = nv_\parallel/L = n/\tau_\parallel. \tag{1.5}$$

For the slab model shown in Fig. 1.4

$$\nabla_\perp\cdot\underline{\Gamma}_\perp = \frac{\partial}{\partial x}\Gamma_x. \tag{1.6}$$

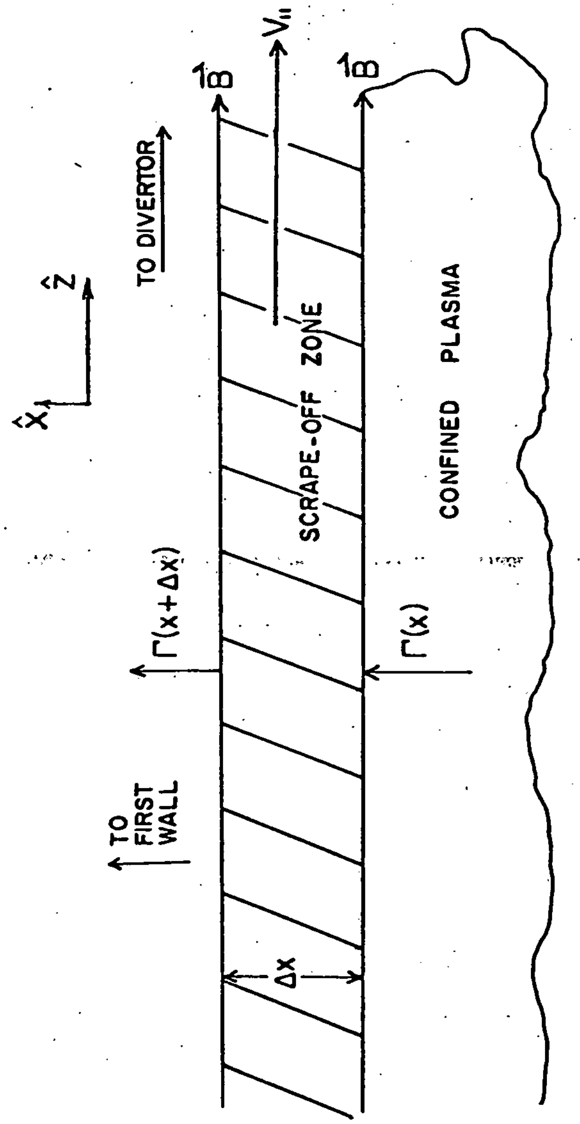

Fig. 1.4: The two dimensional scrape-off zone model that is used as the starting point for the flow model and the theory of Boozer.

Assuming a Fick's law type diffusion, $\Gamma_\perp = -D_\perp \frac{\partial n}{\partial x}$, one gets for the continuity equation

$$-\frac{\partial}{\partial x} D_\perp \frac{\partial n}{\partial x} + \frac{n}{\tau_\parallel} = 0. \qquad (1.7)$$

If we assume that $D_\perp$ is independent of x, then the solution is

$$n = n_s e^{-x/\lambda} , \qquad (1.8)$$

where $\lambda = (D_\perp \tau_\parallel)^{1/2}$ and n_s is the density at the separatrix. The density has an exponential fall off with an e-folding length λ. If one allows for an additional source in the scrape-off zone due to collisional ionization of neutrals, λ becomes

$$\lambda = \left(\frac{D_\perp \tau_\parallel}{1 - n_o \sigma v \tau_\parallel}\right)^{1/2}, \qquad (1.9)$$

where $n_o \sigma v$ is the total production rate of ions due to electron and ion collisions. In a similar way, one can add terms which model other processes that one believes may occur in the scrape-off zone and choose values for $D_\perp$ and $\tau_\parallel$ again as a function of the physical processes one believes are relevant. Having chosen these values, one can estimate the particle flux incident in the first wall as

$$\Gamma_{wall} = - D_\perp \frac{\partial n}{\partial x}\Big|_{r=wall}, \qquad (1.10)$$

and the plasma flux to the divertor

$$\Gamma_{wall} = \int \frac{n}{\tau_\parallel} dz. \qquad (1.11)$$

where z is in the direction of the magnetic field.

The choice of the various governing parameters within the context of this model has been the subject of considerable theoretical attention. The value and scaling of $D_\perp$ appears to be uncertain at present, but concerning the value of $\tau_\parallel$ there is more certainty. For example, one choice of $\tau_\parallel$ is the time that an ion might take to travel along a field line of length L to the collector plate[34],

$$\tau_\parallel = \frac{L}{V_\parallel}. \qquad (1.12)$$

One choice for $V_\parallel$ is the ion acoustic speed

$$V_\parallel = V_s = (kT_e/M_i)^{1/2}. \qquad (1.13)$$

This assumption is based on the treatment of the sheath problem carried out by S.A. Self[35], and assumes cold ions and ambipolar flow of ions and electrons in the presence of the long range electrostatic potential. (The assumption of ambipolarity in these models is one of the subjects that this thesis examines experimentally.) There is experimental justification for this assumption as well in that both the Diva[36] and FM-1[25] divertor experiments measure flow velocities at about one third the ion acoustic value. Based on analyses that treat the more relevant case of hot ions, one may expect a different long range potential and thus a different $V_\parallel$.[37] In this case the proper choice for $V_\parallel$ is $2(kT_i/2\pi M_i)^{1/2}$, for a maxwellian distribution of ions.

A second choice for $\tau_\parallel$ comes from the consideration of single particle dynamics in the scrape-off zone. As plasma particles follow field lines to the divertor they must move through an increasing magnetic field.[34] In this case, if the particle velocity vector is outside the loss cone of the mirror, it will be confined to a region outside the collector. (Of course, those particles with their velocity vector inside the loss cone will flow freely to the collector with a time $\tau_\parallel = L/V_\parallel$.) The maximum time that the remaining mirror confined plasma could be trapped is of the order of the 90 degree scattering time for ions[38] to scatter into the loss cone,

$$(\tau_\parallel)_{max} \simeq \tau_{ii} = \frac{3M_i^{1/2}T_i^{3/2}}{4\sqrt{\pi}\,\ell n\Lambda\; e^4 Z^2 n_i}. \qquad (1.14)$$

In addition to the classical processes discussed above, the loss cone distribution[38] of the mirror confined fraction of plasma can drive a wealth of high frequency instabilities that can break the adiabatic invariance of the magnetic moment and increase pitch angle scattering. Thus, in the presence of such modes, the best estimate of the parallel flow time may still be $(\tau_\parallel)_{min}$ of equation 1.13, and the plasma layer in the scrape-off zone may be too thin and tenuous to be an effective shield, unless the plasma flux crossing the separatrix is large enough. This will be discussed in more detail shortly. Low frequency modes[39] driven by the density gradient or bad field curvature can lead to enhanced cross field transport without inceasing the rate of pitch angle scattering, thereby increasing the flux to the wall.

As an illustration, for parameters typical of a next generation experimental tokamak with divertor,

T_i= 1 keV, T_e= 200 eV,
L= 3 m,
$n_e = 10^{12}-10^{13}$ cm^{-3} (at the separatrix),

the ratio $(\tau_{\parallel max}/\tau_{\parallel min})^{1/2}$ may vary from 10 to 30, and therefore can vary as much. Considering the possible variation in D_i leads to even greater uncertainty. Again the final values must rest on experiment.

A.T. Mense[40] considered the effect this large range of $\tau_\parallel$ and D_i had on the flux to the wall (among other parameters) using equation 1.7, with the boundary conditions:

(a) $-D_\perp \frac{\partial n}{\partial x}\big|_{x=0} = \Gamma_{sep}$ flux out of the core.

(b) lim n(x)=0 as x goes to infinity (ie: wall very far away)

The flux at the wall is then given by

$$\Gamma_{wall} = -D_\perp \frac{\partial n}{\partial x}\big|_{x=wall}.$$

The results for the indicated coefficients were as follows:

(1) $D_\perp = D_{Neoclassical}$, $\tau_\parallel = \tau_{ii}$ (pitch angle scattering)

$\Gamma_w \simeq 0$

(2) $D_\perp = D_{Bohm} = \frac{1}{16}\frac{KT_e}{eB}$(due to instab.), $\tau_\parallel = \tau_{ii}$ pitch angle

$\Gamma_w = (.94)\,\Gamma_o$; almost all particles escape the divertor.

(3) $D_\perp = D_{neoclassical}$, $\tau_\parallel = \tau_{\parallel min}$

$\Gamma_w \equiv 0$ an overly optimistic case.

(4) $D_\perp = D_{Bohm}$, $\tau_\parallel = \tau_{\parallel min}$

$\Gamma_w = .25\,\Gamma_o$; a marginally effective divertor.

In light of Mense's later transport equation solution it is found that too high a value of T_e was assumed in this earlier calculation. Thus $D_\perp = D_{Bohm}$ is far too high and with more realistic values of T_e, shielding efficiencies of 95% are found.

The shielding efficiency of the plasma in the scrape-off zone can be assessed from a continuity equation as well. If $\Gamma_o(x)$ is the neutral flux at any x,

$$\frac{\partial \Gamma_o(x)}{\partial x} = -n(x)n_o(x)(\sigma v), \qquad (1.15)$$

where n(x) and σv have the same definitions as before and $n_o(x)$ is the neutral density as a function of x. For a given plasma density profile and some neutral flux coming off the wall, the probability that an incoming neutral will be ionized is

$$f_i = 1 - \exp\left[\frac{-\langle \sigma v\rangle_{oi}}{v_{oi}} \int n\,dx\right], \qquad (1.16)$$

where n is the plasma density, v_{oi} and $\langle \sigma v\rangle_{oi}$ are the impurity velocity and the impurity ionization rate respectively. Thus one sees that the shielding depends on the line integral of the plasma density across the scrape off zone. Based on the simple flow model outlined above, if $\tau_\parallel$ is not a function of x, the line averaged density can easily be shown to be

$$\int n\,dx = \tau_\parallel\,\Gamma_{sep}, \qquad (1.17)$$

where Γ_{sep} is the plasma flux that crosses the separatrix. So as indicated above, a knowledge of the parallel flow time is not enough to specify the shielding, one needs to know the the plasma flux that is crossing the separatrix as well. The shielding efficiency is found to be greater than 99% (for $T_{imp} \simeq 5$ eV)[41] if:

$$n\lambda = \frac{3D_{\perp}\ \tau_*(n_p/a)}{(1-n_o\ \sigma v\ \tau_*)} > 10^{13}.\ \mathrm{cm}^{-2} \qquad (1.18)$$

Here n_p is the average plasma density in the core, and a the minor radius of the torus, and the line averaged density has been approximated by $n\lambda$.

A more careful analysis of the plasma particle and energy transport in the divertor, and the effect of various boundary conditions (at the separatrix and first wall) on a tokamak discharge has been carried out by several authors [41,42,43].

The group at Princeton[41] numerically solved detailed particle and energy balance equations for the electrons and ions. They included such energy loss and gain mechanisms as radiation, ionization, charge exchange and neutral beam heating. The effect of the divertor on the main core was assessed by solving these equations with boundary equations at the separatrix supposedly appropriate to the PDX experiment.

Comparison of the parameters of the PDX discharge with and without the divertor were made using their code. For the divertorless case, the coefficient R, the fraction of neutrals recycled back into the plasma is chosen to be 1 (Z_{eff} is chosen to be 8.) For the discharge with divertor, R is chosen to be .2 and Z_{eff} =1 (due to the expected reduction in impurity level.) The principal difference between the solutions to these two cases is the higher electron and ion temperature in the core (i.e. divertorless: $T_i \simeq 2.7$ keV, $T_e \simeq 1.8$ keV; diverted: $T_i \simeq 3.9$ keV, $T_e \simeq 3.8$ keV) for the diverted case, and smaller losses due to charge exchange.

A better treatment that does not rely on divertor type boundary conditions at the separatrix was done by Mense.[40] In this treatment, the transport equations were solved consistently in the core and the scrape-off zone. The only "boundary condition" was that $D_{\perp}$ was continuous across the separatrix. At the edge of the core near the separatrix the diffusion coefficient of the trapped ion mode was chosen. An adjustable parameter e_b was inserted into the assumed Bohm diffusion coefficient in the scrape-off zone:

$$D_{\perp} = e_b \frac{1}{16}\left(\frac{T_e}{eB}\right) \qquad (1.19)$$

to assure continuity of $D_{\perp}$ ($e_b \simeq$ .25 to .1). Various boundary conditions at the first wall were tried, and it was found that the transport equation solutions in the core and most of the divertor were insensitive to these boundary conditions.

In the scrape-off zone, the continuity equations as well as the electron and ion energy balance equations for cross field diffusion, parallel flow to the collector, and neutral gas effects were solved. In addition, 10% of the plasma neutralized at the collectors is recycled to the scrape-off zone. (Various deposition profiles of reflux were tried in the scrape-off, and found to have minimally different effects.)

The results of this code typically show a rapid fall off in density in the scrape-off zone as compared to the core profile. The temperature profiles of the ions and electrons show that $T_i \simeq T_e$ throughout much of the core region (due to rapid equilibration between species) but that T_e falls off much more rapidly than T_i in the scrape-off zone. The important effect that causes this difference is the sheath that forms at the particle collectors. This sheath forms to repel the majority of electrons that approach it, to assure that $\Gamma_i = \Gamma_e$. Only the hottest electrons can reach the surface and combine, but all ions that enter the sheath strike the plate. The net result is a more rapid cooling of the electrons than the ions. However, secondary electron emission from the collector can reduce the potential drop across the sheath and cause even larger losses to the electrons.[42] As we shall see in the description of the experiments that follows, a similar enhanced electron cooling can be the result of non-ambipolar diffusion. It should be noted that this effect will invalidate the assumption of ion acoustic flow into the divertor plate which is based on the existence of ambipolar flow. Therefore, another important area of experimental investigation needing further research is sheath formation in the presence of secondary emission, and its effect on V_* and electron energy loss, in one of the next generation divertor experiments.

A group at Princeton have applied an analysis similar to the method used by Mense to the case of a divertor for the INTOR tokamak.

Two Dimensional Divertor Models

The first two dimensional analytical study of the divertor was carried out by Hazeltine and Hinton.[43] In their model, it is assumed that the distribution function of both ions and electrons are Boltzmann distributions. The ions are further assumed to be collisionless and the electrons collisional in the scrape off zone. Their fundamental definition is that the ion density is simply the integral of the ion distribution function over that portion of velocity space where the ion single particle orbits are contained, and that the distribution function is zero on unconfined orbits. Using the Tokamak drift orbits for the untrapped particles, those orbits that pass beyond a certain minor radius (i.e. the separatrix at the collector) are taken to be lost to the poloidal divertor, in an idealized magnetic geometry. When this integral is evaluated and the result combined with the quasineutrality condition, they find the density scale length in the scrape-off zone to be

$$\lambda = -\left(\frac{3.9a\,\rho_{pi}}{R}\right)^{-1} \qquad (1.20),$$

where ρ_{pi} is the ion gyroradius evaluated with the poloidal field intensity and a/R is the inverse aspect ratio. This analysis yields singular results, however, for poloidal angles approaching the location of the divertor plates, which is an artifact of the collisionless assumption. (That is, the density profile approaches a step function at poloidal angles near the location of the divertor plates.)

In a later section of their paper, the authors extend the analysis to the region where the collisionless model breaks down. Based on a neoclassical analysis of particles diffusing into the divertor loss regions, it is shown that the density scale lengths obtained in the collisionless limit are valid everywhere except near poloidal angles of $\theta = \pm\pi/2$, the location of the divertor plates. At $\theta = \pm\pi/2$ the boundary layer analysis yields a more gentle fall off of density than the step function of the collisionless analysis. They conclude their paper by calculating the particle and energy loss to the divertor based on these results.

The importance of including the barely trapped ions in the energy and particle losses to the divertor, left out in the previous paper, was shown by EL-Nadi[44] in a similar analysis based on the drift kinetic equation.

A further refinement of the Hazeltine and Hinton paper is carried out by Daybelge and Bein[45]. Using the full Fokker-Planck collision operator in the ion drift kinetic equation, and accounting for the variation of the loss region as a function of position, the particle and energy losses to the divertor are calculated.

There is one final divertor model worth mentioning that is quite different from the models discussed previously. Fig. 1.4 describes the two dimensional model of Boozer[46] schematically. The model assumes plasma is deposited into the $\hat{z}$ directed magnetic field with some given profile $\Gamma(z)$. The divertor is assumed to accept any and all plasma given to it(common to all the divertor models discussed except the numerical models of Mense[40] and Meade[41] et al), the plasma then moving across and parallel to $\underline{B}$, through the sheath at the collector plates, and neutralizing itself on the target plates. (This process is assumed to depend only on x and z; y is a symmetry plane.)

A general set of equations given by Braginskii[38] are used to solve for the plasma transport. These equations are essentially the two fluid equations, with a term $\underline{R}$ included to account for inter-fluid "frictional" Coulomb forces, and energy balance equations[42]. Solution of these equations indicates once again that plasma flow parallel to $\underline{B}$ will be at the ion acoustic speed. However, here the similarity to the flow models ends. While the flow models predict equal flow of ions and electrons across field lines with a profile $n \propto e^{-x/\lambda}$, this model predicts different characteristic λ's for each species. It indicates that the electrons flow to the collector over a narrow region of width $\lambda \simeq \rho_e L/\lambda_e$ (ρ_e= electron gyroradius, λ_e=electron mean free path,L the field line length to the collector.) The ions will have a $\lambda = \rho_+(T_e)$, the ion gyroradius calculated with the electron temperature. The latter is wider than the predicted λ from the flow models, which for comparison purposes in these units is

$\lambda = (\rho_+ \rho_e L / \lambda_e)^{1/2}$. The flux of plasma is ambipolar only in the sense that equal fluxes of electrons and ions enter the sheath if integrated over the width of the particle collector. Interestingly enough, the FM-1 divertor experiment did note an ion outflow width of $\rho_+(T_e)$, and a large potential change across the scrape-off zone, as if the electrons and ions are separated. The existence of such non-ambipolar flow has also been observed in the experiment to be described. Boozer's model assumes cold ions and classical transport in the scrape-off zone. These are unlikely occurances in Tokamak reactor plasmas, but may have relevance for our experiment.

The final choice among these many theories can only rest on experiment. The large divertor experiments that are presently coming on line will hopefully answer this question. It is the humble hope of this author that the experiments described in this thesis will shed a ray of light on a small area of the divertor problem.

References-Introduction

1. G.M. McCracken, P.E. Stott, Nuc. Fus. 19,889 (1979).
2. A. Vershkov, S.V. Mirnov, Nuc. Fus. 14,14 (1974).
3. D. Meade, Nuc. Fus. 14, 289 (1974).
4. K.H. Burrell, Phys. Fluids 19, 401 (1976), and 20, 342 (1977).
5. V.I. Gervids, V.A. Krupin, JETP letters 18, 60 (1973).
6. J.A. Schmidt, N.R. Sauthoff, R.J. Hawryluk, Phys. Rev. Letters 32, (1974).
7. TFR Group, Phys. Rev. Letters 36, 1306 (1976).
8. S.A. Cohen, J.L. Cecchi, E.S. Marmar, Phys Rev. Letters 35, 1507 (1975).
9. T. Ohkawa, Kaku Yugo Kenkyu 32, 67 (1974).
10. M.S. Chu, J.M. Rawls, Phys Fluids 20, 1787 (1970).
11. S.K. Wong, Phys Fluids 21,299 (1978).
12. K.H. Burrell, et al., Phys. Rev. Letters 41, 1382 (1978).
13. R.C. Isler, et al., in Plasma Physics and Controlled Nuclear Fusion Research, (Proc. 8th Int. Conf. Brussels, 1980) paper IAEA-CN-38/A-5.
14. L. Spitzer Jr., " A Proposed Stellarator" , U.S. Atomic Energy Comission Report No. NYO-993 (PM-S-1) (1951).
15. G.A. Emmert, "Modeling of Bundle Divertors", Dept. of Nuclear Engineering, University of Wisconsin, Madison, UWFDM-343 (1980). See also: G.A. Emmert, A.W. Bailey, UWFDM 365 and 362 (1980).
16. M. Keilhacker, Magnetic Divertors, in Tokamak reactors for

Breakeven (Proc. Int. School of Fusion Reactor Technology, Erice, Italy 1976) Pergamon Press, Oxford England (1978).

17. C.R. Burnett, D.J. Grove, R.W. Palladino, T.H. Stix, K.E. Wakefield, Phys. Fluids 1, 438 (1958).

18. L. Spitzer, et al, Bull. Am. Phys. Soc. 9, 320 (1964).

19. N.A. Uckan, et al., ORNL/TM-5438 (1976).

20. D.W. Kerst, Plasma Physics 4, 253 (1962).

21. P.E. Stott, A. Gibson, Nuc. Fus. 17, 481 (1972).

22. P.E. Stott, A. Gibson, Nuc. Fus. 18, 475 (1978).

23. P.E. Stott, et al, in PLasma Wall Interactions (Proc. Int. Symp. Julich, 1976) Pergamon Press, Oxford (1977) 39.

24. R.G. Mills, Princeton Plasma Physics Report Matt-949, (1973).

25. K. Ando, et al., Princeton Plasma Physics Report Matt-1078, (1974).

26. DIVA Group, Nuc. Fus. 18, 1619 (1978).

27. D.M. Meade, J.C. Simms, Proceedings of the International Symposium on Plasma Wall Interactions, (Julich 1976). (Pergamon Press, Oxford, 1977) 683.

28. G. Haas, M. Keilhacker, Proceedings of the International Symposium on PLasma Wall Interactions, (Julich 1976) (Pergamon Press, Oxford, 1977) 691.

29. K. Bol, Bull. Am. Phys. Soc. 25, 851 (1980).

30. D.W. Kerst, "Electric Field Effects in Our Octupoles and Applications to Divertors and Limiters", Dept. of Physics, University of Wisconsin, PLP 613 (1965).

31. E.J. Strait, Ph.D. Thesis, University of Wisconsin, Madison, Wisconsin (1979).

32. D.M. Meade, et al., in Plasma Physics and Controlled Nuclear Fusion Research (Proc. 5th Int. Conf., Tokyo, Japan, 1974) Vol 1, IAEA, Vienna (1975) 605.

33. B. Badger, et al., UWMAK-1, a Wisconsin Toroidal Fusion Reactor Design, University of Wisconsin Nuclear Engineering Dept., Madison, Wisconsin, 1974.

34. A.T. Mense, G.A. Emmert, J.D. Callen, Nuc. Fus. 15, 703 (1975).

35. S.A. Self, Phys. Fluids 6, 1762 (1963).

36. H. Ohtsuka, et al., Plasma Phys. 20, 749 (1978).

37. G.A. Emmert, R.M. Wieland, A.T. Mense, J.N. Davidson, Phys. Fluids 23, 803 (1980).

38. S.I. Braginskii, in Reviews of Plasma Physics, Vol. 1 p.215.

39. B. Badger, et al., UWFDM 112, Nuclear Engineering Dept., University of Wisconsin, Madison, Wisconsin, UWMAK 2 Conceptual Fusion Power Reactor Design Report Jan. (1975).

40. A.T. Mense, Ph.D. Thesis, Dept of Nuclear Engineering, University of Wisconsin, Madison, Wisconsin (1976).

Also see: A.T. Mense, G.A. Emmert, Nuc. Fus. 19, 361 (1979).

41. D.M. Meade, et al., IAEA-CN-33/A15-4 Vol. 1, 605 (1974).

42. G.D. Hobbs, J.A. Wesson, Plasma Physics 9, 85 (1967).

43. F.L. Hinton, R.D. Hazeltine, Phys. Fluids 17, 2236 (1974).

4. A. El-Nadi, Phys. Fluids 22, 1570 (1979).

5. U. Daybelge, B. Bein, Phys. Fluids 20, 1777 (1977).

6. A.H. Boozer, Phys. Fluids 19, 1210 (1976).

Chapter 2

Experimental Apparatus

A schematic of the D.C. machine, the device used for these experiments, is shown in Fig. 2.1. This apparatus was constructed in the years 1970-71 by Dale Meade, Tom Jernigan and Ron Prater and used by Prater and Jernigan as the main experimental device for their Ph.D. thesis.[1,2] Subsequently R. Richards obtained his Ph.D. for experiments carried out on the same device.[3]

The center section of the vacuum tank was constructed by rolling 3/4 inch 5083 aluminum into a cylinder and welding the seam. The end flanges are cut from 1.5 inch 5083 aluminum and are sealed to the cylindrical section with large Viton O-rings. The entire device is supported on a stand, with the center line (see Fig. 2.1) in a horizontal plane. The tank is 66 cm. long and 92 cm. in diameter. Ports are provided in the tank for six internal ring supports, diffusion pump, ion gauge, and the current feed to the internal ring as well as numerous other diagnostic ports. All port seals are either indium or Viton O-rings.

Vacuum System

A base pressure in the mid 10^{-7} range is obtained with an oil diffusion pump, topped by a Freon cooled baffle and a water cooled cold cap, backed by a mechanical pump. The oil diffusion pump is a six inch PMC-6 Consolidated Vacuum Corp. charged with DC-704 silicon base oil. A small Tecumseh Corp. refrigeration unit cools the

Fig. 2.1: A schematic of the D.C. Machine showing: A-Lisitano coil; F-internal ring; G-Helmholtz coils; H-mirror coils; B,C, D-typical field lines for the chosen magnetic configuration.

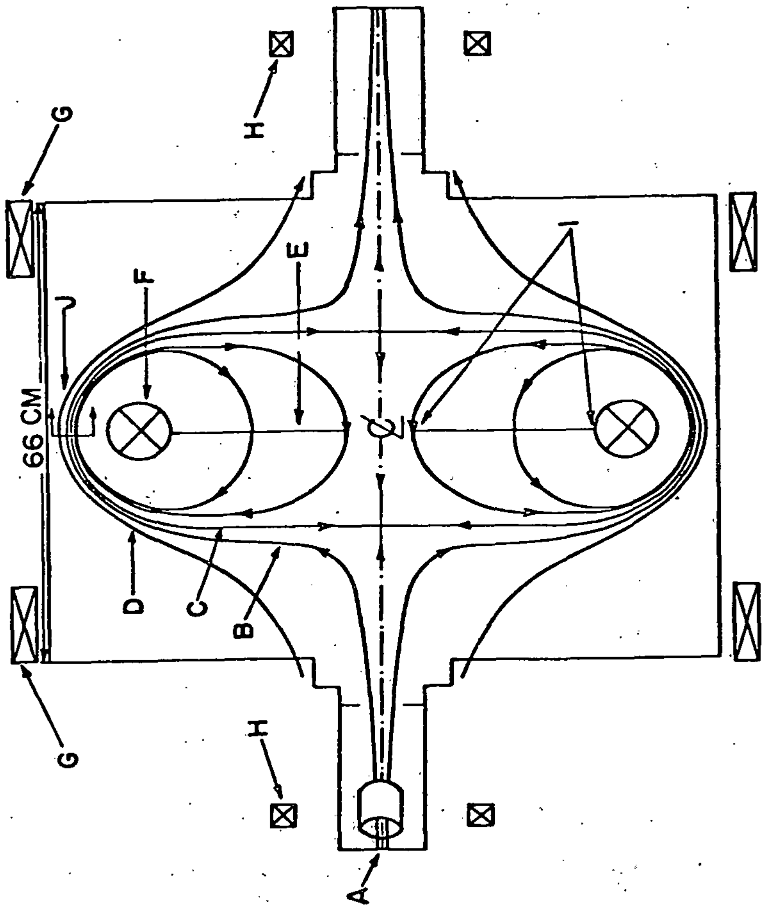

Consolidated Vacuum type BC-61C baffle to about -60 degrees farenheit to reduce backstreaming of diffusion pump oil. The baffle reduces the pumping speed to about half of its original 1400 l/s. Finally a Welch mechanical pump with a pumping speed of 500 l/s evacuates the diffusion pump through a steel-wool packed foreline trap, whose purpose is to reduce backstreaming of mechanical pump oil. A Leybold-Heraeus DK-45 mechanical pump, with a pumping speed of 650 l/s, is used to rough the system down from atmospheric pressure through a separate port.

Analysis of the residual gasses in the system with a Molytek Spectramass 80 mass spectrometer showed the dominant partial pressure in the system was that of water. In addition smaller peaks were observed at mass to charge ratios in the range 41-50 and were thought to be hydrocarbons from the diffusion pump oil. Fig. 2.2 shows typical R.G.A. traces when the base pressure was $5x10^{-7}$ torr. The dominant peaks at m/e=18 (partial pressure= $3.3x10^{-7}$ torr.) and m/e=28 (partial pressure=$1.7x10^{-7}$ torr.) are evident. Both substances are undesirable in a plasma experiment because of potential changes in work function they can cause on probe surfaces[4], as well as adding effective capacitance and resistance in series with the probe. An additional effect is due to the silicon base pump oil. On surfaces that have been continually bombarded with plasma a glassy non-conducting deposit has built up over the years, in places thick enough to flake off. Analysis of these brown deposits by Auger spectroscopy has shown they consist largely of silicon and carbon with

Fig. 2.2: Residual gas analyzer traces of the D.C. machine vacuum before the installation of the cryopanel. The horizontal scale is mass to charge ratio of the impurity, and the vertical scale is proportional to the partial pressure of the impurity. Shown are three different sensitivities of the R.G.A.

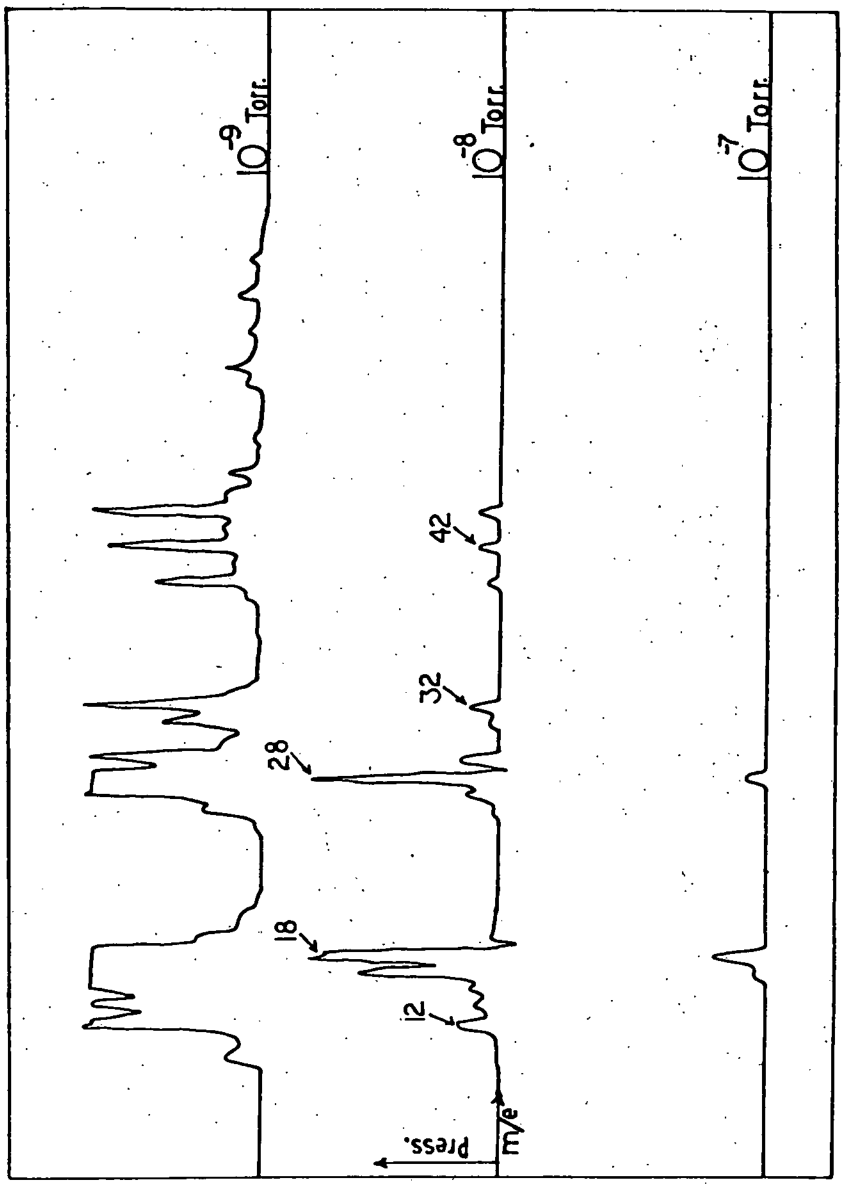

trace amounts of chlorine and sulphur, suggesting they are chemically cracked pump oil. Build up of this same coating has been observed on probe surfaces, where it can change the effective collecting area of the probe.

To eliminate or reduce as much as practical the bad effects of these impurities, a liquid nitrogen cooled cryopanel was constructed and installed on the D.C. machine. The cryopanel is nearly identical to one that has been shown to be effective on the octupole and was designed by Jon Twichell. Fig. 2.3 shows the R.G.A. traces after installation of the panel. The water peak has been reduced to $1.2\text{x}10^{-7}$ torr. and the oil peaks have been reduced by about a factor of three. The cryopanel has two square feet of baffled, cooled copper plate with a pumping speed for water of about 2000 l/s.

The pressure in the system is monitored in the 1 atm. to 1 micron range with varian type 0531 thermocouple gauges. For pressures below 1 micron, a Varian 563 Bayard-Alpert type ionization gauge is used and monitored by a Varian 843 ionization gauge controller. To control the pressure during experiments, gas is bled into the tank through a needle valve while the system is being pumped on.

Magnetic Field Coils

The original intent in the design of the magnetic field structure of the D.C. machine was to model certain properties of multipoles in a steady state device.[1] To this end, and the desire for flexibility in the available configurations, the coil arrangement in Fig. 2.1 was

Fig. 2.3: Residual gas analyzer traces after the installation of the cryo-panel. Note the reduction of the water peak at m/e=18, and the reduction in the high m/e peaks attributable to pump oil.

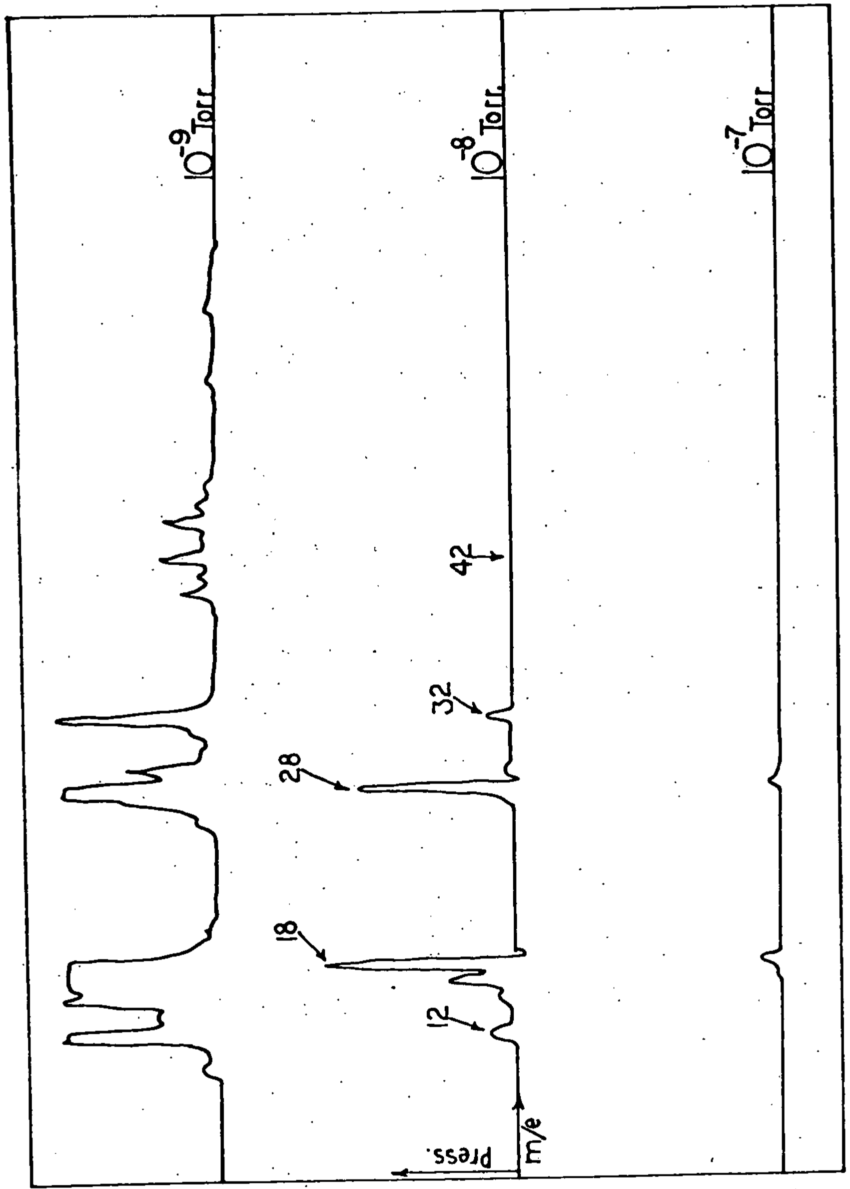

arrived at. For maximum flexibility there are three different sets of coils, and the current in each set can be varied independently.

Forming the field are a set of five coils. The largest coils external to the vacuum chamber are in a Helmholtz configuration. These coils are made up of 18 "pancakes", each "pancake" having 12 turns of copper tubing and measuring 56.5 cm. in major radius, 10 cm. in thickness and 14 cm. in length. The successive turns in each "pancake" are insulated from each other by fiberglass tape and potted in epoxy. The power supply for these coils is a modified Lorain Products Flotrol magnetic amplifier, capable of 400 amps at 70 volts. These coils are usually operated at about 70 amps per turn, which produces an on axis field of about 250 G.

Carrying current in the same direction as the Helmholtz coils are the small end coils. These coils provide the resonance field necessary to operate the Lisitano source, as well as pinching the field down to form a magnetic mirror. The end coils are wound from 100 turns of the same copper tubing as the Helmholtz coils. The "cube" power supply for these coils is capable of 275 amps at 36 volts but is normally run at 180 amps. The machine's field maximum of 1200 G. occurs at the throat of these coils.

Finally the internal ring of the D.C. machine is a magnet that was originally loaned to the experiment by the Princeton Plasma Physics Lab., and only recently became property of the University of Wisconsin. The magnet had been used in the Spherator S.P.-1 experiment. This coil has twelve turns of copper inside a stainless steel jacket with an inside major radius of 33 cm. Supporting the coil inside the vacuum vessel are six 1/8 inch diameter stainless steel rods, and both rods and coil are electrically isolated from the main vacuum chamber. The current supply to the ring is a surplus Magneflux metal flaw detector supply that can supply 4 kA at 12 V but until recently only in a step-wise fashion. It was found during the preliminary investigations of this thesis that a continuous variability of the current was necessary. Therefore T. Lovell, C. Strawitch and D. Grubb designed and installed the circuit shown in Fig. 2.4 that allows the current to be nearly continuously varied between the taps on the autotransformer.

The two most useful configurations for divertor studies are shown in Fig.2.5 , and the third is essentially a simple mirror configuration when the internal ring is not energized. The lower magnetic configuration in Fig. 2.5 is most similar to a divertor field plot, but for reasons outlined later the upper configuration was chosen. For the configurations shown in Fig. 2.5 the current in the internal ring is run opposite the currents in the Helmholtz coils.

The outputs of all three power supplies are highly capacitively filtered in addition to the inherent current stability provided by the inductive loads of the magnets. All of the magnets are cooled by a closed loop cooling system that pumps a distilled water anti-freeze mixture (to prevent corrosion) through the coils at approximately 140 Psi. and seven gal./min. In turn a heat exchanger transfers the waste heat to the city water. A system of electronic interlocks

Fig. 2.4: Schematic of the modifications to the Magneflux power supply to make it continuously variable.

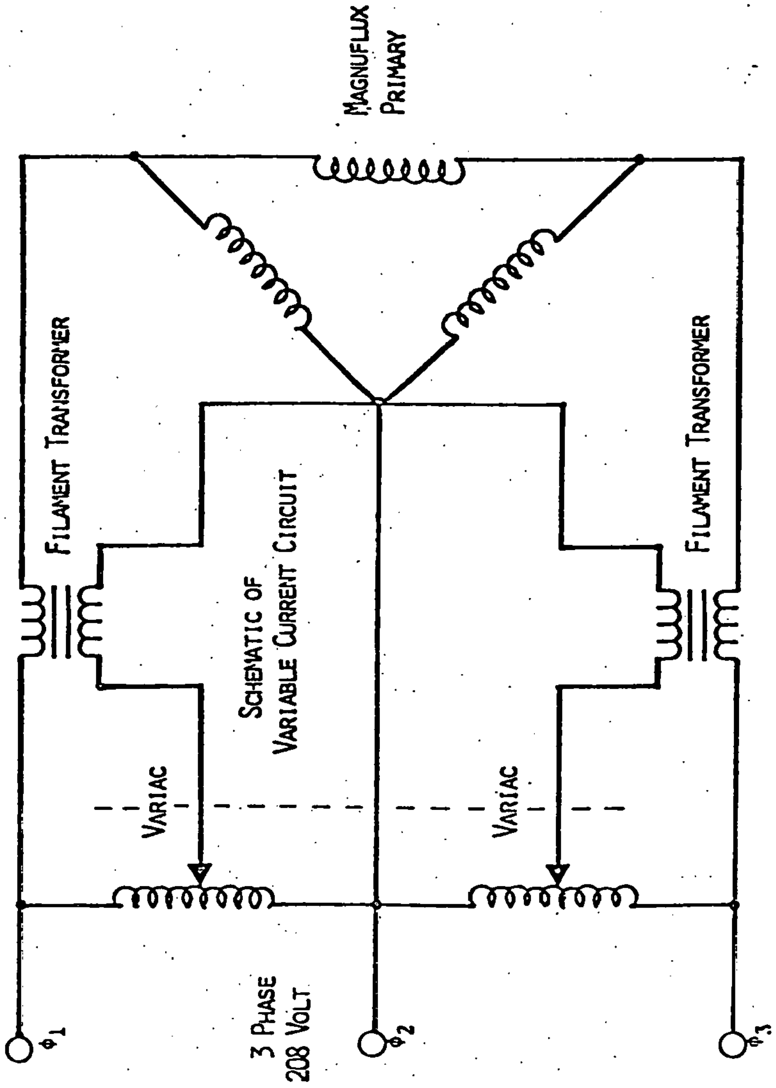

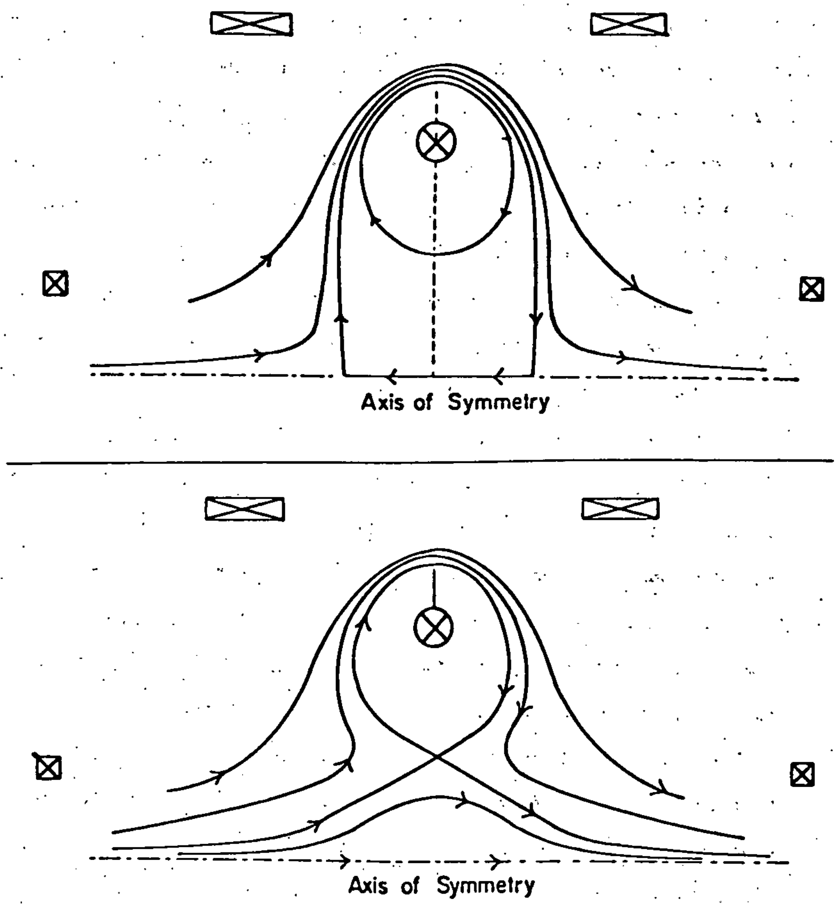

Fig. 2.5: Magnetic Configurations Available for Divertor Studies

allows power to be applied to the coils only when the cooling water is circulating.

<u>Plasma Source</u>

The plasma source used throughout these experiments was a so-called "Lisitano coil" slow wave structure similar to ones found in transmission lines in microwave tubes.[5] The coil, shown in Fig. 2.6, is an open ended metal cylinder slotted in its axial direction. R.F. energy is fed into one end of the transmission line formed by the slots (shown schematically in Fig. 2.6) and the other end is terminated in a short circuit. The slots are one half wavelength long and there is a 180 degree phase shift between similar points on adjacent slots. The fringing field from the TEM wave propagating in the slots forms a field pattern similar to a $TE_{0,1}$ mode of a cylindrical resonant cavity, and will be stronger on the inside than on the outside due to the cylindrical shape. A $TE_{0,1}$ mode has its electric field vector in the θ direction of the cylinder, and changes direction on each half cycle of the applied R.F. and similarly so does a Lisitano coil. The advantage to using a Lisitano coil over a cylindrical resonator is that the internal field configuration is independent of its diameter and relatively independent of the frequency of the applied R.F. Therefore the size of the source can more easily be tailored to the reqirements of a given experiment.

When an axial magnetic field is applied, one can make use of the resonant nature of the orbit of electrons in a magnetic field by applying R.F. at the cyclotron frequency to achieve breakdown at a

Fig. 2.6: The slotted cylinder Lisitano coil, showing the microwave power feed and the orientation of the magnetic field.

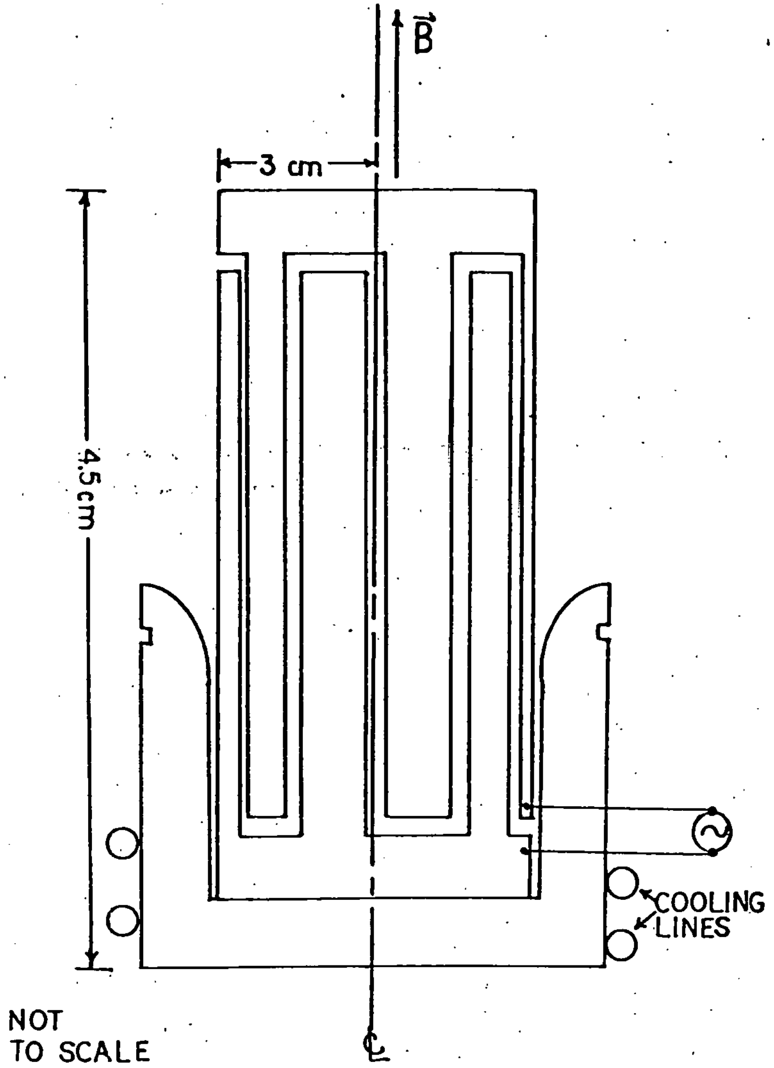

lower electric field than if no magnetic field were present.[6] Source gas is bled into the base of the coil, and a breakdown can be achieved from 10^{-6} and up to 10^{-3} torr.

Once the plasma is formed, power is absorbed at the upper hybrid resonance frequency

$$f_a = f_{uh} = (f_{pe}{}^2 + f_{ce}{}^2)^{1/2} =$$

$$\frac{1}{2\pi}\left(\frac{4\pi ne^2}{m_e} + \left(\frac{eB}{m_e}\right)^2\right)^{1/2}$$

$$= 2.8(n(\mathrm{cm}^{-3})1.03\times10^{-11} + B^2(\mathrm{kG.}))^{1/2}$$

where f_a is the applied frequency, f_{uh} is the upper hybrid frequency, f_{pe} is the electron plasma frequency, and f_{ce} is the electron cyclotron frequency. For plasma densities less than 10^{11} cm^{-3} this reduces to $f_a = f_{ce}$.[1]

Care must be taken to avoid higher order coaxial modes that will compete for the available power with the desired mode in the coil.[7] From Fig. 2.6 it will be observed that the coil holder, with the attached cooling lines, and the coil form a coaxial transmission line. Higher order coaxial modes therefore can exist in the gap between coil and holder. For example, the $TE_{1,1}$ mode has the lowest cutoff wavelength

$$\lambda_o = \pi(b+a)/2$$

where λ_c is the cutoff wavelength, b is the inside diameter of the holder and a the outside diameter of the coil. For our parameters λ_c=19 cm. and the R.F. wavelengths used are near 12 cm indicating that the $TE_{1,1}$ mode will exist. In fact breakdown between the holder and the coil to the point of completely eliminating the desired central discharge was a severe problem for a time. It was cured by enlarging the space between coil and holder, and by cutting a smooth radius on the end of the holder where a sharp edge had been. Both steps were designed to reduce the electric field in this region. Breakdowns with as little as 4 W of input power have been achieved in the desired mode after these modifications.

The microwave power for the coil is supplied by a Raytheon RK5609 magnetron capable of up to 70 W at 2.95 GHz. To prevent reflected power from the coil from adversely affecting the magnetron a P and H Laboratories model B1-526317 circulator is interposed between coil and magnetron source and provides 20 db of isolation.

References-Chapter 2

1. R. Prater, Ph.D. Thesis, Wisconsin Plasma Physics Report PLP 452 (1971).
2. T.C. Jernigan, Ph.D. Thesis, Wisconsin Plasma Physics Report PLP 424 (1971)
3. R.K. Richards, Ph.D. Thesis, Wisconsin Plasma Physics Report PLP 675 (1976)
4. J.D. Swift and M.J.R. Schwar, Electric Probes for Plasma Diagnostics, American Elsevier, New York(1969)
5. G. Lisitano, Proceedings of the Seventh International Conference on Phenomena in Ionized Gasses (Gradevinska Knjiga Publishing House, Boegrad 1966) Vol. 1,p 464.
6. J.D. Cobine, Gaseous Conductors, Dover Publications Inc., New York, (1958).
7. Walter R. Day, Princeton Plasma Physics Report TM-238, (1967).

Chapter 3

Diagnostics

All of the data for the experiments described in this thesis were taken with electrostatic probes in one form or another. Electrostatic probes have the advantage of providing a simple, local measurement of plasma parameters but the price to be paid is the perturbing effect they may have on the plasma. The latter can hopefully be minimized by designing the probe to be physically small and, in addition, perhaps draw no net electrical current. Implementation of probes as a diagnostic then is a simple matter in general; however, the interpretation of the probe characteristic is far from simple and still a subject of active research. Still another complication arises when a layer of impurities resides on the probe surface, which is almost unavoidable in most laboratory plasmas. Since Langmuir[1] first developed the electrostatic probe technique in 1924, there has developed a very extensive literature on probes. The work of Chen[2] was the first systematic account of probe theories through 1965. Swift and Schwar[3] updated the work of Chen to the year 1969. Finally Chung, Talbot, and Touryan[4] summarize the state of the art up to 1975.

Spherical Single Tip Probes

The so called I-V characteristic of a probe contains all of the information about a plasma that one can obtain from a probe.[2,5] The simple probe theory of Bohm[6] predicts an ion current, which, at voltages sufficiently negative with respect to the plasma potential to repel the majority of electrons, is independent of voltage. Based on the so called "Bohm sheath criterion" from this same theory, the ion current to the probe is given by

$$I_{oi} = n_i eA\left(\frac{kT_e}{m_i}\right)^{1/2} , \qquad (3.1)$$

where A is the probe area and I_{oi} the ion saturation current. Obtaining T_e, the electron temperature, from the exponential part of the I-V characteristic enables one to calculate n_i the ion or plasma density. A typical I-V characteristic from the D.C. machine plasma is shown in Fig. 3.1. The lack of saturation of the ion current is obvious and leads one to suspect the simple theory of Bohm. The analysis of Laframboise[7] is applicable to the case of non-saturating ion collecting probes, for the case when the ion mean free path is much greater than the probe radius, which certainly is the case in our plasmas. The numerical work of Laframboise takes into account the ion orbits that will occur in the attracting potential well of the probe, and calculates the ion current by noting which orbits will intersect the probe surface. Knowing the floating potential and the electron temperature, the value of I_{oi} from the I-V trace is uniquely determined in his theory, and from this follows the ion density. It is worth pointing out that the paper by Sonin[8] was very useful in the actual application of the results of Laframboise's theory, for reasons described in Ref. (4).

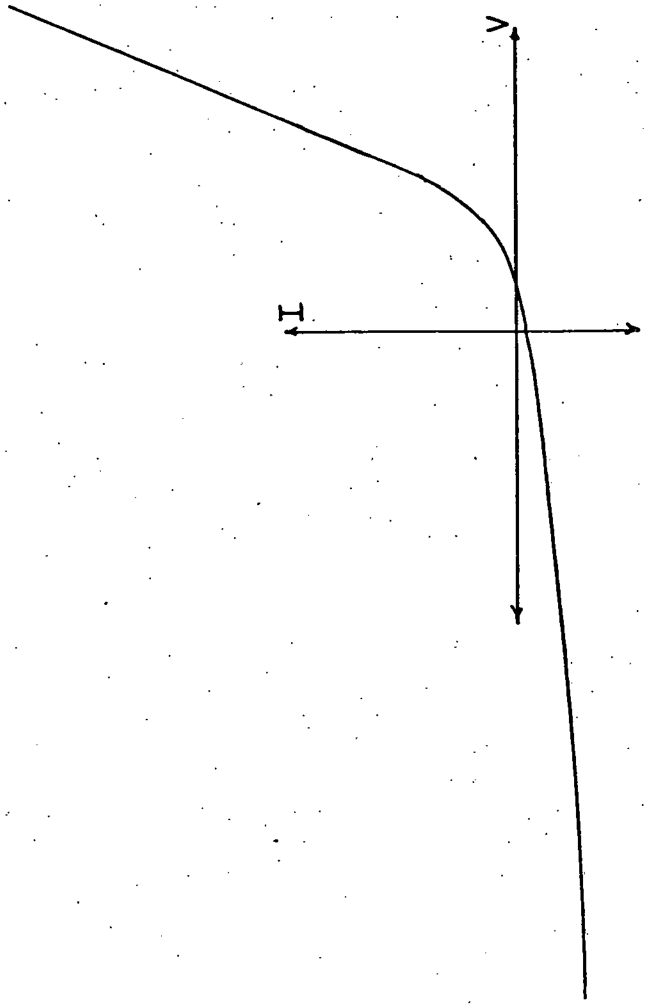

Fig. 3.1: A typical probe characteristic in the D.C. machine, illustrating the lack of ion saturation current.

The theoretical results of Laframboise are derived under the assumption that there are no magnetic fields present. However, if the ion gyroradius is much greater than the Debye length, one has a reasonable expectation that the results of this theory are still applicable. In this limiting case, the ion orbits on the sheath spatial scale are very nearly straight lines outside the sheath, as is implicitly assumed in Laframboise's theory. For our parameters: $\underline{B}\simeq 50$ G, $\rho_i \simeq 2.5$ cm, $\lambda_D \simeq .2$ mm, and obviously $\rho_i \gg \lambda_D$. In fact the results of Chen et al[9] and Brown et al[10] support this conclusion by experimental comparison of density obtained from probes, interpreted using the theory of Laframboise, and a microwave interferometer.

The electron retarding portion of the I-V characteristic can still be used to determine the electron temperature in this parameter regime. As in simple probe theory, the current (dominated by electrons) to the probe in the retarding region varies as

$$I \propto \exp \frac{e(V-V_p)}{kT_e} \tag{3.2}$$

where V is the probe voltage and V_p the plasma potential. A program that carries out an exponential least squares fit to the I-V characteristic was written for a HP-29c programmable calculator and used to deduce T_e. In all cases the curves are very close to an exponential with a coefficient of determination, R^2, of .95 or greater

(R^2=1 is a perfect exponential). The program then impliments the theory of Laframboise to determine the density.

Having determined T_e and V_f, the floating potential, as the voltage on the probe at zero current (the point where the I-V intersects the voltage axis) one can determine the local space or plasma potential from the relationship

$$V_p = V_f + \alpha T_e \tag{3.3}$$

where the value of the constant α can also be obtained from the theory of Laframboise. It is convenient at times to use these same probes to measure the floating potential without the necessity of sweeping the probe through its I-V characteristic. In this case the probe must be terminated in a resistance much larger that the sheath impedance.[5] In our case $R_{sheath}=(kT_e)(1/I_{oi})$ = 50 k ohms, so a Tektronix 10 M ohm balanced attenuator probe is more than adequate. It is interesting to note that the so called "probe paradox"[11] that is observed in the Octupole is not observed in the D.C. machines. This refers to the experimental observation that a high impedance probe indicates a different value of the floating potential than a low impedance probe in the Octupole. The difference is attributed to unequal rates of impurity coat buildup on the probe surfaces in the two cases.

Shown in Fig. 3.2 is the circuit used to obtain the I-V characteristics. Typically the entire characteristic can be generated in a few seconds when the bias voltage is swept by hand. The differential amplifier is used as a high impedance voltmeter and allows ease in scaling over the voltage range that is necessary to measure maximum and minimum densities.

Impurities on probes have been shown to cause the measured T_e value to be higher than the actual T_e as well as affect the value of V_f that is measured.[12,13] In an effort to minimize the effect of impurities on the probe characteristic, the probe tips are first cleaned with acetone and then alcohol before insertion into the vacuum chamber. Once inside the chamber, the probe is biased to ion saturation to clean the surface of vacuum evolved impurities. Both electron and ion bombardment have been reported in the literature as a method of cleaning probes.[12-16] During data acquisition, the probe is maintained at ion saturation and only swept briefly through its I-V trace. This method has also been reported to maintain a clean probe surface under constant ion bombardment desorption of impurities. This is also supported by experimental observation in both D.C. machines. Probes maintained at the floating potential or electron saturation for periods of days of accumulated run time develop black ash-like deposits. These deposits have been shown by Auger spectroscopic analysis to consist of silicon, carbon, and sulphur all of which may have come from cracked diffusion pump oil. On the other hand, probes kept at ion saturation do not develop such deposits, and remain

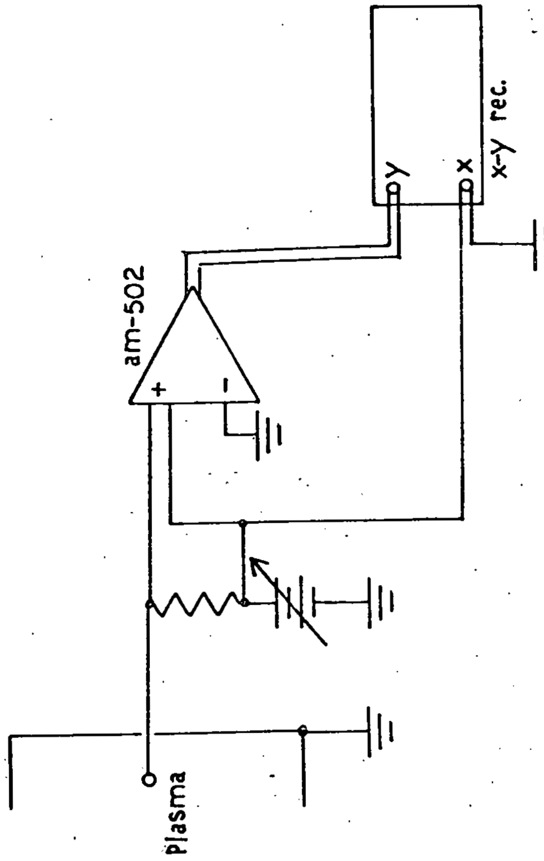

Fig. 3.2: Schematic of the circuit used to obtain the probe characteristic, showing the Tektronix AM-502 differential amplifier and the HP-7035B x-y chart recorder.

remarkably clean and free of impurities. A probe biased to electron saturation in the D.C. machine will glow cherry red, which would certainly seem to be enough to boil away impurities. However, the observations don't support this idea, but apparently imparting momentum directly to the impurities by ion bombardment is more effective.

Profiles of the various plasma parameters are made by simply moving the probe through the plasma and taking I-V traces on a point by point basis.

The error bars shown on the density data are based on experimental comparisons of the density measured with a microwave interferometer and a Langmuir probe interpreted with the theory of Laframboise.[9,10] For the very weak magnetic field that exists in our experiment, the theory of Laframboise predicts densities that are less than 20% lower than the true density as measured with an interferometer. This is expected to be the dominant error contribution, and thus we conservatively place error bars of ±20% on the density data.

The dominant error source in the electron temperature measurement is due the resistive impurity coat that forms on the probe surface, and causes indications of higher electron temperature than is actually present.[14] (Because the probe is swept slowly through its I-V characteristic, the capacitive portion of the impurity layer model is ignored in the analysis that follows.) The resistance of the impurity coat is typically estimated to be of the order of 200-300 k ohms, but a better estimate upon which to base an error estimate is available. By subtracting off the ohmic voltage drop that occurs across the layer when current is drawn, one obtains the true voltage that the plasma sees at the surface of the impurity layer. For an assumed impurity layer resistance, the plot of collected current versus true probe voltage should obey an exponential Boltzmann relation, the best exponential being given by an assumed layer resistance that equals the actual value. This procedure was carried out and found to work nicely, indicating a typical resistance of 25 k ohms, substantially smaller than the reported values. This value of the layer resistance causes the T_e values to be typically 20% too high. Once again this appears to be the dominant error as reproducibility is not a problem in the D.C. machine plasmas, and thus a conservative estimate on the error in T_e is about ±20%.

The measured floating potential can differ from the correct floating potential due to secondary emission enhanced by work function changes of the probe surface again caused by an impurity layer. (The choice of platinum as the material of our probe tips reflects efforts to minimize these effects, as platinum has a high work function.) Typical errors on the floating potential are reported in the literature[9] to be ± 10%.

The methods used for probe construction are a local standard and are adequately described elsewhere.[15] It was soon discovered that the standard method of sealing the probe stalk to the vacuum feed through, namely high vacuum epoxy, would not stand up to 1 kW. of continuous microwave bombardment from another experiment on the D.C. machine. Therefore, for probes that couldn't be withdrawn from the vacuum chamber, another method of probe constuction had to be arrived at. Fig. 3.3 shows the probe that stood the test of microwaves, and is the probe used to take most of the data to be discussed later. (Not shown is the angled probe tip that made withdrawal through a vacuum feed through impossible.) The probe stalk is structurally supported by #31 Sauereisen high temperature cement. This cement is porous so a hole is drilled near the tip to avoid virtual leaks. The vacuum seal is made at the other end of the support with high vacuum epoxy. The probe support is made of anodized alumunum. To prevent the probe support and the wire to the probe tip from acting like a coaxial wave guide and conducting microwaves to this outer seal, the center wire is wound into a large inductor. To further prevent arcing from the wire to the aluminum support, the coil is surrounded with alumina tubing. A similar probe without the inductor soon saw the outer seal reduced to ash. The D.C. voltage drop across the inductor is negligible as is necessary for accurate I-V traces.

Striped Particle Collector

For measurements of the plasma flux to a given surface striped particle collectors like those used by Cavallo[16] and treated theoretically by Mak[17] and Mosberg[18] were used. Neither of the latter two authors treated the case of magnetic field lines perpendicular to the collector surface, however, so we used the analysis carried out in the field free case. Plasma motion along a uniform magnetic field is

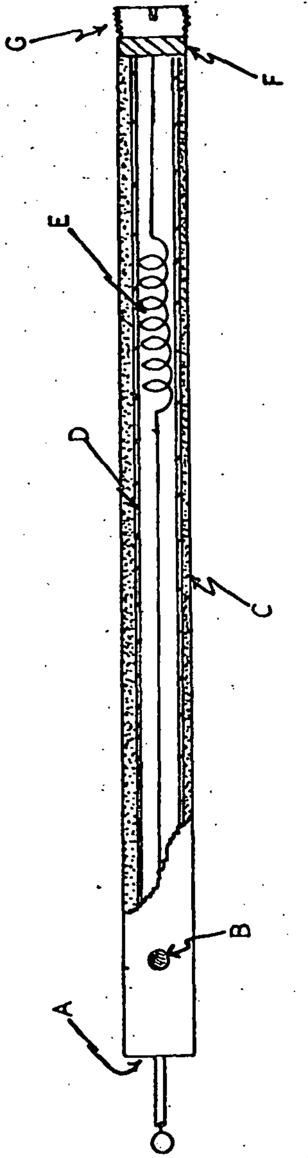

Fig. 3.3: Cross sectional view of the microwave resistant probe, showing: A-Sauereisen cement as a high temperature support for probe tip, B-pump-out hole, C-aluminum probe stalk, D-alumina inner support, E-inductor, F-vacuum seal, G-microdot coaxial connector.

unaffected by the presence of the field. So, as long as the current drawn from a given tube of flux is much less than the cross field current that fills that tube, any field free probe analysis is valid. If the current drawn does approach the filling current, then one presumably begins to encounter magnetic field effects as plasma must now move across $\underline{B}$ to get to the probe. Experimental observations, both in our experiment and the experiments of others[9], support the use of the field free analysis as well. A plane probe oriented perpendicular to the magnetic field in the D.C. machine gives an I-V trace that is very similar to that predicted by the field free theory, exhibiting good ion saturation current. On the other hand, a plane probe with its face parallel to $\underline{B}$ exhibits a severely distorted I-V trace in both the electron and ion collecting regions. The analysis of Mak, for the field free case, uses simple probe theory for plane collectors. Therefore, we felt the application of the field free analysis to the collectors oriented perpendicular to $\underline{B}$ was justified.

Shown is Fig. 3.4 is a typical I-V characteristic from one of the striped particle collectors used, and is in fact similar in shape to the trace expected in the magnetic field free case. Also shown is the circuit used to bias the collectors. Below a certain plasma density, the I-V traces bear little resemblance to the traces shown in Fig. 3.4, so much so that application of the theory is impossible. The traces become highly asymmetric, and cross and recross the voltage axis in an irreproducible fashion. It seems likely that this may be a Debye length effect because for proper operation of the collectors the

Fig. 3.4: A simplified schematic of the striped particle collector and biasing circuitry. Also shown is an actual I-V characteristic.

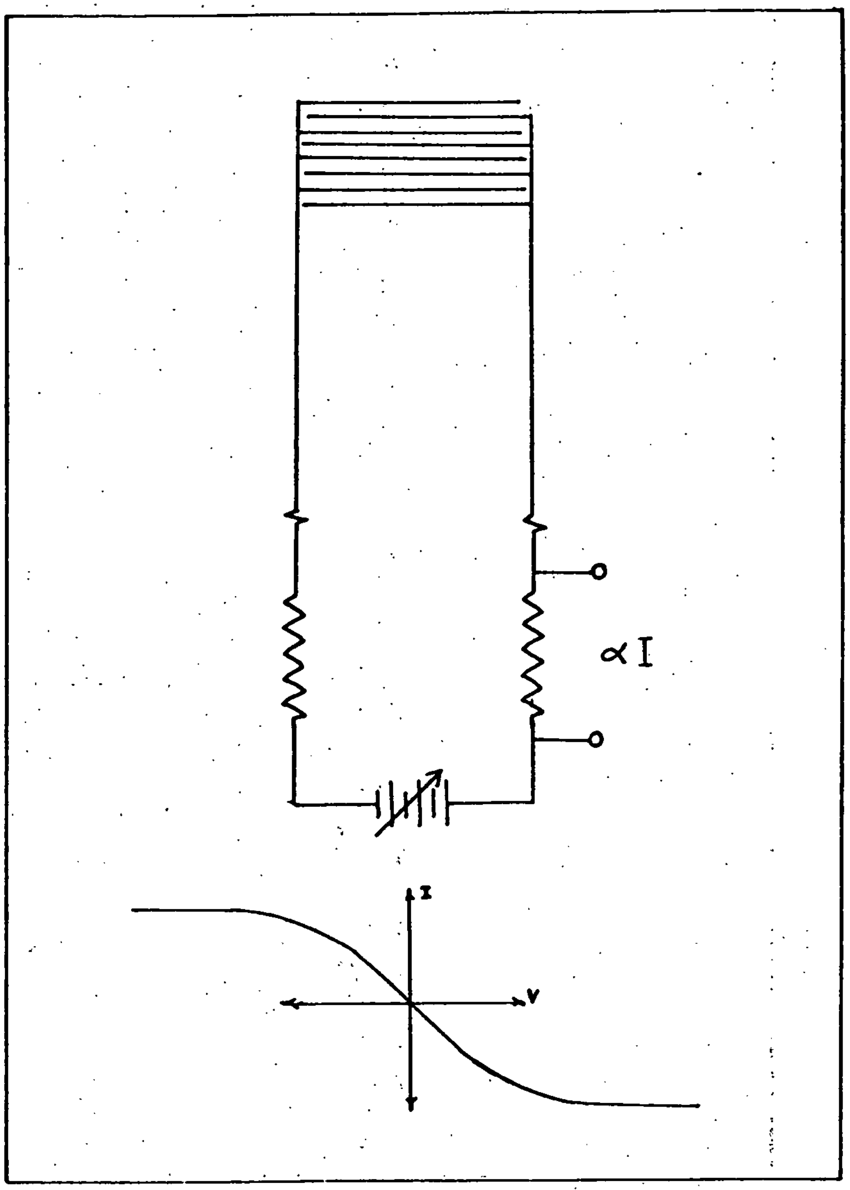

Debye sheath of each strip should only overlap the adjacent strips. For the densities where the traces become asymmetric, the Debye sheaths overlap several strips. To avoid this effect, the plasma density had to be kept above this critical density for the space of the flux measurements. This unfortunately limited the useful range of the striped particle collectors.

Electrostatic Energy Analyzer

The ion temperature in the plasmas studied was measured using a voltage swept gridded electrostatic energy analyzer that was constructed and described by Navratil.[19] Measured ion temperatures were found to be a function of the neutral pressure and range from about .5 ev at $8x10^{-5}$ torr., to .1 ev at $8x10^{-4}$ torr., the operating range of most of the experiments to be described. These results were for a helium plasma but similar results were found for a hydrogen plasma. These numbers are in rough agreement with the results of Brown[20] who also worked with a Lisitano source of about the same power input.

Collector Array

The collector array, used in experiments to be described, is shown in Fig. 3.5. The array strips are simply copper strips attached to mica insulators with epoxy, with each strip having a wire soldered to the back that is eventually brought out of the vacuum vessel. To measure the current out of each strip, one strip is shorted to the rest of the array through a small resistor and the voltage measured. Typically the resistor used is 100 ohms so that for the currents

Fig. 3.5: Diagram of the collector array used to measure the extent of the non-ambipolar outflow. There are fewer strips shown than actually exist in the real array.

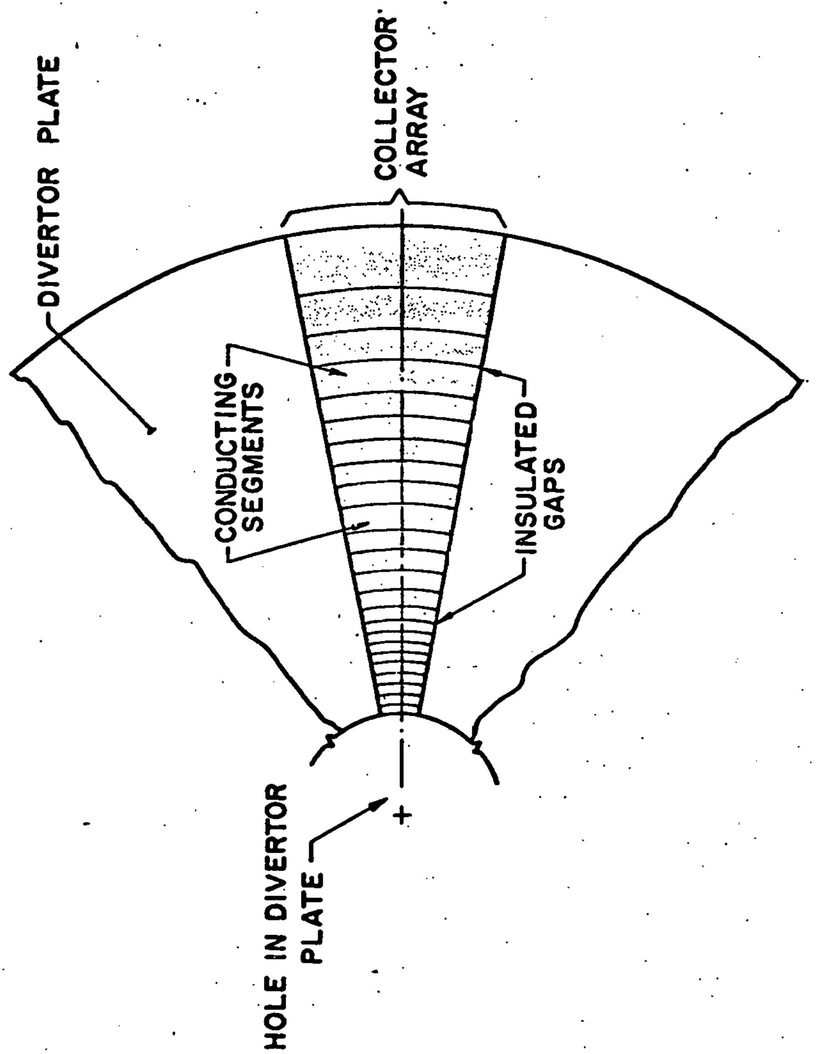

measured (usually tens of microamperes) the voltage offset introduced to the collector strip monitored is at most a few thousandths of a volt. Voltages of the order of volts would be necessary to seriously perturb the measurements. The array was chemically cleaned before mounting in the machine.

Electron Gun

An electron gun that could be inserted through a probe port was constructed in the early phases of these experiments, as a method of following certain characteristic field lines. The gun is shown schematically in Fig. 3.6. Accelerating voltages of up to 400 volts could be tolerated before arcing between the two cylinders occurred, with about 10 ma of current out of the gun. Firing the beam through 5 microns of neon gas was easily visible as a bright orange trace that followed the magnetic field lines. This gun is modeled after an earlier gun that was constructed by Paul Nonn.

Fig. 3.6: Cross sectional view of the electron gun showing A- the filament, B- the inner and outer accelerating cylinders, C- the support stalk, D- epoxy vacuum seals located as far away as possible from the hot filament, E- machine ground, F- alumina tube to support biasing wires, G- set screws so that top may be removed, H- biasing wires, I- Sauereisen cement as a high temperature insulator between cylinders.

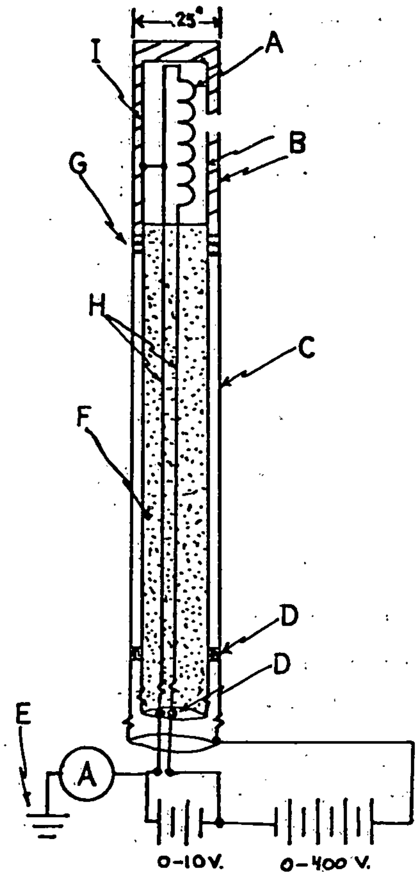

References-Chapter 3

1. I. Langmuir, in "Collected Works of Irving Langmuir", (G. Suits,ed.) Macmillan (Pergamon), New York 1961.

2. F.F. Chen, "Electric Probes" in *Plasma Diagnostic Techniques*, (R.H. Huddlestone and S.L. Leonard, eds.), Academic Press, New York (1965).

3. J.D. Swift and M.J.R. Schwar, *Electric Probes for Plasma Diagnostics*, Iliffe Books, London (1971).

4. P.M. Chung, L. Talbot and K.J. Touryan, *Electric Probes in Stationary and Flowing Plasmas: Theory and Applications*, Springer-Verlag, New York (1975).

5. J.C. Sprott, University of Wisconsin Plasma Physics Report P.L.P. 88, (1966).

6. D. Bohm, E.H.S. Burhop, and H.S.W. Massey, in *The Characteristics of Electrical Discharges in Magnetic Fields*, ed. A. Guthrie and R.K. Wakerling (McGraw-Hill New York, 1949), Chap. 2.

7. J.G. Laframboise, University of Toronto Institute of Aerospace Studies Report 100, (1966).

8. A.A. Sonin, A.I.A.A. Journal 4, 1588 (1966).

9. F.F. Chen, C. Etievant, and D. Mosher, Phys. Fluids 11, 811 (1968).

10. I.G. Brown, A.B. Compher, W.B. Kunkel, Phys. Fluids 14, 1377 (1971).

11. J.C. Sprott, D.E. Lencioni, and J.A. Schmidt, University of Wisconsin Plasma Physics Report P.L.P. 135 (1967).

12. J.F. Waymouth, J. Appl. Phys. 30, 1404 (1959).

13. G. Medicus, 5th Int. Conf. Ionization Phenomena in Gases 2, 1397.

14. E.W. Peterson, and L. Talbot, A.I.A.A. J. 8, 1391 (1970).

15. D.P.Grubb, Dept. of Nuclear Engineering, University of Wisconsin, Madison, Ph.D. Thesis, 1978.

16. D.W. Kerst, D. Lencioni, A. Cavallo, and J. Greenwood, Wisconsin Plasma Physics Report P.L.P. 709, (1977).

17. S.I. Mak, Dept. of Physics, University of Wisconsin, Madison, Ph.D. Thesis (1974).

18. E.R. Mosberg Jr., J. Appl. Phys. 40, 5290 (1969).

19. G.A. Navratil, Dept. of Nuclear Engineering, University of Wisconsin, Madison, Ph.D. Thesis (1976).

20. I.G. Brown, Plasma Physics 18, 205 (1976).

Chapter 4

Initial Investigations

As discussed in the first chapter, an essential ingredient in understanding the operation of a divertor and being able to predict its performance is the physics governing plasma flow in the scrape-off zone. In this zone plasma is not only diffusing across magnetic field lines but is also flowing parallel to the magnetic field into a neutralizing plate. These processes are common to all types of divertors; the purpose of the experiment described here is to investigate these features. While the plasma in our experiment has $T_e >> T_i$, which is the opposite of what one expects in a large Tokamak divertor experiment, and the neutral pressure is uniform (but roughly the same in magnitude as the pressure expected in the pumping chambers of these same Tokamaks) the results can contribute to the general understanding of the problem. In fact phenomena which can not be observed with diagnostics that only yield line averaged parameters, can be seen in our experiment because of our capability of using probes. On the other hand, phenomena such as unipolar arcs, ion sputtering, secondary emission or neutral pressure buildup resulting from plasma neutralization are beyond the scope of this experiment.

Our initial objective was the choice of an appropriate magnetic field configuration from the two described in chapter two, and to this end the configuration shown in Fig. 4.1 was initially chosen. The reason for the choice is twofold:

Fig. 4.1: Schematic of the magnetic configuration chosen for the divertor experiments. Indicated are the field nulls, and the initial collector plate location at E. The profile scans for the null leak experiment were also made across the field lines at E.

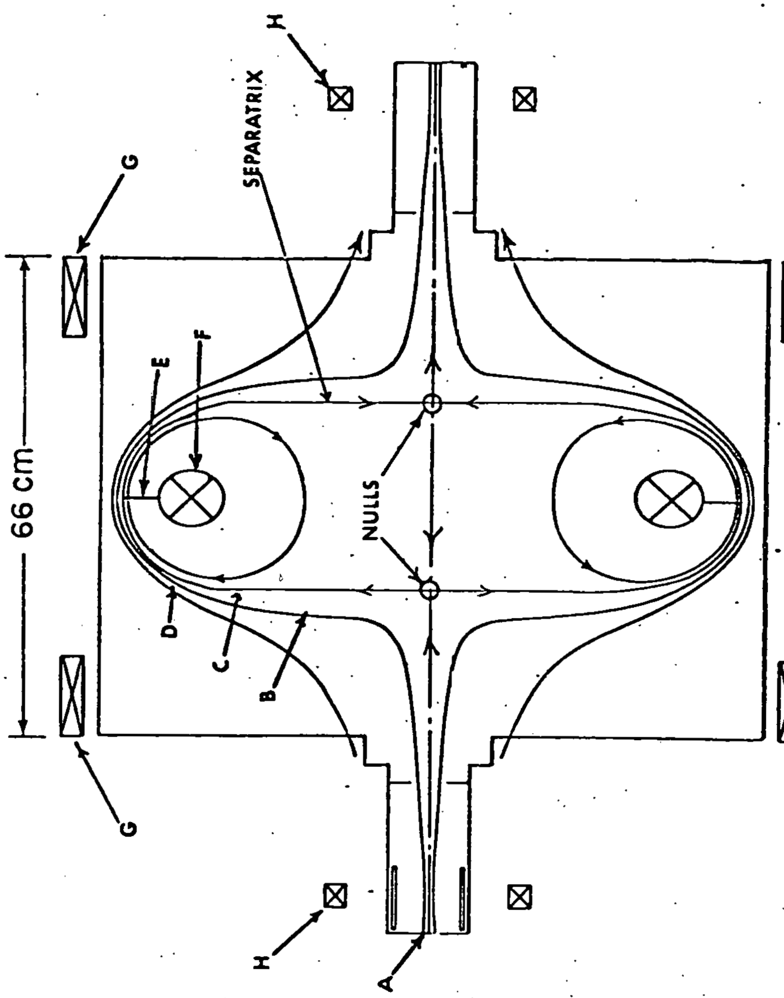

1. The configuration with the addition of the particle collector at E of Fig. 4.1 simulates a divertor. Some of the plasma diffuses across the separatrix, C, onto the field lines encircling the internal ring, F. These field lines intersect the metal neutralizing plate at E. This area simulates the scrape-off zone, while the field lines at B connected to the source simulate the main plasma region of the Tokamak. Our configuration is, in a sense, "inside-out" in comparison to the usual arrangement of the scrape-off zone on the outside of the main plasma in a Tokamak but this is not believed to be of any consequence. The essential transport problem of plasma diffusing onto field lines intersecting a neutralizing plate is modeled by our configuration.

2. The configuation is M.H.D. stable and the cross field diffusion coefficient has been measured. According to M.H.D. theory[1], a low beta plasma-magnetic field system is stable to interchange instabilities if

$$\left(\frac{dP}{d\psi}\right)\left(\frac{d}{d\psi}\left(\oint\frac{dl}{\underline{B}}\right)\right)>0 \qquad (4.1)$$

where P is the plasma pressure. A qualitative plot of P and $\oint\frac{dl}{\underline{B}}$ is shown in Fig. 4.2 which shows the stable nature of this configuration.(This diagram is based on the measured density profiles and the calculated field line integrals. The magnitude of each curve has been adjusted so they coincide for ease of comparison.) The

Fig. 4.2: Qualitative plot of P and $\oint d\ell/B$ versus ψ taken at E of Fig. 4.1.

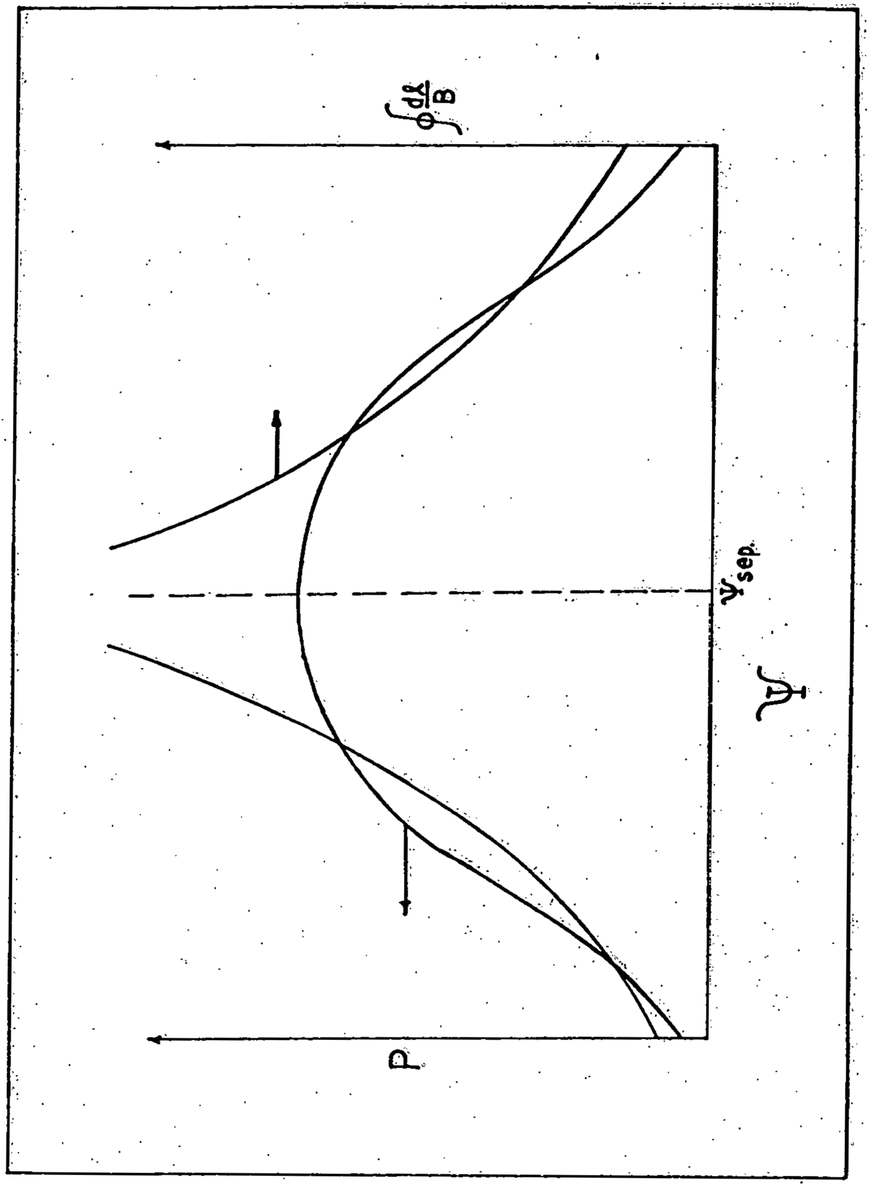

logarithmic divergence of $\oint\frac{dl}{B}$ at the separatrix is the result of carrying out the line integrals over the field nulls on the separatrix surface.

Further verification of the stable nature of this configuration comes from earlier work done on the D.C. machine.[2] The perpendicular diffusion coefficient was determined from an analysis of the measured steady-state density profile and from measurements of the radial plasma loss. The diffusion coefficient was found to be within a factor of two of the classical ambipolar coefficient for a partially ionized gas, indicative of the lack of instability driven diffusion. Experimentally, the absence of low frequency fluctuations confirms the stablity of this configuration.

An M.H.D. stable plasma configuration is an obvious necessity if one wishes to study divertor phenomena and not gross M.H.D. instabilities. From a practical experimental point of view, the large fluctuations associated with M.H.D. instabilities would greatly complicate the acquisition of data by any means. Furthermore, future devices will be designed to have M.H.D. stability at least. (Removing the plasma with the divertor plate may invalidate the concept of average good curvature, because it can interrupt the parallel electrical current between regions of good and bad curvature. Thus evaluation of the M.H.D. stability of a given configuration may await experiment.) Also knowing $D_\perp$ from Ref. 2 enables one to attribute any change in the diffusion coefficient to the interaction of the particle collector with the plasma and provides a basis of comparison.

Field Null Plasma Leak Experiments

Prior to the installation of the divertor plate and the start of any divertor experiments, the effect of the field nulls on cross field plasma transport to private field lines was assessed. Field nulls are also a feature of bundle divertors and toroidal divertors have a near null, in that the weaker poloidal field is still present at the toroidal null. Field nulls have been shown[3] to allow cross field transport due to nonadiabatic particle motion at the zero of the field, which might conceivably be greater than the cross field transport over the separatrix magnetic surface.

It was decided that the easiest way of experimentally assessing the magnitude of the plasma leak through the null would be to eliminate it and observe the change on plasma profiles inside the separatrix. If the nulls provide a source of plasma inside the separatrix that is a large fraction of the cross field diffusive source, the profiles should change substantially if the nulls are shielded from impinging plasma. Our method of achieving this was simply to insert metal disks between the null and the plasma source outside the separatrix so that plasma could not reach the field nulls.

The first order of business was the location of the field nulls inside the device. Initially the null was roughly located using the electron gun fired through a background of neon gas. When the gun sat on the separatrix, because of the finite width of the beam, a trace could easily be observed following field lines on either side of the null. The null was roughly half way between the traces. A more precise null location was obtained by letting the machine up to air and searching for simultaneous zeroes in the axial and radial fields with a Hall probe. The null located in this fashion was compared with the null location predicted from a computer routine that searched for the null on axis. At first the two didn't agree, but it was discovered that the front panel meter of the Magnaflux was reading 140% of the actual current value. When this was corrected the two agreed to within a few mm, an error easily explained by coils that are not the somewhat idealized current filaments that are used in the code.

A stainless steel disk was therefore mounted on an alumina stalk to act as a null blocker, and fashioned is such a way that it could be moved from the null while the machine was under vacuum. The disk was 4 cm in diameter and centered on the null. The largest leak near a field null occurs at the null. However, even near the null particle orbits are such that they may cross the separatrix.[1] To affect the null source as much as possible, the disks were made large to block those particles whose orbits make large excursions across the separatrix according to the theory of Schmidt in Ref. 1.

Plasma parameter scans with and without the null blocked where made across the magnetic field at E of Fig.4.1. The density profiles in these two cases are shown in Fig. 4.3. The important point to note is that the shape of the profiles is the same, which is not what one

Fig. 4.3: Density scans before (upper curve) and after the magnetic field nulls were blocked.

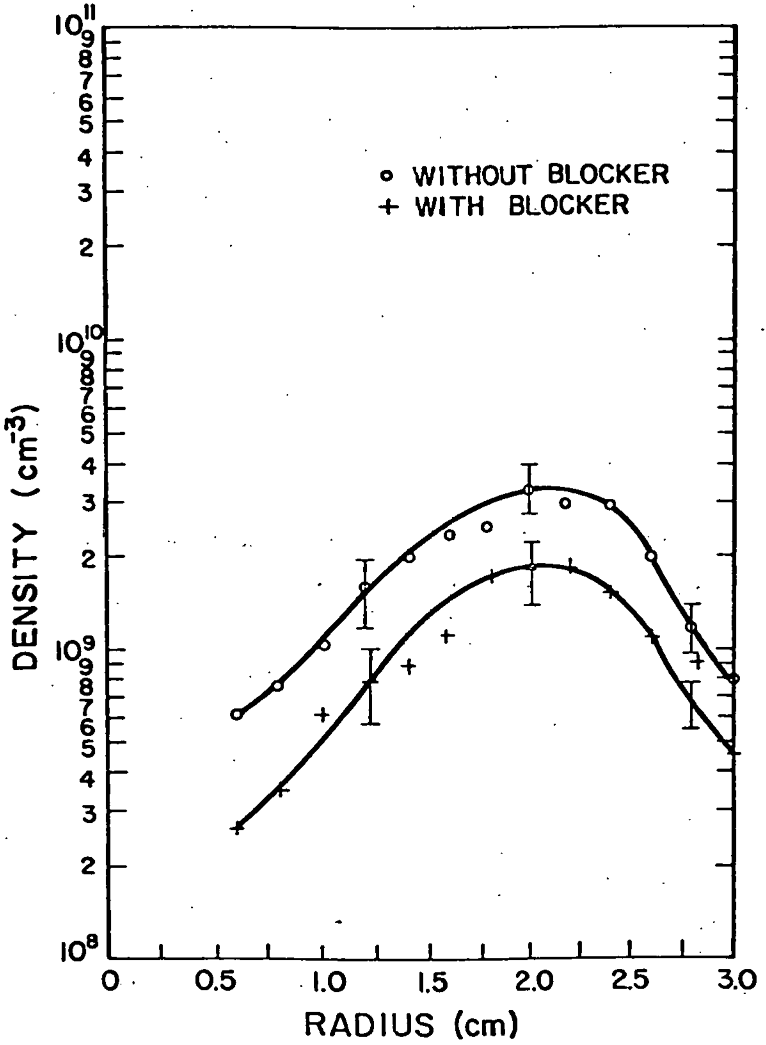

would expect if the nulls were a significant source of plasma. It was suspected that the Lisitano source was perturbed by the disk's supporting stalk where it crossed the separatrix; this would explain the lower relative density. To insure that this was indeed the case, a probe was constructed with a stalk of the same size as that of the null blocker support, but that was just long enough to cross the separatrix with no disk at its end. Density scans with the test probe inserted and withdrawn demonstrated that the lower relative density was due to the plasma source being perturbed. The mechanism by which the stalk perturbs the Lisitano source is not well understood, but the stalk may short out electric fields inside the source that are critical to its operation.

The validity of concluding that the null is not acting like a plasma source can also be seen by a rough calculation. The particle current Γ_1 escaping through a point cusp is given by[4]

$$\Gamma_1 = n \, \pi \, \rho_i \, \rho_e \left(\frac{kT_e}{M_i}\right)^{1/2}, \qquad (4.2)$$

where ρ_i and ρ_e are the ion and electron gyroradius evaluated at the cusps field maximum, n is the ion density, T_e is the electron temperature, M_i is the ion mass, and k is Boltzmann's constant. (This calculation assumes that in the steady state, the cross field transport into the cusp balances the flow out.) For our parameters

($\underline{B}\simeq 100$ G, $\rho_i \rho_e \simeq .05$ cm^2, $T_e \simeq 5$ eV, $T_i \simeq .1$ eV) $\Gamma_1 \simeq 3\text{x}10^{15}$ particles/sec. The diffusive particle current, Γ_2, is given by

$$\Gamma_2 = (-D_\perp \nabla n)A_{sep}, \tag{4.3}$$

where $D_\perp$ is the perpendicular diffusion coefficient and A_{sep} is the area of the separatrix magnetic surface. Using classical diffusion due to ion-neutral collisions with our experimental parameters, $\Gamma_2 \simeq 7\text{x}10^{16}$ sec^{-1}. Thus the diffusive transport is better than an order of magnitude greater than the non-adiabatic transport for a conservative choice of parameters.

Having determined that the nulls are a negligible source of plasma, collector plates were installed around the outer periphery of the internal ring, as shown at E of Fig. 4.1. The collector was made of aluminum and electrically isolated from the internal ring. Alignment of the edge of the collector was again accomplished with the help of the electron gun. Measured profiles on field lines that intersect the collector showed a significant change from the profiles taken before mounting the collector, and behaved consistently with the collector acting as a particle and energy sink as expected. Our investigations of the plasma behavior in this arrangement of the collector ended here for a number of reasons. First of all, the profiles in the scrape-off zone evolve in the space of only about a centimeter, which is about ten probe tip diameters. Thus gradients in density and temperature are not negligible over the diameter of the probe, and some spatial averaging is inevitable. Secondly, the high magnetic field (800 G.) in this area makes the applicability of the theory of Laframboise doubtful (i.e. $\rho_i \simeq .6$ mm, $\rho_e \simeq .1$ mm, and therefore $\rho_e < \rho_i << D_p$ the probe tip diameter). Finally, because so few points are obtainable in the course of completing a profile, experimental uncertainty makes the profile shape less determinate.

The solution to all of these problems is to allow the same field lines to intersect the collector plate, but to place the collector plate inside the internal ring as shown in Fig. 4.4. Now the average magnetic field strength drops to around 20 G. ($\rho_i \simeq 2.5$ cm, $\rho_e \simeq 1.1$ mm, and importantly $\rho_i >> D_p$.) In addition, the resulting spreading of the field lines means the profiles evolve in tens of centimeters instead of just one centimeter. The problem of aligning the collector plate with the separatrix magnetic surface is avoided entirely, as the magnetic field now defines the scrape-off zone.

The plate itself is again solid aluminum, cleaned with Oakite before insertion into the vacuum chamber. Electrical isolation is provided by Teflon supports inside the internal ring, that also hold the plate in place, and allow the plate to be biased with respect to machine ground. To completely eliminate any effects of null scattered particles, a ten centimeter hole was cut in the center of the plate. Those field lines nearest the null, and thus most likely to have null scattered particles on them[5], do not strike the plate and they must again be diffusively transported to the experimental region in front of the plate. An additional advantage of the hole is that the

Fig. 4.4: The final configuration of magnetic field and collector chosen for the divertor studies. Shown are: A-Lisitano source, B&D- source plasma on non-diverted field lines, C-separatrix magnetic surface, E-collector plate location, F-internal ring, G-Helmholtz coils, H-end or mirror coils.

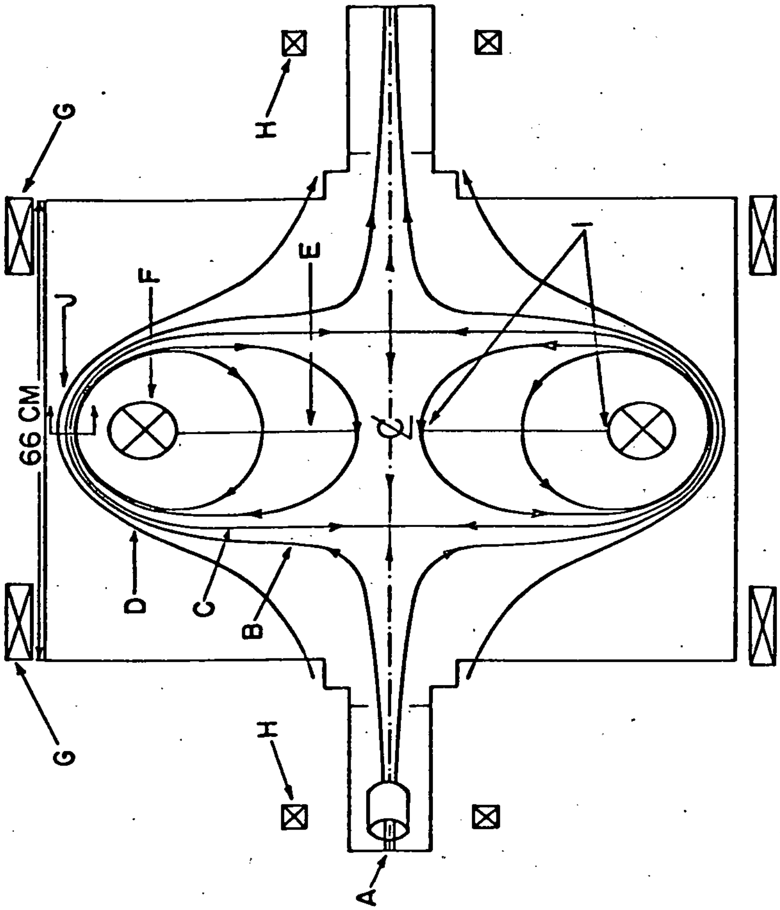

juxtaposition of field lines that do and do not strike the collector plate allows study of phenomena that occur in the transistion of diverted to non-diverted plasma. This transition from closed to open field lines also better models a Tokamak divertor, where this transition occurs too. All of the data presented in the rest of this thesis was taken with the machine in this configuration.

References-Chapter 4

1. G. Schmidt, Physics of High Temperature Plasmas, Academic Press, New York, p. 138 1966).
2. D. Meade, and R.J. Fonck, Phys. Fluids 16, 1654 (1973).
3. J. Sinnis, and G. Schmidt, Phys. Fluids 6, 841 (1963).
4. I. Spalding, in Advances in Plasma Physics Vol. 4, edited by A. Simon and W.B. Thompson, Interscience, New York, 79 (1971).
5. G. Schmidt, Phys. Fluids 5, 994 (1962).

Chapter 5

Divertor Experiments

For reasons discussed in the previous chapter, the configuration of magnetic field and collector that is used throughout these experiments is the one shown in Fig. 5.1. All of the parameter profiles to be shown were taken between the arrowheads at letter I in Fig. 5.1, parallel to the collector plate and about 2.5 cm away from the plate axially with a spherical tip Langmuir probe. The center line shown in Fig. 5.1 is the origin of the coordinate system used, and the edge of the collector plate is at r= 5 cm with increasing r as one moves towards the internal ring. Hydrogen and Helium plasmas were used for the majority of the data to be presented, and because the results obtained did not differ qualitatively, but only quantitatively in ways attributable to mass difference, the plasma used in each case is specified only when such a mass dependent difference occurs. Shown in Table 5.1 are typical parameters in the experiment region. The ion temperature for the experiments discussed was measured with a gridded electrostatic analyzer, and found to range from .1 to .5 eV and depend depend only on the neutral density. This is in rough agreement with a previous spectroscopic determination of T_i.[1]

For comparison purposes, a profile of density, n, and electron temperature, T_e, was taken before the installation of the divertor collector plate and is shown in Fig. 5.2. Figures 5.3 and 5.4 show profiles of the electron temperature, floating potential, ϕ_f, and

Fig. 5.1: The configuration chosen for the divertor studies showing: the region that all the parameter scans in this chapter were taken in (i.e. between the arrowheads), J- the region of the first collector plate.

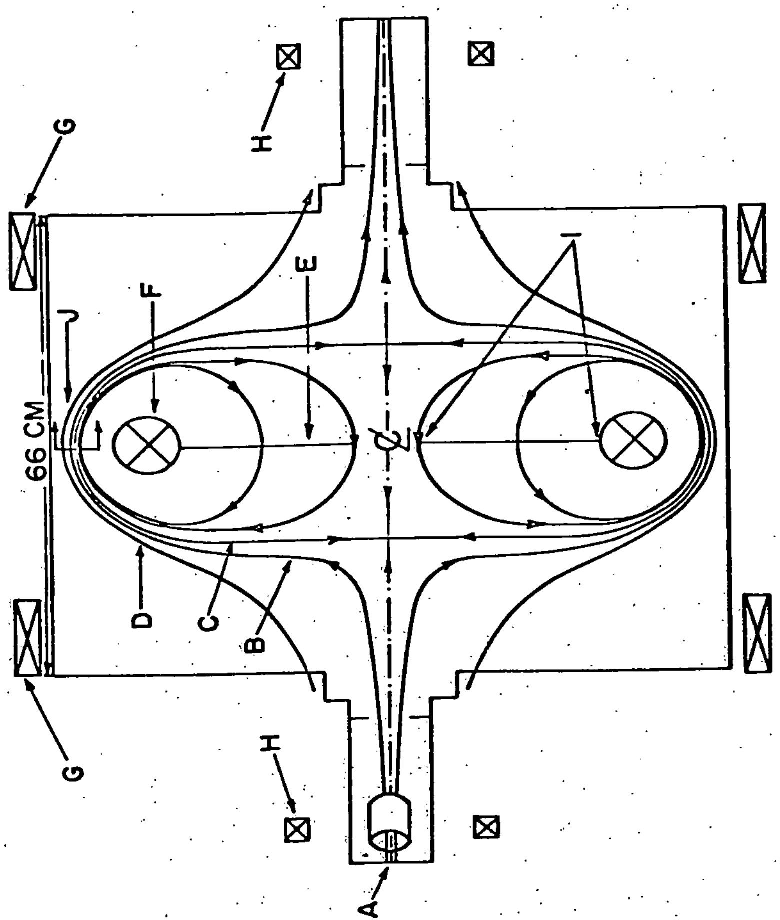

Table 5.1

Plasma Parameters in the Experiment Region

Neutral Density ~ 10^{12} - 10^{13} cm^{-3}

Plasma Density ~ 10^{8} - 10^{9} cm^{-3}

Electron Temperature ~ 5 - 10 eV

Ion Temperature ~ .1 - .5 eV

Electron-Neutral Mean Free Path ~ 300 cm

Ion-Neutral Mean Free Path ~ 18 cm

Debye Length ~ .2 mm

Electron Gyroradius ~ 1.1 mm

Ion Gyroradius ~ 2.5 cm

Average $\underline{B}$ ~ 50 G

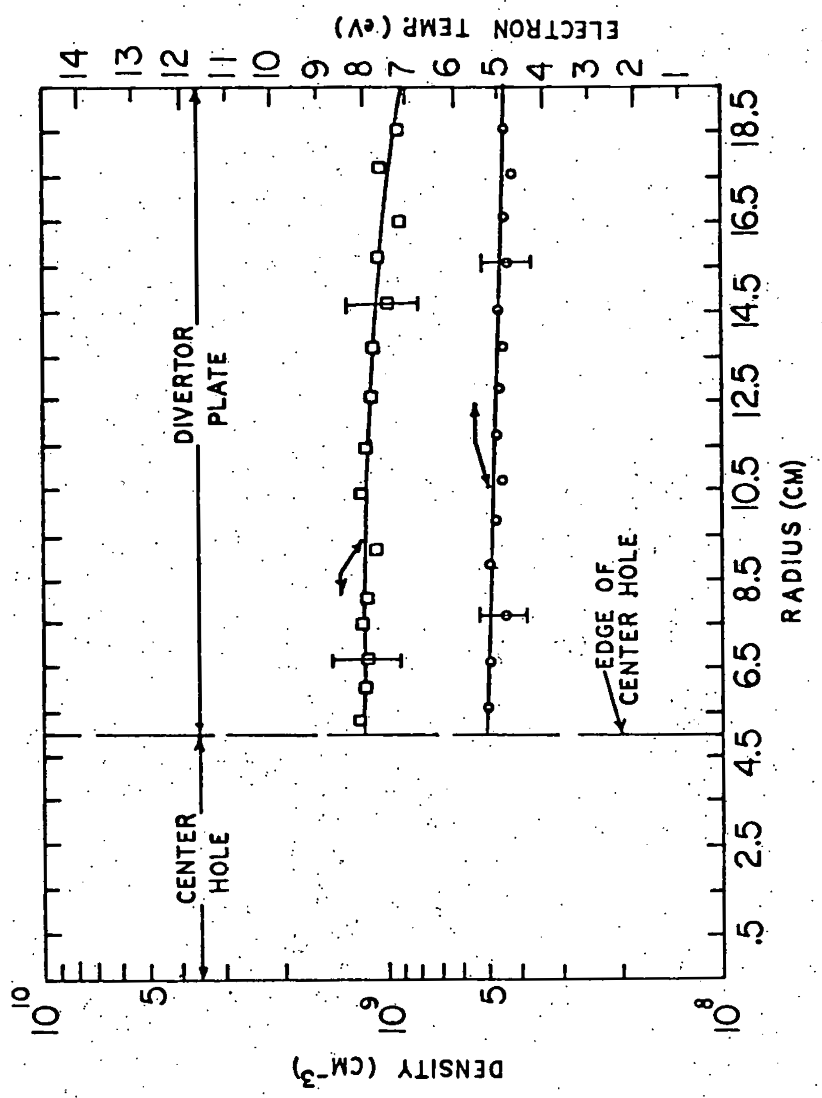

<u>Fig. 5.2:</u> Density and electron temperature before installation of the divertor plate.

Fig. 5.3: Electron temperature and floating potential after the installation of the plate.

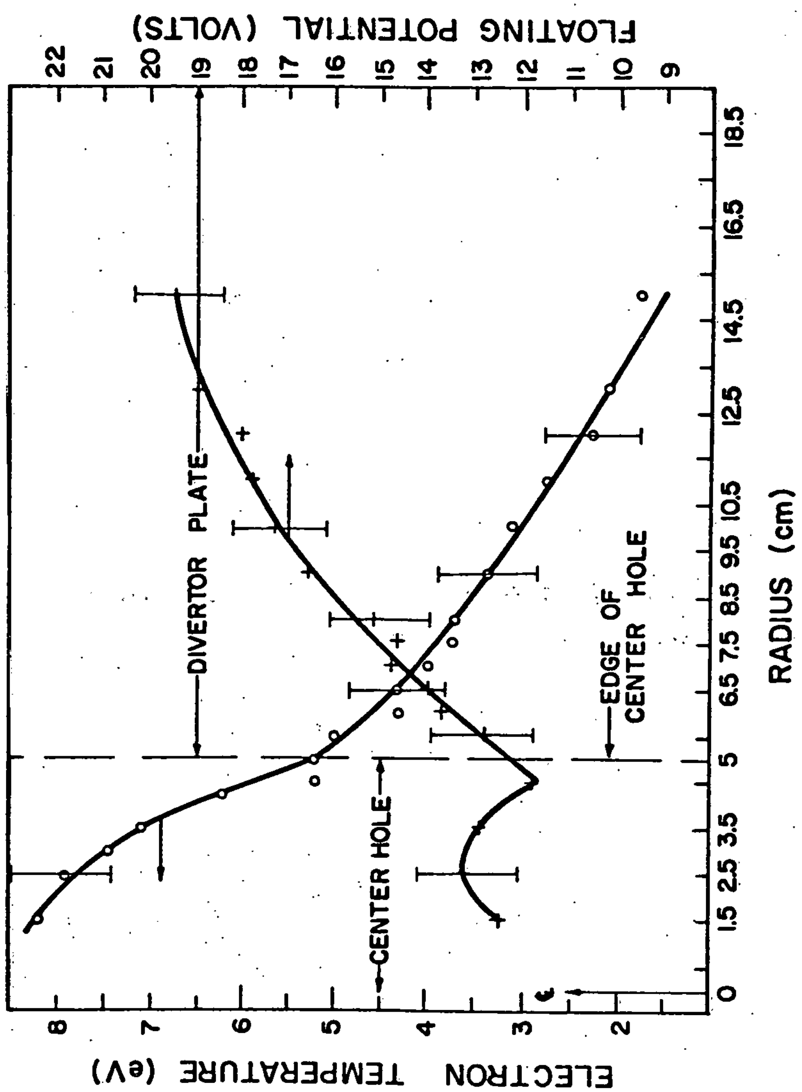

Fig. 5.4: Plasma density after the installation of the collector plate.

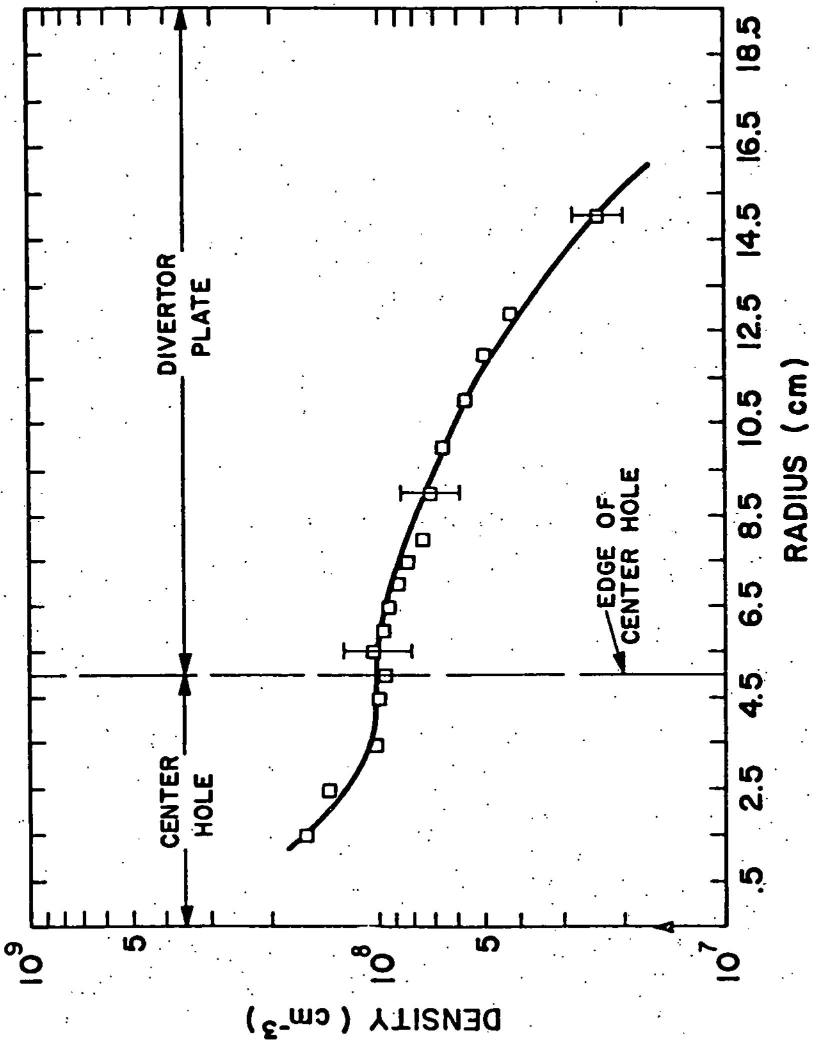

density in the experiment region with the divertor plate in place. These profiles are symmetric about the axis of the machine and are identical on opposite sides of the collector plate.

The density and temperature show the expected decay, due to the collector plate acting as a particle and energy sink, in comparison with the no collector case. The significance of the floating potential contour is most easily seen if one considers the difference $\phi_{fp} - \phi_{fc}$ vs. radius, where ϕ_{fp} is the floating potential of the probe and ϕ_{fc} is the potential the plate assumes. This difference is plotted in Fig. 5.5. On a given field line, when $\phi_{fc} = \phi_{fp}$, equal fluxes of ions and electrons strike the collector plate where this field line passes through the plate. (We are assuming here that the probe floating potential on a given field line is a good measure of the potential that the collector would have to assume on this same field line so that it too would locally collect no net electrical current. The potential which a body immersed in the plasma must assume so that the fluxes of ions and electrons are equal is the definition of the floating potential). To lowest order, when $\phi_{fp} = \phi_{fc} = \Delta\phi$ is not equal to zero, unequal fluxes of ions and electrons will strike the plate and the parallel flow is nonambipolar. When $\Delta\phi > 0$ more ions than electrons flow along field lines to the collector, and vice versa for $\Delta\phi < 0$. These areas are indicated in Fig. 5.5. Whenever there is non-ambipolar parallel flow, the steady state continuity equation implies that there is also non-ambipolar cross field transport.

Fig. 5.5: The quantity $\Delta\phi$ vs. radius with the plate installed.

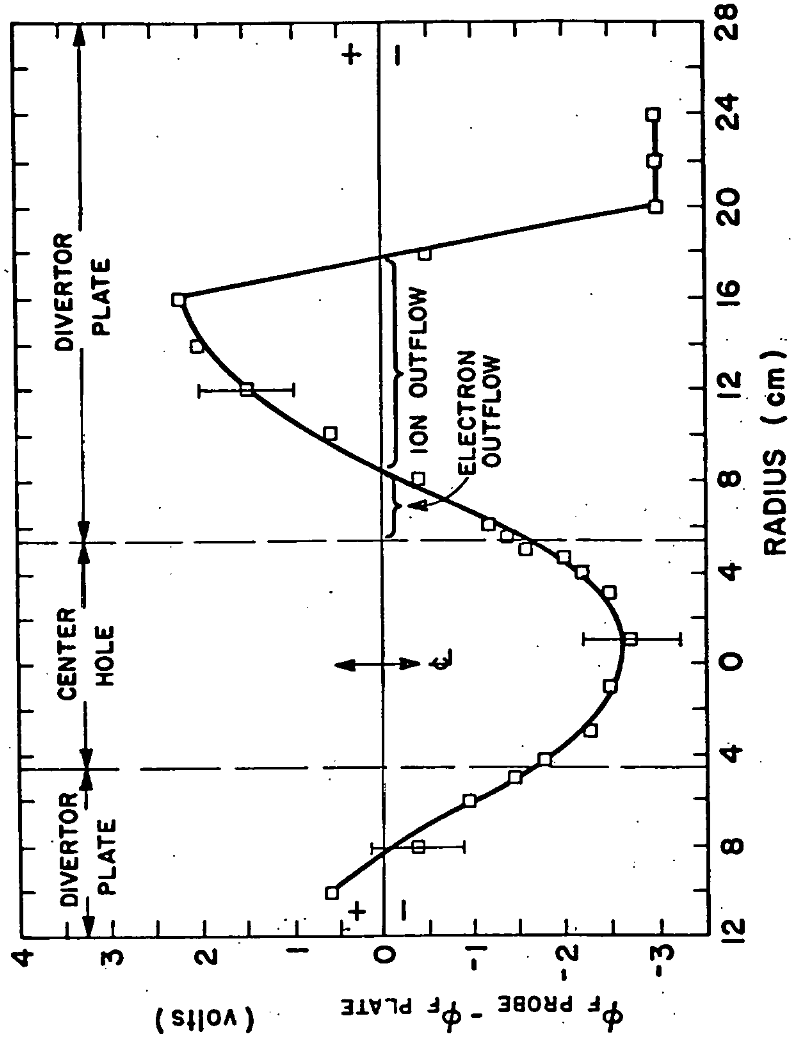

Several assumptions are implicit in the above discussion. These assumptions will add small corrections to Fig. 5.5 but not change the conclusions of this section. One assumption is that the electron temperature is constant along the portion of the magnetic field line that passes between the probe and collector. This is certainly true because the electron mean free path (= 300 cm) is much greater than the 2.5 cm distance between collector and probe. (This was also verified by measurement of the electron temperature at the collector plate.) Two other approximations are inherent in the above discussion. The first is that there is no offset in the floating potential of the probe or collector; such an offset could be caused by impurities on the surface of the probe or collector. The second is that the spherical probe tip will assume the same floating potential on a given field line that a plane collector would. In other words it is assumed that there are no geometrical effects that will cause a spherical and planar probe to float at different potentials in the same plasma. Of course, both of these effects do exist but the question to be answered is how severe they are. Presumably if either of these effects is large enough the existence of non-ambipolar flow is in question.

Perhaps the easiest way to assess the magnitude of these two effects is to attempt to remove them. In order to eliminate these sources of error, it was decided to try to measure the net current to the collector plate as a function of radius rather than infer it from the floating potential with all of its possible errors. To preserve overall charge neutrality, the collector plate must conduct excess electrons from the electron outflow region to the area of net ion outflow. This neutralizing current was detected directly by mounting an array of conducting strips on the divertor plate but insulated from it; this is shown schematically in Fig. 5.6. The array of strips was intended to act as any typical section of the collector plate would, with the added feature of allowing the current that flows within the plate to be measured. The separation between strips is less than the local Debye length. Each segment could be individually shorted to the rest of the array through an ammeter to measure I_{net}, the net current to the segment. This concept is illustrated in Fig. 5.7. Figure 5.8 shows the net current measured by this method as a function of radius, and Fig. 5.9 shows the current density to the strips. The latter is shown to compensate for the differences in the areas of the individual collector strips. One notes that this method of measuring the non-ambipolar parallel current has the same gross features as the plot of $\Delta\phi$ vs. r. (There are however small differences that will be discussed shortly.) It is found that the current outflow summed over the array equals zero as expected. A measure of the degree of non-ambipolarity of the parallel flow in regions of a given sign of I_{net} can be indicated by the ratio I>/I<, where I> is the dominant current of one species and the I< the smaller current of the other species. (For example where $I_{net}>0$, I> is the ion current and I< the electron current.) Using simple probe theory to infer I> and I< from the locally measured plasma parameters and the measured sheath potential drop, I>/I< ranges from 1 to 5 in both outflow regions.

Fig. 5.6: The segmented collector used to measure I_{net}.

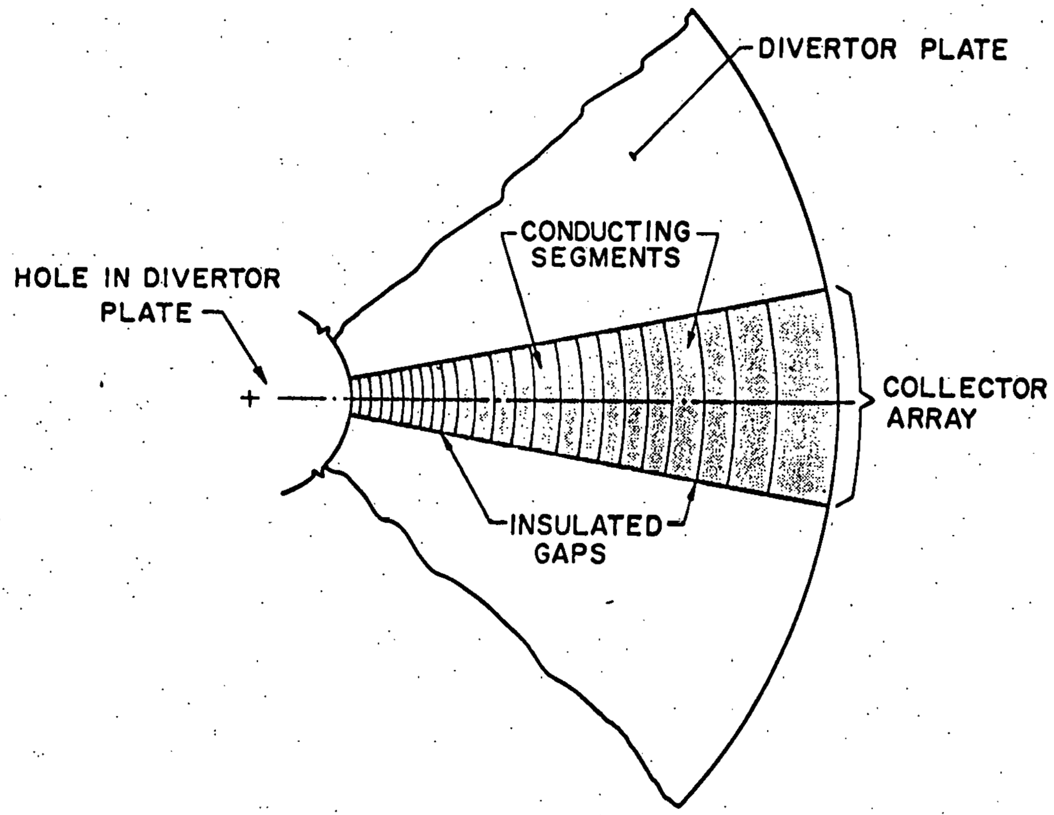

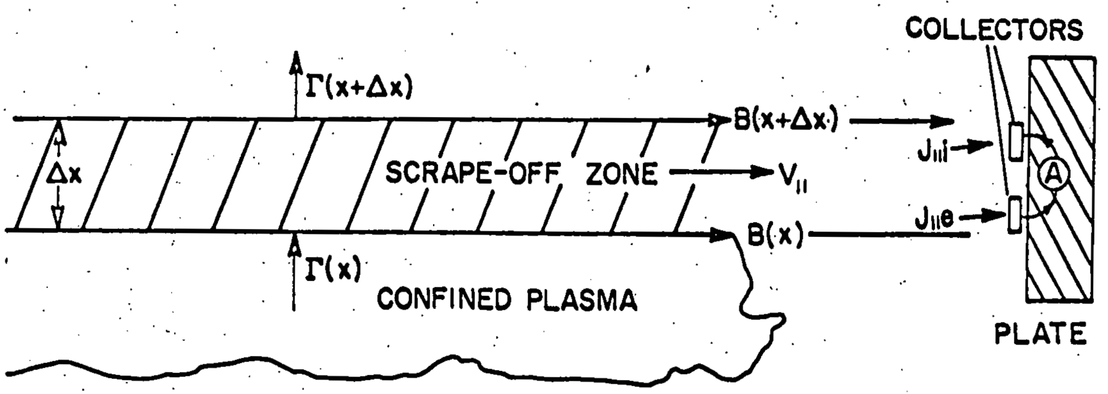

Fig.5.7: The scrape-off zone showing non-ambipolar current flow into and through the array, and the schematic location of the ammeter to measure the net current.

Fig. 5.8: Net current to an array segment vs. radius.

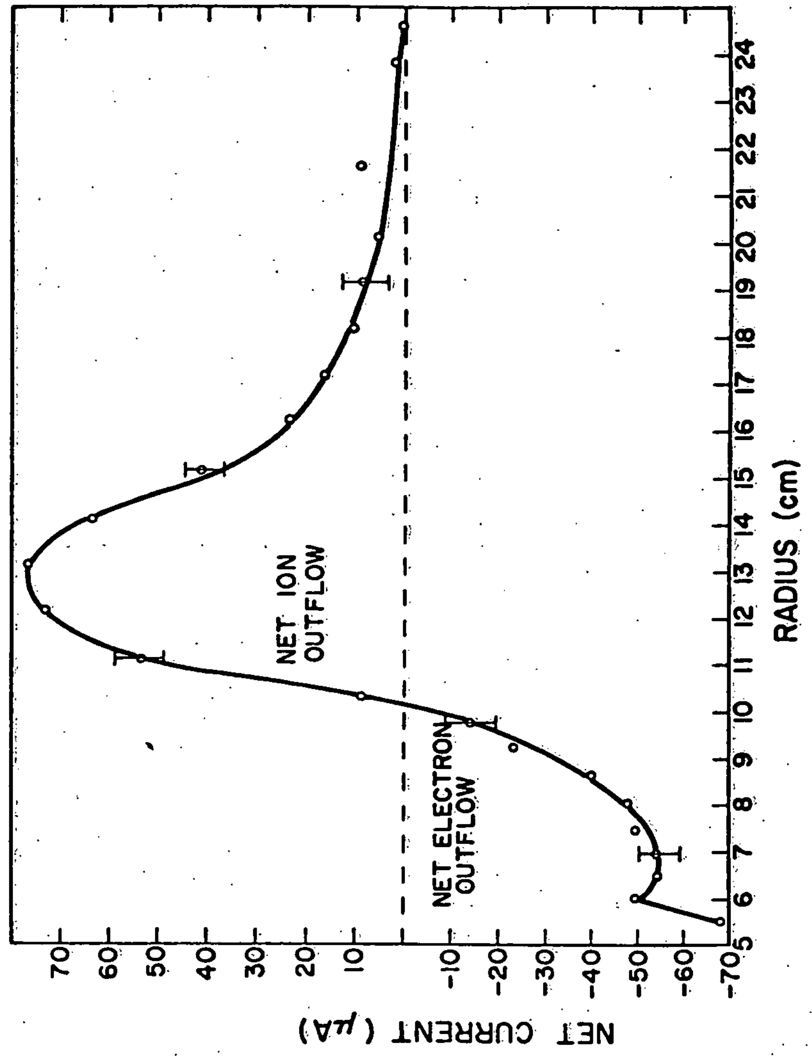

Fig. 5.9: The net current to an array strip divided by its area as a function of radius.

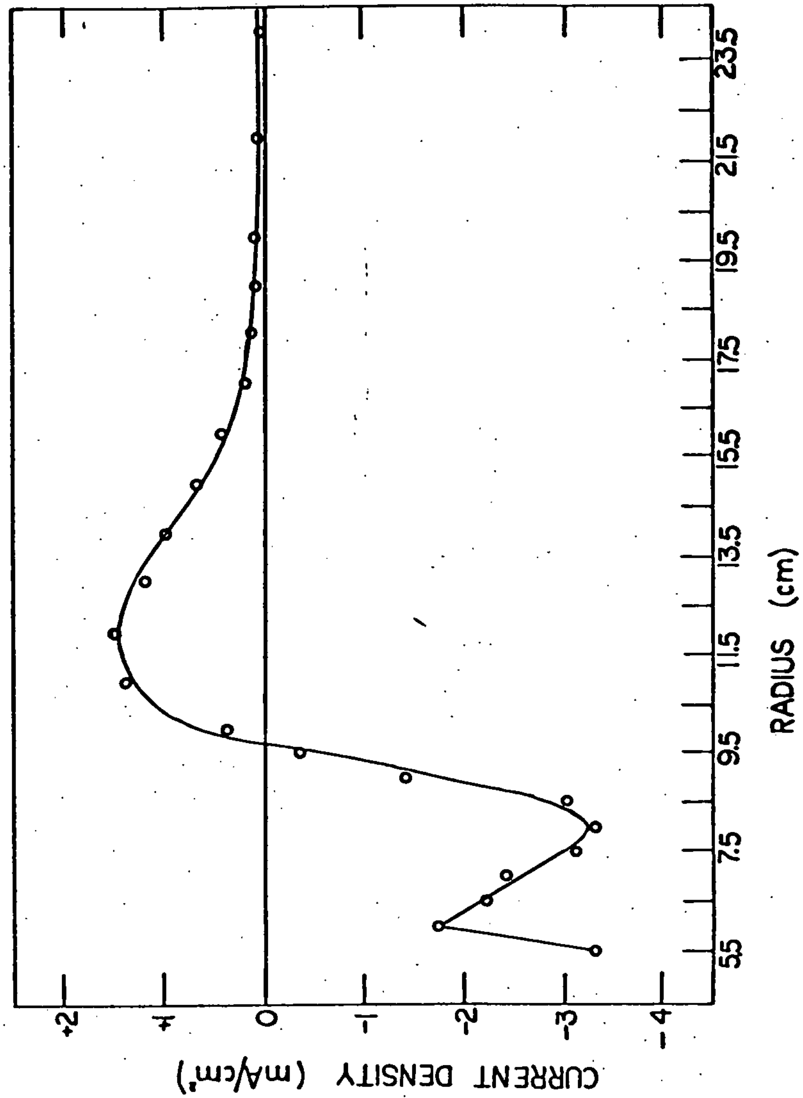

One consequence of this unequal charge outflow is a monotonically increasing value of the parameter η (η=sheath potential drop/electron temperature) as one moves deeper into the scrape-off zone. The experimentally determined sheath drop is deduced from the relationship

$$\phi_p = \phi_{fp} + \alpha T_e, \tag{5.1}$$

where ϕ_p is the plasma potential, ϕ_{fp} the measured probe floating potential and α a constant that depends on the ion and electron mass, and the shape of the probe.[3] The sheath drop ϕ_s is then

$$\phi_s = \phi_p - \phi_{fs} \tag{5.2}$$

where ϕ_{fs} is the potential of the collector segment that the probe is in front of. In the present case all the strips are at the same potential. Dividing by the measured value of T_e gives η , and this is shown as a function of radius is Fig. 5.10. The electron flux through the sheath is determined by

$$\Gamma_{\parallel e} = n(\frac{kT_e}{2\pi m_e})^{1/2}\exp(\frac{-e\phi_s}{kT_e}) \tag{5.3}$$

and thus the electron flux through the sheath is exponentially dependent on η . The horizontal line in Fig. 5.10 is drawn at the

Fig. 5.10: $\eta = e\phi/kT_e$ vs. radius.

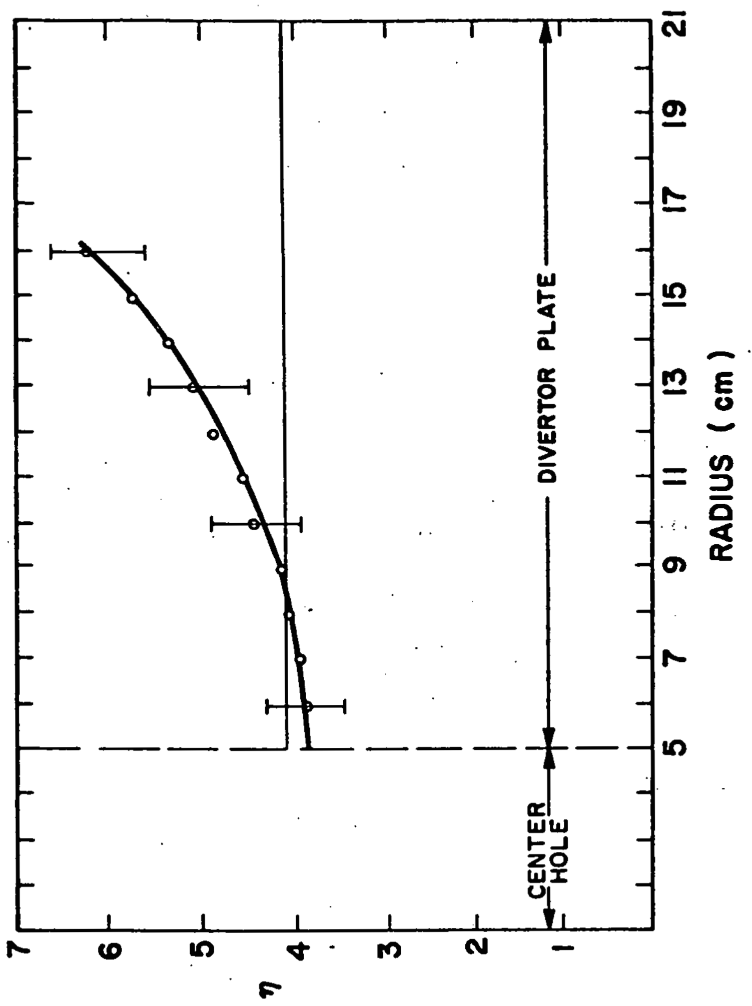

value of η where the electron flux equals the ion flux, and thus again the electrons can reach the plate in greater numbers than the ions at small radii, but are electrostatically constrained from reaching the plate at large radii. (The pre-sheath potential drop is relatively unchanged across the scrape-off zone, and thus so is the ion acoustic velocity of the ions. Therefore the ion motion is relatively unaffected as compared to the ambipolar case.) One still has charge neutrality outside of the sheath in this region. The location of the horizontal line is determined by the value of α for a plane collector, and it is only when the curve of η vs. radius intersects this line that ambipolar flow occurs. That is when

$$\left[\frac{(\phi_{fp} + \alpha T_e) - \phi_{fs}}{T_e}\right] = \alpha', \qquad (5.4)$$

where α is the value of the constant appropriate for a spherical collector, and α' for a plane collector. To understand equation 5.4 note that if an array strip is floating, then equation 5.1 is applicable to both collector strip and floating probe on the same field line if the appropriate values of α are used for each. That is either can be used to deduce the plasma potential when the proper value of α is used. In this case one can write

$$\phi_p = \phi_{fs} + \alpha' T_e = \phi_{fp} + \alpha T_e. \qquad (5.5)$$

Subtracting ϕ_{fs} from both sides, and dividing by T_e yields the value of α for a floating strip, which is equation (5.4). The predicted outflow regions as measured by this method agree well with the values shown in Fig. 5.8.

The magnitude of the measured net current at each strip of the array is found to be in good agreement, that is well within the experimental uncertainty, with the value calculated using the measured value of α in the simple probe theory equation

$$I_{net} = nA_{strip}e[(\frac{kT_e}{m_i})^{1/2} - (\frac{kT_e}{2\pi m_e})^{1/2}\exp(-\eta)], \qquad (5.6)$$

which assumes collection of the ions at the local ion acoustic velocity. In this formula the density, n, the electron temperature, T_e, and the floating potential, ϕ_f, are measured by sweeping each strip through its I-V characteristic, as it is allowed to electrically float away from the array. Table 5.2 shows the comparison of the measured net current and the calculated current using the measured value of the sheath potential drop. The correct value of η is again calculated using equation 5.1. The value of α can be experimentally determined by varying α in equation 5.6 until a best fit with the data is obtained; the best fit value is found to agree well with the value of α from simple probe theory

Table 5.2

Comparison of Measured Net Current to the Array Strips Vs. Calculated Net Current

Collector #	Measured Current (A.)	Calculated Current (A.)
2	-6.68×10^{-4}	-8.09×10^{-4}
4	-1.15×10^{-3}	-1.5×10^{-3}
6	-1.77×10^{-3}	-1.28×10^{-3}
8	-1.17×10^{-3}	-1.4×10^{-3}
9	-4.83×10^{-4}	-1.64×10^{-4}
11	$+2.02\times10^{-3}$	$+1.67\times10^{-3}$
14	$+1.88\times10^{-3}$	$+1.28\times10^{-3}$
15	$+1.42\times10^{-3}$	$+1.28\times10^{-3}$
17	$+5.0\times10^{-4}$	$+3.34\times10^{-4}$

$$\alpha = \frac{1}{2}\,\ell n\left(\frac{\pi m_e}{2 m_i}\right).$$

It is interesting to return briefly to the method that compares the floating potentials of probe and array to detect non-ambipolar flow, and compare it to the direct current measurement that is not subject to the errors of the former. Comparison of Figures 5.5 and 5.8 reveals that the two methods don't agree as to the exact spatial extent of the outflow regions. Because the current measurement method detects the unequal outflow directly, possible sources of error in this technique are external to the experiment (i.e. in the measuring apparatus) and can be eliminated. Therefore it is natural to ask where the sources of error arise in the method that relies on the comparison of floating potentials of the array and probe. Of the possible sources of error that were mentioned earlier, let us consider the effects of impurities first. First, no amount of ion bombardment cleaning of the probe or array caused the observed offset in these two methods of detecting non-ambipolar flow to decrease. Cleaning was often tried for periods of twenty minutes or more with no effect. Electron bombardment cleaning was tried as well,often heating the probe to incandescence, with no effect. Sweeping the probe through its I-V characteristic rapidly has been mentioned in the literature as a means of detecting the presence of impurities on a probe surface.[4] Any discernable hysteresis in the characteristic indicates an impurity layer on the probe. The probe was swept at various frequencies and no hysteresis was observed. There are undoubtedly some impurities on the probe and array, but we conclude from the above observations that they have a negligible effect on the measurement of the floating potential.

Geometrical differences can also cause two objects in the same plasma to float at different potentials. Fig. 5.11 is reproduced from Laframboise[3] and shows a dimensionless ion current $i^{\pm}$ to a spherical probe on the ordinate vs. dimensionless probe potential on the abscissa. Each curve is parametrically dependent in addition on the ratio R_p/λ_d, the ratio of the probe radius to the Debye length. Also plotted on the graph, shown with a dashed line, is the electron current in the retarding region that is given in equation 5.3. The intersections of these two curves mark the dimensionless potential where no net current strikes the probe. This value of $e\,\phi_f/kT_e$ is nothing more than the value of α for a given R_p/λ_d. Note too that as R_p/λ_d gets large, the intersection of the electron and ion currents moves to the right on the curve, and approaches the value 4.22 which is the simple probe theory estimate for alpha. This is exactly the limit that one would expect intuitively. Thus the correct alpha to choose for a given dimension of one's probe tip depends on the comparison of this dimension to a characteristic scale length of the plasma, namely the Debye length. A spherical probe becomes, in a sense, like a plane as far as the plasma is concerned only when the probe size is much greater than a Debye length. To see if this sort of geometry effect could cause the observed offset, the array strips themselves were used to measure the local floating potential by

Fig. 5.11: I±(dimensionless ion current) vs. dimensionless probe potential with respect to the space potential for cold ions, for various values of the ratio of the probe radius to the Debye length for a spherical probe tip. Shown also is the electron current (dashed line) to the probe vs. the same dimensionless potential. (Taken from Ref. 3)

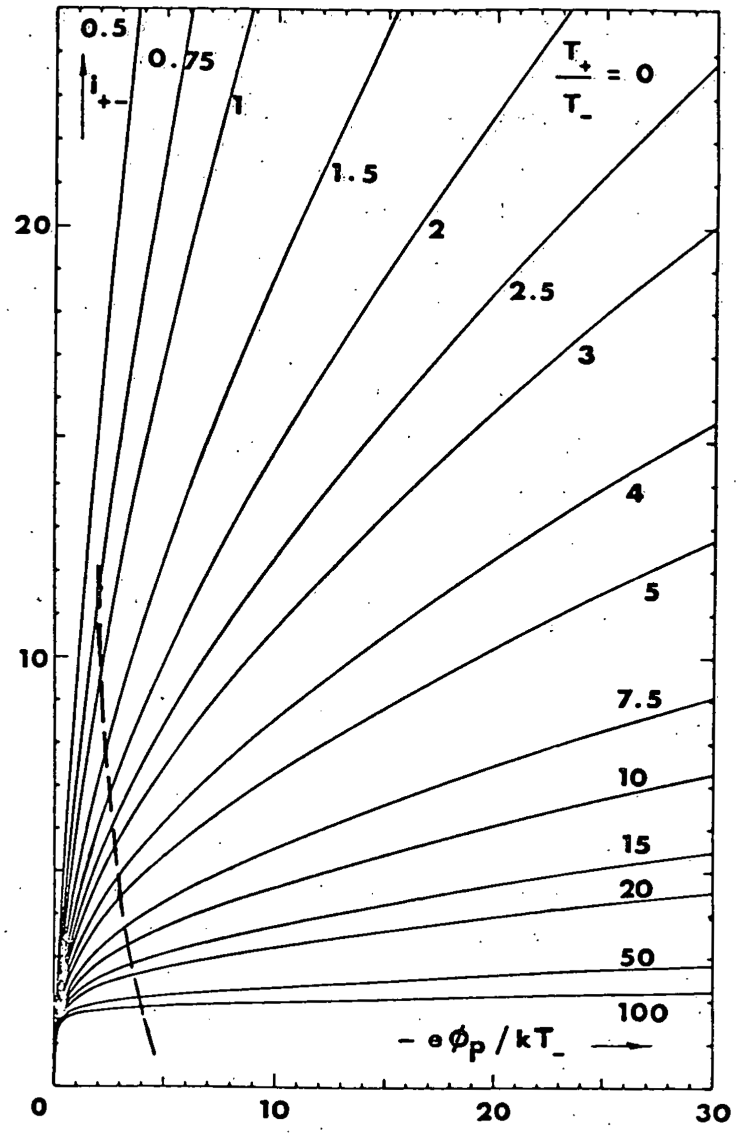

isolating each strip in turn electrically from the rest of the array, and measuring its potential. Because each strip is a plane collector the geometrical effect should be eliminated. In fact, exact agreement is observed between the potential and the current methods of measuring the outflow if the array strips are used. That is, the spatial extent of the nonambipolar flow that one would deduce from this measurement of η is the same as the current diagnostic. This is shown in Fig. 5.12, and comparison with Fig. 5.8 does indeed show agreement as to the spatial extent of the non-ambipolar flow. One can conclude that the observed offset is due entirely to the spherical geometry of our probe tip.

This result allows one to experimentally measure a value of alpha for a spherical probe tip. Rearranging equation 5.5 allows one to write the condition for ambipolar flow as

$$\phi_{fp} - \phi_{fs} = (\alpha' - \alpha)T_e \tag{5.7}$$

where the symbols have the same definition as before. In Fig. 5.5 the assumption $\alpha' = \alpha$ was made so the condition for ambipolarity was $\phi_{fp} - \phi_{fs} = 0$, or where the experimental curves crossed the x-axis. The correct condition for ambipolarity, that takes into account the geometrical effects discussed above, would plot the experimental $\phi_{fp} - \phi_{fs}$ versus $(\alpha' - \alpha)T_e$, and now the intersection of the two curves correctly indicates equal charge outflow. When this is actually done with the experimental data, the current measuring method

Fig. 5.12: $\Delta\Phi$ taken with the individual array strips vs. radius.

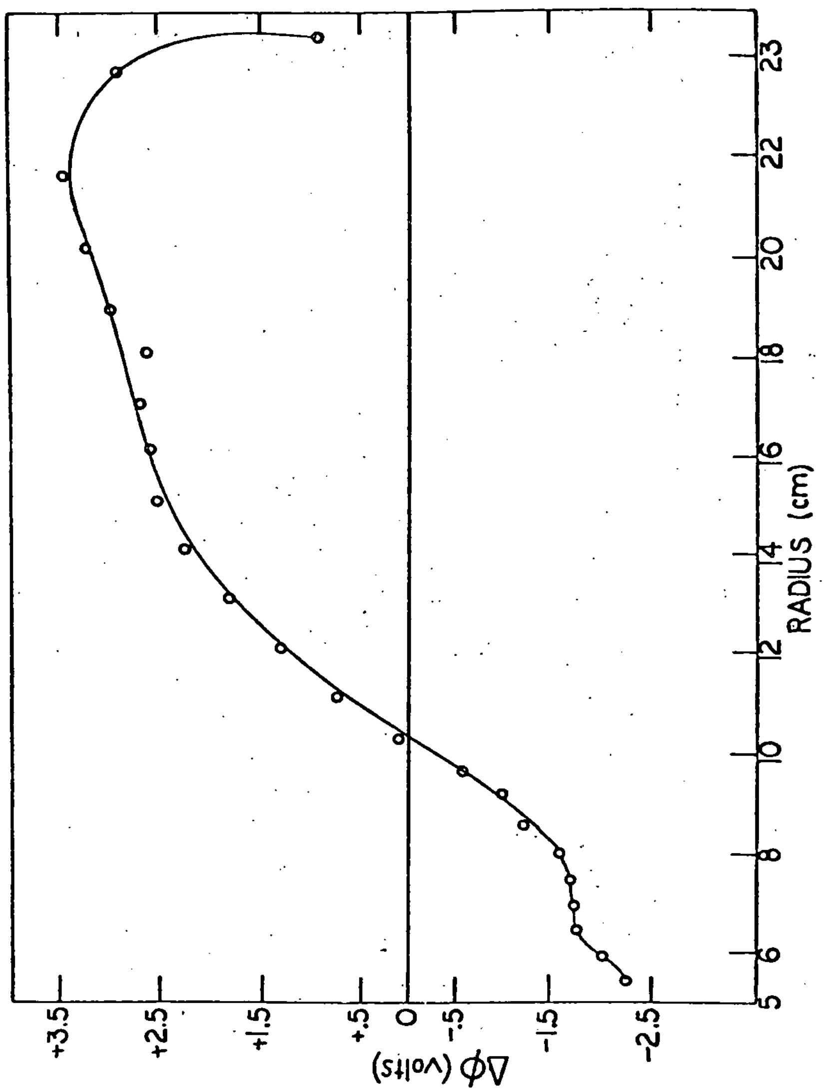

agrees well with the floating potential method, as shown in Fig. 5.13. However, the uncorrected curve provides a measure of alpha for the probe. Typically when the current diagnostic indicates a crossover to opposite charge outflow, the uncorrected floating potential diagnostic reads a positive .5 volts. Therefore the value of alpha for a probe for the case of a Helium plasma of electron temperature 3 eV at this point must satisfy

$$(\alpha' - \alpha)T_e = (4.22 - \alpha)3 = .5$$

or solving for alpha gives $\alpha = 4.05$, where the value 4.22 is the simple probe theory estimate for the value of alpha for a plane probe. This agrees well with the predictions of the theory of Laframboise. ($R_p / \lambda_d > 10$ for most of our plasmas.)

Theory of Non-ambipolar Diffusion

The theory of non-ambipolar diffusion was first presented in a paper by A. Simon[5] to describe some experimental findings in arc plasma experiments that were incorrectly attributed to instability driven diffusion.[6] The possibility and effects of non-ambipolar diffusion in a divertor were first discussed by A.H. Boozer, but from a different theoretical standpoint.[7] As an aid to one's intuition about this phenomena, presented here is a brief description of the underlying physics based on Ref. 5. A more formal derivation can be found in Ref. 8. In a plasma with no magnetic field, the electrons tend to diffuse out of a system faster than the ion species. A space

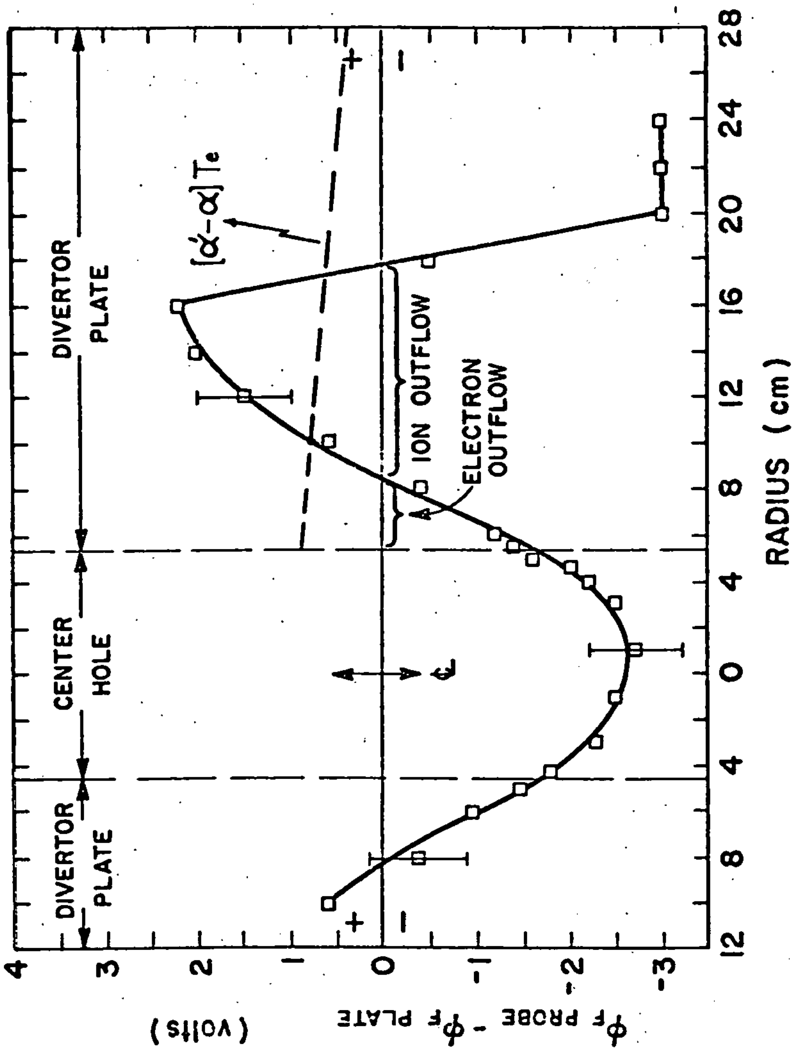

Fig. 5.13: Δϕ of Fig. 5.5 corrected for geometrical effects.

charge buildup occurs with a resulting electric field that reduces the electron current and maintains space charge neutrality. There results the familiar ambipolar diffusion coefficient, which is the same for both ions and electrons approximately given by

$$D = \frac{2D_+D_-}{(D_++D_-)}, \tag{5.8}$$

where D_+ and D_- are the ion and electron diffusion coefficients. Imposing a magnetic field has the effect of reducing the diffusion across $\underline{B}$ to the values

$$D_{\perp +} = \frac{D_+^{\,o}}{1+(\omega_+\tau_+)^2} \tag{5.10}$$

$$D_{\perp -} = \frac{D_-^{\,o}}{1+(\omega_-\tau_-)^2},$$

where the superscript zero indicates the field free value, and $\omega_\pm = e\underline{B}/M_\pm c$ and $\pm$ is the mean free time between collisions for ions and electrons. The diffusion coefficient along the field is the same as the $\underline{B}=0$ value. In our experiment $\omega_-\tau_- > \omega_+\tau_+ >> 1$ so the ordering

$$D_{\perp -} << D_{\perp +} << D_\pm^{\,o} = D_{\pm \parallel} \tag{5.10}$$

applies. One might think that, since the ions diffuse more rapidly across the field than the electrons, an ambipolar electric field would result that would speed up the electron diffusion so that the overall diffusion coefficient would be $D_\perp \simeq 2D_{\perp -}$. When the magnetic field intersects an end wall or a divertor plate, as in our case, this is no longer true. Because the parallel and perpendicular conductivities obey relations similar to equation 5.9 and inequalities similar to 5.10, (i.e. $\sigma_{\parallel e} >> \sigma_{\perp e}$ where σ is the conductivity), any inequality in the space charge can be removed by the flow of parallel currents to the divertor plate. Referring to Fig. 5.7, any electric field buildup can be counteracted by an enhanced electron flux to the plate at one location, and an enhanced ion flux at another location to preserve quasineutrality. The plate itself participates in the conduction by carrying electrons from the region of enhanced electron outflow to the area of enhanced ion outflow. Thus, this "short circuit" eliminates the need for an ambipolar electric field in the perpendicular direction. Furthermore, because there is no electric field to slow down the ion diffusion, the ions diffuse at their own characteristic rate.

The phenomenon of non-ambipolar transport may be of interest in tokamak divertors where a conducting target plate is placed across field lines as in this experiment. Whether or not it will occur in a tokamak divertor depends on whether $\nu_{in} > \nu_{ie}$, where ν_{in} is the ion neutral collision frequency and ν_{ie} is the ion electron collision frequency. For example, the collision frequencies can be shown to be[9]

$$\nu_{ie} = \frac{8(2\pi m_e)^{1/2} n \, \ln\Lambda \, e^4}{3 m_i T_e^{1/2} T_i} \tag{5.11}$$

$$\nu_{in} = n_n \sigma_{oi} (\frac{kT_i}{m_i})^{1/2} \tag{5.11'}$$

where n is the plasma density, n_n is the neutral density, $\ln\Lambda$ is the coulomb logarithm, m_e and m_i the electron and ion masses, T_e and T_i the electron and ion temperatures, and σ_{oi} the ion neutral collision cross section. For parameters typical of the PDX device: $T_i \simeq 50$ eV, $T_e \simeq 20$ eV, $\sigma_{oi} \simeq 5\times10^{-15} cm^2$, $\ln\Lambda = 16$, $m_i = 1.67\times10^{-24}$ g, $m_e = .91\times10^{-27}$ g, the scaling with neutral density and plasma density are

$$\nu_{ie} = n(2.28\times10^{-10}) \text{ sec}^{-1}$$

$$\nu_{in} = n_n(3.46\times10^{-8}) \text{ sec}^{-1}$$

Therefore, unless n_n/n is 6.6×10^{-3} or less, neutral driven transport will dominate in comparison to classical diffusion. Neutral pressure in the divertor chamber may be as high as 10^{-4} torr or higher. For plasma densities of 10^{12} cm^{-3}, neutral transport will dominate. If $\nu_{ie} > \nu_{in}$ charged particle transport will dominate the transport and the cross field flow may be automatically ambipolar due to conservation of momentum in charged particle collisions. (This may not hold up in plasma systems that have a finite length along $\underline{B}$.) It is interesting to note though, that the theory of Boozer[7] is for a fully ionized plasma and yet still predicts non-ambipolar diffusion. If, on the other hand, instabilities dominate the cross field transport, the flow may again be ambipolar because the time averaged $\underline{E}\times\underline{B}$ drifts will move ions and electrons across the field lines at the same rate, unless there is a localization of the driving instability that could cause resonance effects. For pressures below 10^{-3} Torr, Bohm diffusion will dominate classical ion-neutral collision driven transport. However, for pressures above this number, ion-neutral classical diffusion can again become comparable to Bohm.

If the flow is non-ambipolar, one can expect most of the electrons to exit the plasma where the separatrix intercepts the divertor plate. An electron "hot spot" will result as many more electrons will deposit their energy there. The ion energy flux will also be present, but its deposition profile will be unchanged from the ambipolar case. The energy flux to the collector plate from the electrons is given by

$$Q = n \exp(-e\,\phi_s/kT_e)(\frac{kT_e}{2\pi m_e})^{1/2}[e\,\phi_s + 2kT_e] \tag{5.12}$$

assuming a Maxwellian distribution of electrons, where again ϕ_s is the sheath potential drop, and n is the density at the sheath edge. Assuming that the density and temperature profiles remain the same in the ambipolar and non-ambipolar case, the ratio of the non-ambipolar to the ambipolar heat flux varies from 1.5 to 1.7 for our experimental parameters. That is, in the region of the electron "hot spot" the heat flux from the electrons is 50% to 70% greater than in the ambipolar case.

It might also be thought that the larger diffusion coefficient that occurs for non-ambipolar diffusion might change the shielding efficiency because the cross field particle flux will change. However, reference to equation (1.17) indicates the shielding to be only a function of τ_w and the plasma flux that crosses the separatrix. The actual profile may change, but the shielding properties don't depend on $D_\perp$.

The adverse effects of non-ambipolar flow make it desirable to be able to eliminate it. To this end each strip in the collector array was allowed to separately electrically float to eliminate the shorting path from electron to ion outflow region and hopefully force ambipolar cross field and parallel to the field flow. An insulating layer was placed on the back side of the divertor plate to prevent shorting there, where the same field lines that intersect the array also strike the collector plate.

Figure 5.14 shows the profile of η before and after the shorting path through the plate was removed, for a hydrogen plasma. (The data shown in Fig. 5.10 was for a helium plasma.) As is evident, the scale of the the outflow has been changed but the fact remains that the parallel flow is still non-ambipolar. The magnitude of the outflow imbalance has also been reduced. At radii smaller than 11 cm,

Fig. 5.14: η with the array strips shorted together and individually floating.

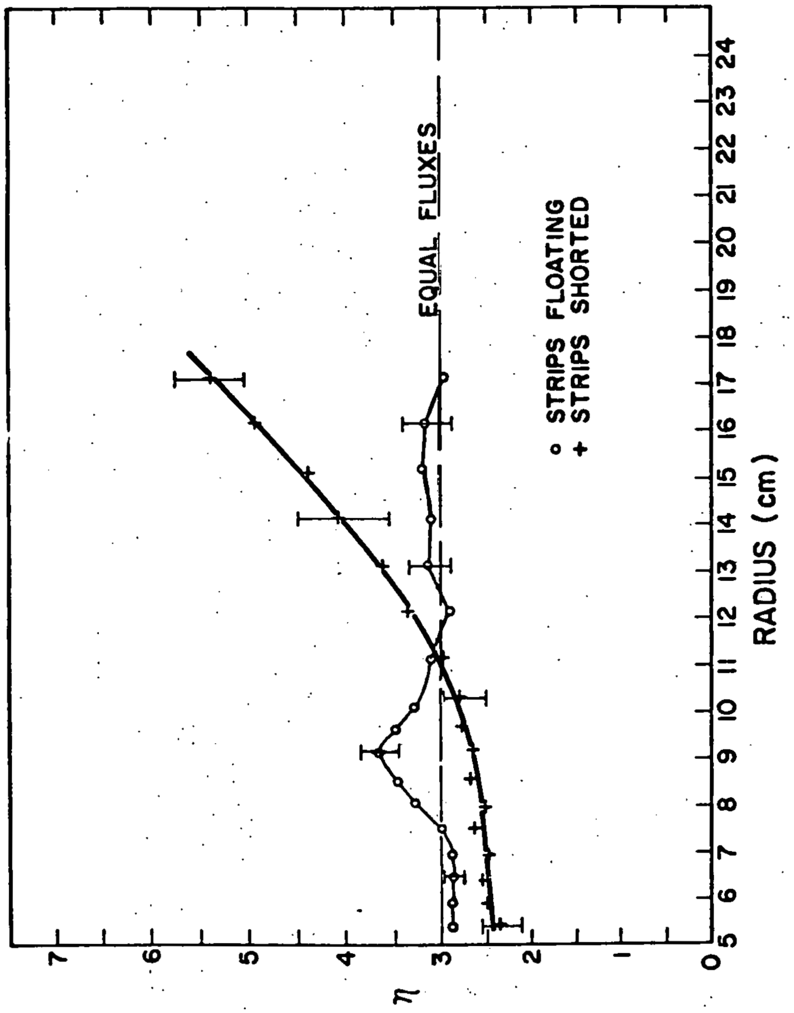

the outflow still shows the characteristic net electron outflow followed by net ion current. At radii larger than 11 cm, the flow is probably ambipolar. As to why the transport becomes ambipolar at large radii we can at present only speculate. The lower plasma density at these radii may not provide enough charge carriers to allow shorting on the surface of the array to occur. The mechanism that allows some shorting to occur in the regions of non-ambipolar flow is also unclear, and time limitations don't allow further investigation. Perhaps photoelectrons ejected from the ultraviolet light that is certainly present from the plasma, or charged particles that reside on the array for short periods before being neutralized, may allow shorting to occur across the face of the collector array. In any case, it appears that a greater effort is in order to eliminate the shorting that does occur, at least more heroic than simply allowing the array strips to float. R. Neidigh carried out the experimental verification of the diffusion coefficient scaling predicted by A. Simon[8], and apparently also found that non-ambipolar diffusion was hard to eliminate. Further indication that the individually floating array doesn't eliminate the shorting comes from the observation that the density profiles don't change substantially in the array shorted and floating cases, as shown in Fig. 5.15. This is evidence that the diffusion coefficient is virtually the same in both cases.

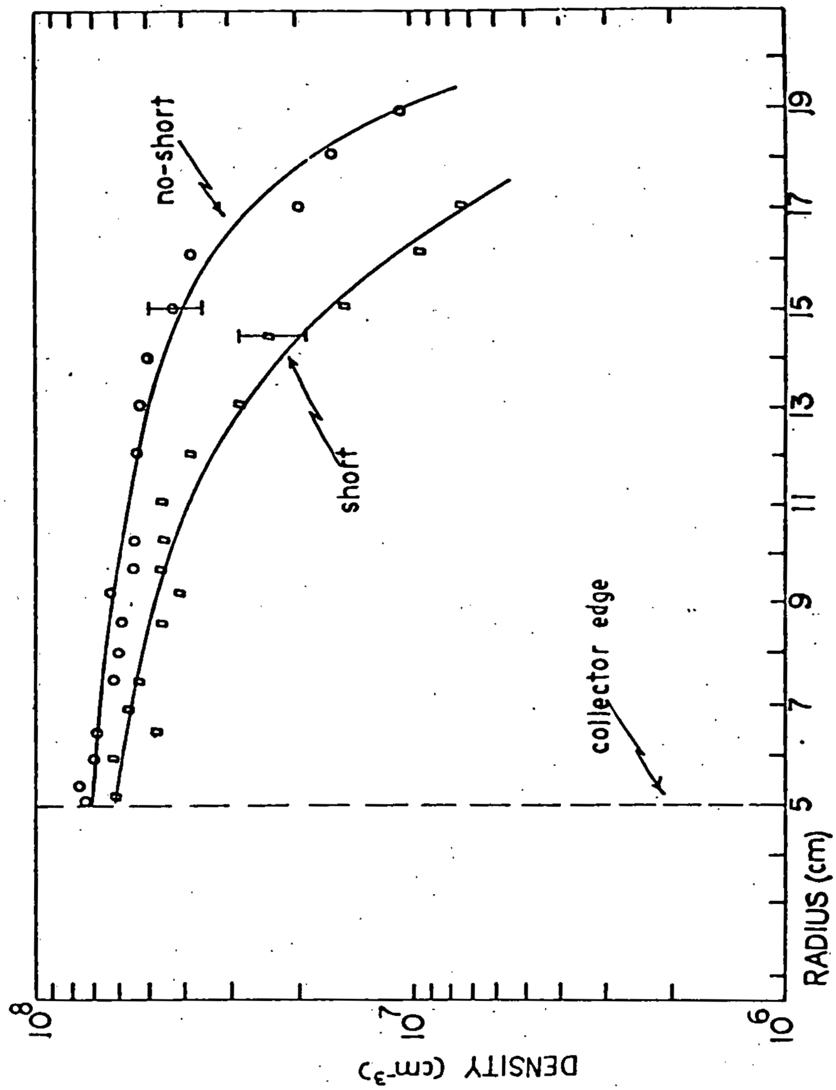

Fig. 5.15: Typical density profiles with the array strips shorted and unshorted. $D_\perp$ changes by less than a factor of 2.

Plasma Flow Velocity Measurements

Another quantity of interest in the understanding of divertor plasma physics is the net plasma flow velocity into the collector plate. Measurements of this quantity have been carried out in the past by propagating ion acoustic waves parallel and anti-parallel to the plasma flow. The difference in the transit time between the propagation in the two directions is proportional to the flow velocity.[10] Typical velocities measured are about one third the local ion acoustic velocity. A different diagnostic approach was adopted here in the interest of testing the results of previous experimenters by an independent means. The striped particle collector diagnostic measures the plasma flux $\Gamma_\parallel$ incident on its face, and so a simultaneous measurement of the density at the collector yields the flow velocity via the equation $V_\parallel = \Gamma_\parallel/n$. At the same time that the characterstic of the striped particle collector is obtained, a probe located in front of the collector measures the density. The measured flow velocities ranged from .3 to 4 times the local ion acoustic velocity with an average over thirty measurements of 1.6 times the ion acoustic velocity.

The reason for the large scatter in the data is not clear, but it is certain that it is not a real effect. For reasons mentioned previously in Chap. 3, all of the measurements were taken at nearly the same operating conditions by necessity. The measured flow velocities defied reproducibility at seemingly identical conditions of neutral pressure, microwave input power, field settings, as well as

measured electron temperatures and densities at the collector. In all cases I-V traces of the collectors appeared exactly as the theory said they should look, above a certain neutral pressure. Below this threshold of neutral pressure the traces became unsymmetric about the current axis. This could very well be a magnetic field effect and its disappearance above a certain neutral density caused by increasing collisionality that increases in turn the cross field diffusion. When the cross field transport is great enough, the parallel current to the collector behaves as it does in the field free case, and is no longer limited by the cross field transport. This is the same effect that complicates the use of probes in magnetic fields.[11] All of the data were obtained above this threshold, however, data was often taken on days widely separated in time. Data taken on the same day are closer to the same value of the flow velocity than data taken on different days. The last possibility that is unexplored is the effect of the long term deposition of impurities on the collectors, or the effect of long term bombardment with microwaves. These effects could change the properties of the insulator that the collectors were mounted on, and thus change the characteristic. For these reasons, the measured flow velocities have large error bars which are impossible to estimate. It appears that there is some truth here though, for the measured flow velocities are always near the ion acoustic velocity.

Comparison to the Theories of Boozer and Simon

It is of interest to compare the experimental scale lengths with the scale lengths predicted by Boozer[7] and Simon.[5] Both theories treat the case of uniform magnetic field, and predict an exponential spatial dependence of the density with a characteristic scale length. (The paper by Simon uses the same flow model that was described in the first chapter, however, based on his ideas about non-ambipolar diffusion, his choice for the cross field diffusion coefficient is $D_\perp=D_i/2$). As is clear by now, the density profiles in the experiment are not exponential,(evidenced by the non-linear semi-logarithmic plots) a reflection of the fact that the field increases in magnitude as a function or r, and thus $D_\perp$ decreases. Also, the volume per unit flux is changing and the temperature is changing. These also offset the profiles from an exponential dependence. However, a comparison can still be made by comparing a sort of "local" measured scale length with the theoretical local scale length. That is, for some small length dr along the radius, $D_\perp$ is approximately constant and equation 1.7 can be solved at this point to give a local density dependence as in equation 1.8. Within this dr, centered at r_o, the scale length is given by

$$\lambda = [(\frac{1}{n}\frac{dn}{dr})|_{r_o}]^{-1} \tag{5.13}$$

which is to be compared to the theoretical prediction at r_o.

The scale length of the electron outflow according to Boozer's theory is $\rho_e L/\lambda_e$. For parameters typical of this experiment: ρ_e=.5 cm, λ_e=300 cm, L=80 cm, this scale length is approximately .13 cm. Because this is considerably less than the electron gyroradius ρ_e, the fluid theory used by Boozer is clearly not applicable. (In fact, Boozer specifically assumes that $L/\lambda_e \gg 1$, and thus one would not expect the electron scale length to be valid in our experiment.) Therefore comparison of the electron outflow scaling to experiment is not valid. On the other hand, Boozer's scale length for the ion outflow is $\rho_i(T_e)$, the ion gyroradius evaluated at the electron temperature, which is obviously much greater than the actual ion gyroradius at all points. The scaling from Simon's paper for both species is $LD_i/2V_i$, where V_i is the ion acoustic velocity, L is the divertor length, and D_i is the ion diffusion coefficient due to ion neutral collisions. These two theoretical scale lengths were calculated and compared to the experimental scale lengths at the extremes of the D.C. machine's operating range. Table 5.3 shows this comparison for the high pressure limit with Helium gas ($P_n=10^{-3}$ Torr) and low pressure with Hydrogen gas ($P_n=5\times10^{-5}$ Torr), and are typical of the results found for all of the data taken. Shown in each case is the radius from the center line that the comparison is made at, and the ratio of the experimental scale length to the theoretical scale length at each point. Interestingly, the theoretical predictions seem to bracket the experimental values (except at one exceptional point that is not typical of the rest of the data) in all cases, the theory

Table 5.3

Comparison of Experimental Ion Outflow Scale-Lengths to Theoretical Scale Length

Helium- High Pressure

Radius (cm)	$\lambda_{exp.}/\lambda_{Boozer}$	$\lambda_{exp.}/\lambda_{Simon}$
7.0	.578	1.45
11.0	.537	2.60
13.0	.473	2.72
15.0	.473	2.39

Hydrogen- Low Pressure

Radius (cm)	$\lambda_{exp.}/\lambda_{Boozer}$	$\lambda_{exp.}/\lambda_{Simon}$
6.0	.337	.596
10.0	.605	1.45
12.0	.841	2.3
14.0	.780	1.73

of Boozer being typically a factor of two larger, and Simon's theory being less than a factor of three smaller. Considering the errors that enter the theoretical predictions from the measured parameters, for example errors in T_i, T_e, the ion neutral collision frequency, and the error inherent in sketching a curve through the experimental data points, the agreement is excellent.

References-Chapter 5

1. W.C. Guss, R.J. Fonck, University of Wisconsin Plasma Physics Report P.L.P. 584, (1974).

2. F.F. Chen, "Electric Probes" in Plasma Diagnostic Techniques, (R.H. Huddlestone and S.L. Leonard, eds.) Academic Press, New York (1965).

3. J.G. Laframboise, University of Toronto Institute of Aerospace Studies Report 100, (1966).

4. Edward P. Szuszczewicz, Julian C. Holmes , Journ. of Appl. Phys. 46, 5134 (1975).

5. A. Simon, Phys. Rev. 98, 317 (1955).

6. A. Guthrie, R.K. Wakerling, "The Characteristics of Electrical Discharges in Magnetic Fields", (McGraw-Hill Book Company Inc.,New York, 1949).

7. A.H. Boozer, Phys. Fluids 19, 1210 (1976).

8. A. Simon, Proceedings of the Second International Conference on Peaceful Uses of Atomic Energy, Geneva, Switzerland, Vol. 32, 343-348 (1958).

9. D.V. Sivuhkin, Reviews of Plasma Physics Vol. 4, (M. Leontovich, editor) 93, (1966).

10. K. Ando, et. al. , Princeton Plasma Physics Lab. Report Matt-1078, October 1974.

11. P.M. Chung, L. Talbot and K.J. Touryan, Electric Probes in Stationary and Flowing Plasmas: Theory and Applications, Springer-Verlag, New York (1975)

Chapter 6

Transport Codes

In an effort to further understand the transport in the scrape-off zone, it was decided to solve the one dimensional flow model that was described in Chapter 1, for our particular geometry. By varying the transport coefficients in the equation until a best fit to the experimental density and electron temperature profiles is obtained, one gains some knowledge of the magnitude and scaling of the transport coefficients within the limits of such a simple model. Additionally, one tests the feasibility of the flow model for divertors over the parameter range that our experiment covers.

Steady-State Diffusion Equation

As a first step, the steady-state particle diffusion equation was solved with the experimental electron temperature as an input parameter. The intention was to solve the more difficult time dependent problem of the coupled diffusion and energy transport equations as familiarity was gained with the numerical techniques from this simpler problem. It is also easier to change the transport coefficient scaling with just one equation, so the knowledge gained about the particle transport should eliminate the need to experiment with different scalings in the more complicated case.

To derive the relevant equation, consider the two adjacent flux surfaces shown in Fig. 6.1, which is the actual magnetic configuration used. Assuming Fick's law diffusion is valid over the whole flux

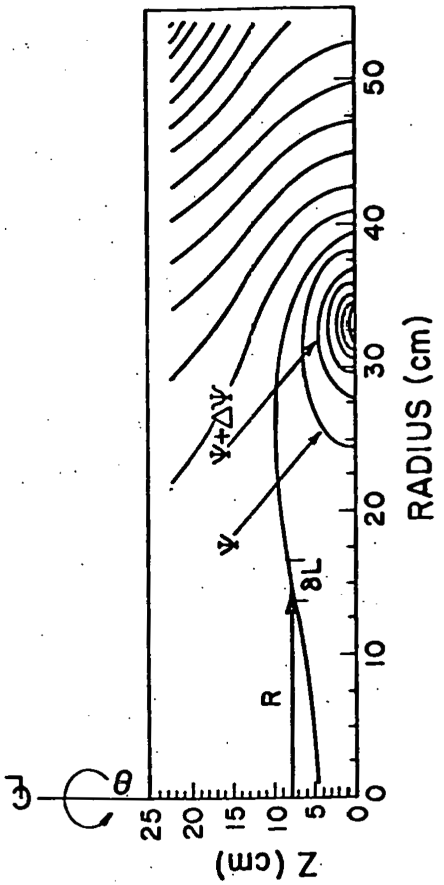

Fig. 6.1: The magnetic geometry of the experiment, showing the coordinate system used to derive the transport equation.

surface for the cross field particle flux ($\Gamma_\perp = -D_\perp \underline{\nabla} n$), the continuity equation for the volume between flux surfaces is written as follows:

$$\frac{\partial}{\partial t}(n\, dV) = \Delta\int_0^{2\pi} d\theta \oint d\ell\, (D_\perp \underline{\nabla} n)R \qquad (6.1)$$

where the Δ indicates the difference in the integrals evaluated on adjacent flux surfaces, dV is the volume between the ψ and $\psi + d\psi$ surfaces, θ is the azimuthal angle, R is the radius, and $\oint d\ell$ is the integral taken along a field line. Dividing both sides by $\Delta\psi$ and taking the limit as $\Delta\psi \to 0$, we get

$$\frac{\partial}{\partial t}\left(n \frac{dV}{d\psi}\right) = \frac{\partial}{\partial \psi}\left(\int_0^{2\pi} d\theta \oint d\ell\, (D_\perp \underline{\nabla} n)R\right). \qquad (6.2)$$

Now note:

$$\underline{\nabla} n(r) = \frac{\partial n}{\partial \psi} \underline{\nabla}\psi$$

$$\psi = \int_0^{2\pi} d\theta \int_0^R BR\, dR$$

$$\underline{\nabla}\psi = 2\pi\, RB$$

Therefore equation (6.2) can be written as

$$\frac{\partial n}{\partial t}\left(\frac{dV}{d\psi}\right) = (2\pi)^2 \frac{\partial}{\partial \psi}\left[\left(\oint d\ell\, R^2 D_\perp\right)\frac{\partial n}{\partial \psi}\right]. \qquad (6.3)$$

Despite the intention to model the steady state situation in our experiment, the time derivative term has been retained to phenomenologically model the loss term due to neutralization at the divertor plate. Consequently, we make the replacement:

$$\frac{\partial n}{\partial t} \rightarrow \frac{n}{\tau_\parallel} \qquad (6.4)$$

where, as in Chapter 1, $\tau_\parallel$ is the characteristic time for flow parallel to $\underline{B}$. This replacement can also be thought of more formally as arising from the parallel part of the divergence of the particle flux $\underline{\nabla} \cdot \underline{\Gamma} = \nabla_\perp \cdot \Gamma_\perp + \nabla_\parallel \cdot \Gamma_\parallel$. The right hand side of equation (6.3) is the perpendicular part of the divergence of the particle flux. The substitution $\nabla_\parallel \cdot \Gamma_\parallel \rightarrow \frac{nV_\parallel}{L} = \frac{n}{\tau_\parallel}$, can be thought of as being the result of averaging $\nabla_\parallel \cdot \Gamma_\parallel$ along a field line[1]

$$\nabla_\parallel \cdot \Gamma_\parallel \rightarrow \frac{1}{L(r)} \int_0^{L(r)} \nabla_\parallel \cdot \Gamma_\parallel d\ell = \frac{\Gamma_\parallel (L(r))}{L(r)}, \qquad (6.5)$$

because $\Gamma_\parallel = 0$ at $\ell = 0$ by symmetry (equal fluxes in both directions). In either case, making the substitution of equation (6.4) into (6.3) yields

$$- \frac{n}{\tau_\parallel} \left(\frac{dV}{d\psi}\right) + (2\pi)^2 \frac{\partial}{\partial\psi} \left[\frac{dn}{d\psi} J(\psi)\right] = 0, \qquad (6.6)$$

where $J(\psi) = \oint d\ell R^2 \underline{B} D_\perp$, and we have assumed that $\frac{dn}{d\psi}$ is independent of position along the field line. If one makes the assumption that $\tau_\parallel$ is proportional to $L/V_\parallel$, where $V_\parallel$ is the ion acoustic velocity, (appropriate to our case of $T_e >> T_i$) and L is the field line length, then

$$\tau_\parallel = \frac{L(\psi)}{(kT_e/m_i)^{1/2}}, \qquad (6.7)$$

where $L(\psi) = \frac{1}{2} \oint d\ell$. At this point let us take the functional form of $D_\perp$ to be: $D_\perp = C_o n^a(\psi) T_e{}^b(\psi) B^c(\psi)$. Different choices for the exponents a,b,c allow us to consider various scalings for $D_\perp$. Then equation (6.7) becomes

$$- \frac{n(kT_e/m_i)^{1/2}}{L(\psi)} \left(\frac{dV}{d\psi}\right) + C_1 \frac{\partial}{\partial\psi} \left[J_c(\psi) T_e{}^b(\psi) n^a(\psi) \frac{\partial n}{\partial\psi}\right] = 0, \qquad (6.8)$$

where C_1 is a collection of constants, and again we have assumed that the density and temperature are independent of position along the field line. In equation (6.8) note that $J_c(\psi) = \oint d\ell\ R^2 B^{c+1}$. The electron temperature is certainly a constant along a field line because of the long electron mean free path. It is anticipated that the density gradient along the field line will be much smaller than the gradient across the field, and this is in fact born out by the experiment. For a simple Boltzmann relationship between the density and the potential along the field line, where the potential drop is of the order of $T_e/2$ over the length of the whole field line, (i.e. the so called pre-sheath drop) the density at the sheath edge is 61% of the density at the center of the slab. Boozer[2] predicts an even smaller change, the density at the sheath edge being about 70% of the density at the center of the slab model divertor. On the other hand, the gradient across the field line is at least an order of magnitude in a distance about half as long as a field line. For this reason the density change along the field line will be neglected. Alternatively, one can think of the density on a given ψ surface as being an average density for that particular surface.

To allow for the case that flow into the collector plate may occur at some fraction of the ion acoustic speed, a multiplicative factor S can be inserted before the parallel loss term. Similarly, a multiplicative factor F can be included to allow for diffusion that scales like a given diffusion coefficient, but may be numerically different. The effects of these two factors is not separable however; they are lumped with C_o into the coefficient C_1. Only the ratio F/S affects the equation.

<u>Numerical Solution Technique</u>

Equation (6.8) is a linear partial differential equation in the flux space of the D.C. machine of the form

$$\frac{\partial}{\partial\phi}[f(\psi)\frac{dn}{d\psi}] - g(\psi)n(\psi) = 0, \tag{6.9}$$

here $f(\psi)$ and $g(\psi)$ are known functions of ψ. Our choice of a method of solution was a numerical one by necessity, involving finite differencing in space. The finite differencing scheme is one that is particularly appropriate for transport equations because of its desirable property of conserving particles. One constructs a spatial mesh in flux space, not necessarily uniform, as shown in Fig. 6.2. The boundaries between mesh zones are taken to be equidistant between adjacent mesh points. Equation 6.9 is integrated across a mesh zone

$$\int_{j-\frac{1}{2}}^{j+\frac{1}{2}} \frac{\partial}{\partial\psi}[f(\psi)\frac{dn}{d\psi}]d\psi - \int_{j-\frac{1}{2}}^{j+\frac{1}{2}} g(\psi)n(\psi)d\psi = 0, \tag{6.10}$$

and then each of the two integrals is approximated with finite difference schemes. For example, the first term becomes

$$f(\psi)\frac{dn}{d\psi}\Big|_{j-\frac{1}{2}}^{j+\frac{1}{2}} = f(j+1/2)[\frac{n_{j+1} - n_j}{\psi_{j+1} - \psi_j}] - f(j-1/2)[\frac{n_j - n_{j-1}}{\psi_j - \psi_{j-1}}], \tag{6.11}$$

where the subscripts j+m indicate that the density is evaluated at a mesh point if m is an integer, and at the midpoint between two mesh points if m is a half integer. The two functions f are further approximated by

$$f(j+1/2) = \frac{1}{2}[f(j+1) + f(j)] \tag{6.12}$$

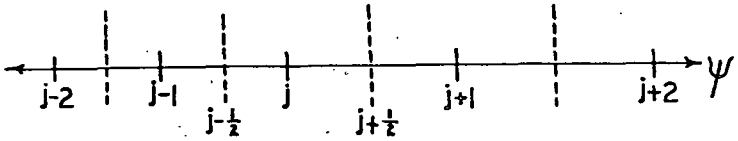

Fig. 6.2: The mesh spacing scheme used for the finite differencing of the transport equations.

$$f(j-1/2) = \frac{1}{2}[f(j) + f(j-1)].$$

The second term in equation 6.10 is approximated by

$$g(j)n_j \, \Delta_j, \tag{6.13}$$

where $\Delta_j = \frac{1}{2}(\psi_{j+1} - \psi_{j-1})$. All of these approximations break down if the chosen mesh spacing is too large, and thus care must be taken to assure that the mesh is fine enough. When all of these approximations are inserted into the original equation, one has a linear algebraic equation for n_{j+1} if n_j and n_{j-1} are known. The resulting equation is

$$n_{j+1} = n_j + (n_j - n_{j-1}) \frac{f(j-1/2)}{f(j+1/2)} \frac{(\psi_{j+1} - \psi_j)}{(\psi_j - \psi_{j-1})} + \tag{6.14}$$

$$\frac{g(j)}{f(j+1/2)} \, n_j \, \frac{(\psi_{j+1} - \psi_{j-1})}{2} (\psi_{j+1} - \psi_j).$$

Needed also, of course, are the various field line integrals for the chosen field configuration. These are obtained numerically using an existing program*. Therefore to solve for say n_4, the density at the fourth mesh point, one needs to know n_3 and n_2. Knowing n_4, one can in turn solve for n_5 also using n_3. This so called "shooting" method,

---

* Special thanks are due to Dr. L.P. Mai for his assistance in generating Ψ(R,Z) and the field line integrals.

so named because one shoots for the n_j point from the known n_{j-1} and n_{j-2}, is carried out until the entire profile is generated.

Two problems have been swept under the rug in the above treatment. The first is how one starts the algorithm. That is, to generate n_3 one needs to know n_2 and n_1. The value of n_1 can be chosen to be the experimental density at the left hand boundary which will also better facilitate the eventual comparison of the generated profile to the experimental profile. One could then conceivably pick n_2 arbitrarily and proceed to generate the rest of the profile until the right hand boundary value n_N is reached. However there is a better way, one that uses equation 6.9, the diffusion equation. Our object is to generate n_2, the density at the second mesh point. To this end, let us divide the space between the first two mesh points by adding another mesh point midway between these two and call it $j_{1/2}$. We further divide the space between j_1 and $j_{1/2}$ in two again, and call it $j_{1/4}$. Now again we integrate equation 6.9 from j_1 to $j_{1/2}$ and approximate the terms as before

$$\left[f(\psi)\frac{dn}{d\psi}\right]\Bigg|_{j_1}^{j_{1/2}} - g(j_{1/4})n_{1/4}\left(\frac{\psi_2 - \psi_1}{2}\right).$$

Now, we approximate the second term by a Taylor series

$$g(j_{1/4})n_{1/4} = g(j_{1/4})\left[n_1 + n_1'\left(\frac{\psi_2 - \psi_1}{4}\right)\right], \tag{6.15}$$

and the first term

$$f(j_{1/2})\frac{dn}{d\psi}\Big|_{j_{1/2}} - f(j_1)\frac{dn}{d\psi}\Big|_{j_1} =$$

$$f(j_{1/2})\left(\frac{n_2 - n_1}{\psi_2 - \psi_1}\right) - f(j_1)n_1', \tag{6.16}$$

where n_1' is the derivative of the density at the first mesh point. Combining these results yields

$$n_2 = n_1 + \frac{\psi_2 - \psi_1}{f(j_{1/2})}\left[f(j_1)n_1' + \left(\frac{\psi_2 - \psi_1}{2}\right) g(j_{1/4})\left\{n_1 + n_1'\left(\frac{\psi_2 - \psi_1}{4}\right)\right\}\right] \tag{6.17}$$

Therefore knowing n_1 and n_1' the algorithm can be self-consistently started. It appears at this point that we have merely traded uncertainty in the choice of n_2 for uncertainty in the choice of n_1', but this too can be self-consistently remedied. As with the left hand boundary, one desires the numerical results to agree with the experimental results at the right hand boundary. One procedure would be to iteratively adjust the value of n_1' until the value of the density generated at the right boundary, n_N, agrees with the experimental one. However, because of the linearity of equation 6.9 an easier approach is available. The density at the right hand boundary, n_N, is linearly dependent on the gradient at the left hand boundary, n_1'.

$$n_N = an_1' + b, \tag{6.18}$$

or equivalently,

$$n(\psi_N) = an'(\psi_1) + b,$$

where the constants a and b are to be determined. Some initial choice for $n'(\psi_1)$, call it $n_1'(\psi_1)$, will yield a unique $n_1(\psi_N)$. A second choice for $n'(\psi_1)$, say $n'_2(\psi_1)$, will yield a second $n_2(\psi_N)$. Writing out these two equations

$$n_1(\psi_N) = an_1'(\psi_1) + b$$

$$n_2(\psi_N) = an'_2(\psi_1) + b, \tag{6.19}$$

and by the solution of these simultaneous equations, the constants a and b are uniquely determined. Thus by inverting equation 6.18 the correct $n'(\psi_1)$ to yield the experimental right hand boundary value is determined on the third pass through the algorithm.

The imposition of the experimental boundary values on the numerical solution at first seems like an arbitrary step to force a measure of agreement between theory and experiment that is hard to justify. The alternative would be to write a diffusion equation for the plasma on field lines outside the separatrix as well as inside, as

has been done, and insist on the continuity of the density and its derivatives at the separatrix. This last condition would replace the boundary conditions that we imposed. However, a degree of arbitrariness would exist again, in that the plasma source strength of the experiment would have to be imposed on the code. This seems like an obvious necessity, unless one intends to model the source as well, that defines a starting baseline for the code. Beyond the imposition of this baseline, the numerical solution must be allowed to evolve independently of the experiment if a true comparison between theory and experiment is to be obtained. After defining the density and its slope at the first mesh point, the numerical solution evolves according to equation 6.9. The critical point of comparison to the experiment is the shape the numerical solution assumes between the boundary values. Only when the numerical solution shape and the experimental shape agree in this region can one argue for a theory that describes the physical processes in the experiment accurately. Inherent in this is the understanding that the multiplicative factors F and S will not be far from unity when agreement is obtained, or serious questions as to the applicability of a given transport coefficient scaling should be raised.

The indicated equations were incorporated into a program written in Rebel Basic[3] and run on a DEC PDP-11 computer. To assure that the numerical approximations accurately model the differential equation, profiles generated on a given mesh were compared to profiles generated on a mesh of half the mesh spacing and found to agree almost exactly.

Therefore we felt assured that the approximations were sufficiently accurate.

Bohm diffusion was chosen as a first case since this assumption has been used in some of the phenomenological divertor studies[1]. Bohm diffusion scaling is $a=0$, $b=1$, $c=-1$. The best fit solution for this case is obtained with $(F/S)=.03$ and is shown in Fig. 6.3 along with the experimental profile. Since the flow velocity parallel to $\underline{B}$ has been measured to be near the ion acoustic velocity, the implication is that the cross field transport is much smaller than Bohm diffusion.

Since we have a rather high neutral density, the case of transport due to ion-neutral collisions is of interest. For neutral collision dominated transport in a magnetic field one has $a=0$, $b=0$, $c=-2$. The best fit profile is shown in Fig. 6.4, and occurs for $F/S\simeq 1$. A comparison of the two cases treated thus far shows that the classical diffusion coefficient scaling gives better agreement with the measured profile than the Bohm diffusion case; this is in agreement with similar measurements done earlier on the D.C. machine[4]. A value of $T_i\simeq .1$ eV is assumed independent of radius in these solutions.

These profile comparisons have been carried out over the full range of the operating conditions of the D.C. machine, and in each case the results are similar. The numerical results agree with the experimental data for small fractions of the Bohm diffusion coefficient, and for values near the classical diffusion coefficient. Admittedly the agreement given by the choice of classical scaling

Fig. 6.3: The numerical solution to the steady-state diffusion equation compared to the experimental density profiles for Bohm scaling in $D_\perp$, and $F/S=.03$.

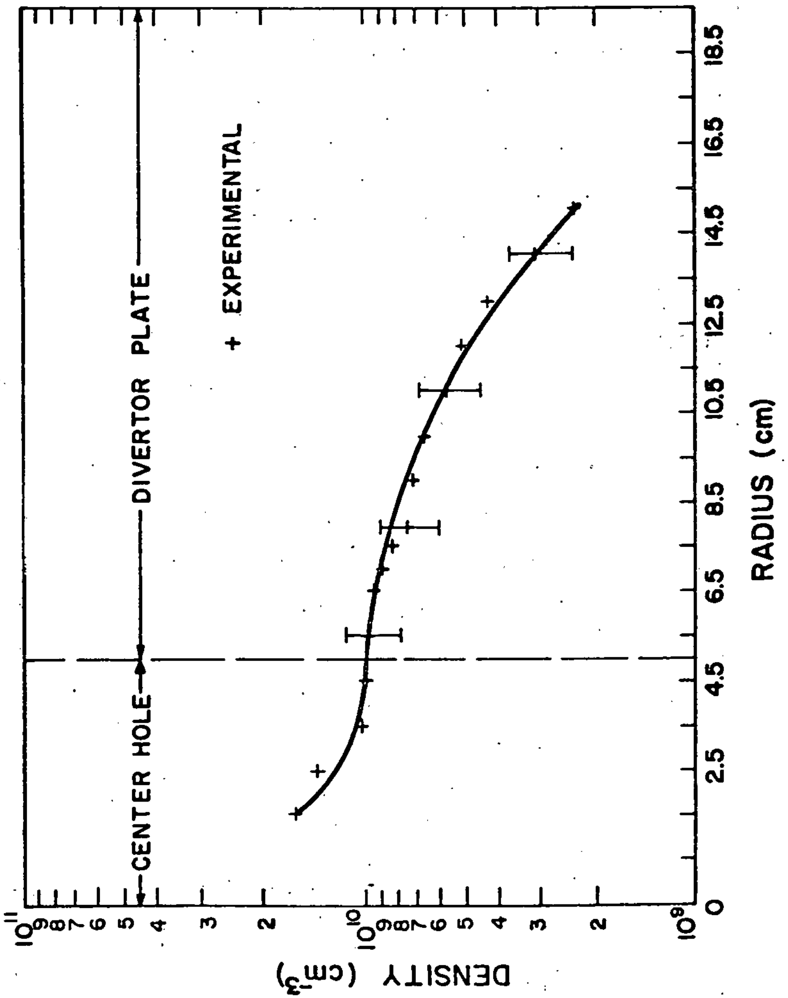

Fig. 6.4: The numerical solution to the steady-state diffusion equation compared to the experimental density profiles for classical ion-neutral scaling in $D_\perp$, and $F/S \approx 1$.

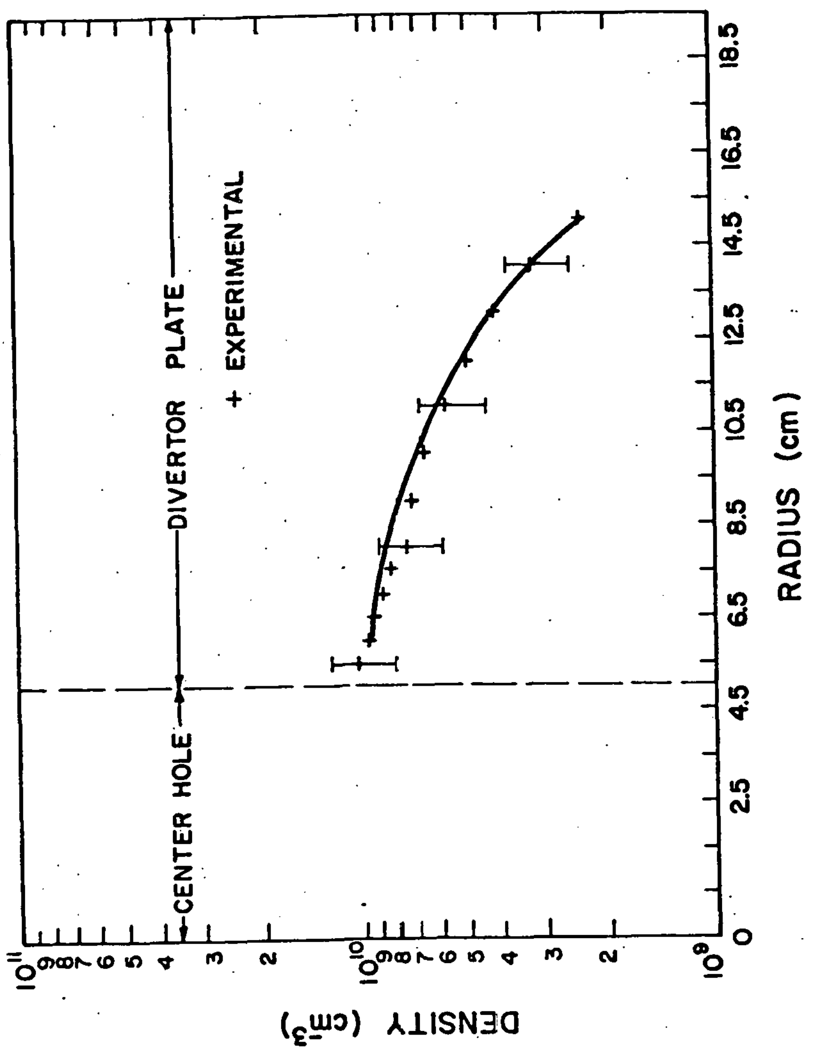

gives only marginally better agreement than Bohm scaling within the uncertainty of our density profiles. Although classical scaling is $\propto B^{-2}$ and Bohm is $\propto T_e B^{-1}$, the experimental T_e profile is roughly $\propto B^{-1}$; this probably explains why we can't more clearly resolve which scaling is present. However, the observed absence of fluctuations in the experiment and the high neutral density indicate that the choice of classical scaling is probably the better one.

Time Dependent Transport Equations

In light of the success of the simple steady-state equation solution, it was decided to attempt the more complex problem of a solution to the coupled energy and particle transport equations. The hope was again to learn more about the type of transport in the scrape-off zone and test the applicability of the one dimensional flow model to the energy transport as well as the particle transport. In addition, because of the non-linear nature of the transport equations, the time dependent equations were chosen as a starting point. The procedure will be to allow the time dependent solution to evolve to steady state. Comparison is then made between the computed steady state profiles and the experimental results. The experience of Mense[5] in such cases indicates that this often the best way to obtain the solution to nonlinear differential equations, and avoid numerical stability problems.

The particle transport equation is, for the most part, the same as equation 6.8, except that the time dependent term in the continuity equation is retained

$$\frac{\partial n}{\partial t}\left(\frac{dV}{d\psi}\right) - (2\pi)^2\frac{\partial}{\partial\psi}\left[\left(\oint d\ell\ R^2 D_\perp B\right)\frac{\partial n}{\partial\psi}\right] = \tag{6.20}$$

$$- \frac{dV}{d\psi}\left[\frac{n(kT_e/m_i)^{1/2}}{L(\psi)}\right].$$

The electron energy transport equation can be derived in a manner similar to the derivation of the particle transport equation, by performing an energy balance on a tube of flux

$$\frac{\partial}{\partial t}\left(\frac{3}{2}nkT_e\right)dV + k\ \Delta\int_0^{2\pi} d\theta\ \oint d\ell\ \left[-\ K\ \underline{\nabla}T_e + \frac{3}{2}\ \underline{\Gamma}T_e\right]R = -\ (S_e\ dV), \tag{6.21}$$

where the Δ again indicates that the line integral is to be carried out on the ψ and $\psi+d\psi$ surfaces, and subtracted, and k is Boltzmann's constant. The term S_e includes energy sources and sinks. The $K\underline{\nabla}T_e$ term accounts for thermal conduction , where K is the thermal conductivity, and the term $\frac{3}{2}\underline{\Gamma}T_e$ accounts for convective energy transport. We will assume in all that follows that $K=\frac{3}{2}Dn$ and $\underline{\Gamma}= -D\ \underline{\nabla}n$, where the first is the classical thermal conductivity for a dilute gas[6] and the second is an assumption of Fick's law transport. We will assume classical scaling for the diffusion coefficient based on the solution of the steady state equation that agrees most closely. The dominant electron cooling mechanism (to be proved shortly) is parallel flow through the sheath to the divertor plate. For a Maxwellian distribution of electrons, this loss is

$$Q_\parallel = 2\pi n \int_{-\infty}^{\infty} V_\perp dV_\perp \int_{V_{min}}^{\infty} dV_\parallel\left(\frac{1}{2}mV_\parallel^{\ 2}\right)V_\parallel\ f(V) =$$

$$\left(\frac{kT_e}{2\pi\, m_e}\right)^{1/2}[e\phi_s + 2kT_e]n\ \exp(-e\phi_s/kT_e), \tag{6.22}$$

here V_{min} is the lowest electron velocity that can traverse the sheath and reach the collector plate, and ϕ_s is the sheath potential drop. In the event that the parallel particle flow is ambipolar, one can write the loss as

$$Q_\parallel = (kT_e/m_i)^{1/2}[e\phi_s + 2kT_e]n. \tag{6.23}$$

Within the context of the flow model, the parallel loss term is $Q_\parallel/L$, with the same L as in the particle equation. When the differentiation of the first term in equation 6.21 is carried out and equation 6.20 substituted in for the $\frac{\partial n}{\partial t}$ term, the energy equation becomes

$$\frac{3k}{2}\left(\frac{dV}{d\psi}\right)\frac{\partial T_e}{\partial t} + \frac{3}{2}\ k(2\pi)^2\ \frac{T_e}{n}\left[\frac{\partial}{\partial\psi}\left\{J(\psi)\frac{\partial n}{\partial\psi}\right\}\right] \tag{6.24}$$

$$-\ \frac{3k}{2n}(2\pi)^2\left[\frac{\partial}{\partial\psi}\left\{J(\psi)\left(n\frac{\partial T_e}{\partial\psi} + T_e\frac{\partial n}{\partial\psi}\ \right)\right\}\right] =$$

$$-\ \frac{dV}{d\psi}\ \left[\frac{(kT_e/m_i)^{1/2}}{L(\psi)}\right]\left(\frac{1}{2}\ kT_e + e\phi_s\right)$$

where we have used the same definition of $J(\psi)$, namely

$J(\psi) = \oint d\ell R^2 \underline{B} D_\perp$. Equations 6.20 and 6.24 are the equations to be solved simultaneously. One notes that the energy loss terms contain the sheath potential drop. In the absence of a third equation that determines ϕ_s, the value of the experimental sheath drop will be inserted.

Up to this point, flow to the divertor plate has been assumed to be the dominant particle and energy loss mechanism. That this is indeed so can be seen by comparing it to other potential source or loss terms for some typical experimental parameters. The particle and energy loss rate for particle flow to the divertor plate is

$$n_{loss} = \left(\frac{nV_\parallel}{L}\right) \tag{6.25}$$

$$E_{loss} = \left(\frac{nV_\parallel}{L}\right)E_{av}$$

where n and $V_\parallel$ are typical plasma densities and loss velocities, L is the length to the plate, and E_{av} the average energy loss per particle. For a conservative estimate of this term, let us choose $V_\parallel$ to be the ion acoustic velocity, and E_{av} from equation 6.22, so 6.25 becomes

$$E_{loss} = \frac{n}{L}\left(\frac{kT_e}{m_i}\right)^{1/2}(e\phi_s + \alpha T_e). \tag{6.26}$$

Choosing some typical parameters: T_e=10 eV, m_i=4x1.67x10^{-24} g, n=1x10^{9} cm^{-3}, L=43 cm, $e\phi = \alpha T_e$ for ambipolar flow, one finds

$$n_{loss} = 3\text{x}10^{13} \text{ particles/sec.}$$

$$E_{loss} = 2\text{x}10^{15} \text{ eV/sec.} \tag{6.27}$$

In the diffusion equation, cross field diffusion is the only source term that balances the particle loss. Other source terms that are possible are ion production due to electron impact ionization, and ion loss due to charge exchange. Of thse two processes, electron ionization is by far the larger for our cold ions ($T_i \simeq .1$ eV), so we will consider this one only. The Maxwellian averaged reaction rate for 10 eV electrons on helium gas is $\langle \sigma v \rangle \simeq 1\text{x}10^{-19}$ cm^3/sec.[7] Therefore the production rate of ions due to ionization is

$$n_p n_n \langle \sigma v \rangle_{ioniz} = 3\text{x}10^{12} \text{ particles/sec,} \tag{6.28}$$

for plasma and neutral densities respectively of n_p=1x10^{9}, and n_n=3x10^{12}. This source term is at least as order of magnitude less than the loss due to neutralization at the plate, and is thus negligible.

In the energy equation we have ignored the energy loss processes of inelastic collisions of electrons with neutrals and ions. The dominant of the these two is loss due to electron-neutral collisions, which includes ionization loss. Based on the treatment by Patau[8], this total loss rate rate is

$$n_p n_n R\langle \sigma v\rangle_{ioniz} = 2.22\text{x}10^{14}\ \text{eV/sec} \qquad (6.29)$$

where R is the total energy loss per ionization. Again this loss term is small compared to the assumed loss term by about an order of magnitude, and is therefore justifiably not included.

Numerical Solution Technique

The numerical solution technique that we follow closely parallels the treatment outlined in Ref. 9. The spatial finite differencing is accomplished by the same method that is outlined for the steady state solution earlier in this chapter. The differencing is carried out in a way that will allow arbitrary spatial meshes to be imposed later. As with the particle equation, this method of implementing the finite differencing also preserves the heat fluxes as well as the particle fluxes, since the flux leaving one spatial mesh is the same flux that enters the next. Upon the completion of the finite differencing, the equations appear in the following functional form

$$\frac{dV}{d\psi}\Big|_k \left(\frac{\psi_{k+1} - \psi_{k-1}}{2}\right)\frac{\partial n_k}{\partial t} = f(n,T_e) \qquad (6.30)$$

$$\frac{3}{2}\frac{dV}{d\psi}\Big|_k \left(\frac{\psi_{k+1} - \psi_{k-1}}{2}\right)\frac{\partial T_{e_k}}{\partial t} = g(n,T_e)$$

where f and g are complicated expressions involving the density and temperature at neighboring mesh points as well as the kth mesh point, and of course the field line integrals and constants. Equations 6.30 are valid at each mesh point. It is our desire to perform some sort of temporal finite differencing scheme that will enable us to step ahead in time from the known values at a previous time, thus allowing the profiles of density and temperature to evolve. If we make the replacement

$$\frac{\partial n_k}{\partial t} \rightarrow \frac{n_k^{p+1} - n_k^p}{\Delta t}, \qquad (6.31)$$

$$\frac{\partial T_k}{\partial t} \rightarrow \frac{T_k^{p+1} - T_k^p}{\Delta t},$$

where the superscript indicates a time step, and the unnecessary subscript 'e' has been dropped on the electron temperature to avoid confusion. Now note that knowing n and T at the pth time step, and the value of f and g, we can calculate n and T at the p+1 time step. Such an algorithm is started from known boundary and initial conditions. One possible solution technique would be to evaluate f and g using n and T at the p time step. This method is called the explicit or Euler technique[10] which, while having the virtue of simplicity over other techniques, is plagued by stability problems if the time step is too large. A solution technique with no stability problems and other advantages[11] is the so called implicit method, where f and g are evaluated at the p+1 time step, and is the method we chose. Whether or not the finite difference approximation correctly models the differential equation for a given time step is a separate problem that must be investigated. With the choice of the implicit method our equations look like

$$\frac{dV}{d\psi}\Big|_k \left(\frac{\psi_{k+1}-\psi_{k-1}}{2}\right)\frac{n_k^{p+1}-n_k^{p}}{\Delta t} = f(n^{p+1},T^{p+1}) \qquad (6.32)$$

$$\frac{3}{2}\,\frac{dV}{d\psi}\Big|_k \left(\frac{\psi_{k+1}-\psi_{k-1}}{2}\right)\frac{T_k^{p+1}-T_k^{p}}{\Delta t} = g(n^{p+1},T^{p+1}).$$

To simplify the solution, we further expand each element of f and g in a Taylor series in time, keeping only terms linear in Δt which leads to a linearized set of equations in density and temperature at the new time, p+1. For example the expansion of f would look like

$$f(n_k^{p+1},T_k^{p+1}) = f(n_k^p,T_k^p) + \left[\frac{\partial f^p}{\partial n_k}(n_k^{p+1}-n_k^p) + \frac{\partial f^p}{\partial T_k}(T_k^{p+1}-T_k^p)\right] + \ldots.. \qquad (6.33)$$

As a further simplification, terms involving the transport coefficients are evaluated at the p time step, a procedure that has been shown to yield the same steady state solution as evaluating at p+1 and linearizing; however the intermediate profiles do not represent a correct time evolution. This process of linearizing generally turns each term in f and g into as many as five terms which makes the ensuing algebra tedious.

Because the equations are linearized in time, a simplified analysis of the numerical treatment can be carried out. At each time step the equations can be put into the form

$$A\underline{x}^{p+1} = B\underline{x}^{p}, \qquad (6.34)$$

where A and B are matrices and $\underline{x}$ is a linear array whose transpose has the form

$$\underline{x}^p = (n_1^p,T_1^p,n_2^p,T_2^p,n_3^p,T_3^p,\ldots n_N^p,T_N^p)$$

and because of the choice of time differencing, the matrix A is block tri-diagonal which permits a certain economy is the solution scheme. Equation 6.34 is solved for $\underline{x}^{p+1}$ at each time step, and the resulting matrix $\underline{x}^{p+1}$ is in turn multiplied by the matrix B, and the process repeated to solve for the array $\underline{x}^{p+2}$. The whole profile of n and T are generated at each time step in this solution method,[11] and one steps in time until the profiles at suceeding time steps are identical, at which time the steady state solution has been reached. The matrix A was inverted using a Gaussian elimination routine specialized to tri-diagonal matrices.

As with the steady state program, the experimental boundary conditions are imposed at the left and right boundaries at each time step. Because the algorithm actually calculates the parameters at the mesh points and the physical boundary is located between the mesh points 1,2 and N-1,N, we must resort to the simple device of imposing an average endpoint density that incorporates the boundary condition. Thus for the first mesh point

$$\frac{n_1^p + n_2^p}{2} = n_L, \tag{6.35}$$

where n_L is the experimental boundary condition at the left boundary. One solves 6.35 for n_1^p, the density at the first mesh point

$$n_1^p = 2n_L - n_2^p, \tag{6.36}$$

which is imposed on the algorithm at each time step. Relations like 6.36 are assumed for both the density and temperature equations at each time step at the left and right boundary. The initial profile assumed is simply a straight line between the two boundary values.

This algorithm was carried out in a program written in Fortran on the P.S.L. Vax computer. Experimentally it is found that the method is indeed stable for any time step, but requires steps of 10^{-5} sec. or less to properly model equations 6.20 and 6.24. This was determined by decreasing the time step Δt until the steady state solution reached was the same for any time step less than this Δt. Typically steady state is reached in 10^{-3} sec. which takes about two minutes of CPU time. This program was written with the option of using a variable spatial mesh to more accurately handle regions of large gradients of density or temperature. The Tektronix Plot-10 plotting package was found to be most useful to allow the generated profiles to be viewed immediately and avoid the delays of hand plotting, when comparing profiles to assess the effects of different scaling assumptions.

Time Dependent Code Results

Constant multiplying factors are again inserted in the program before all of the transport coefficients and the various loss terms so that the magnitude but not the scaling of the terms can be varied. A factor FC multiplies the conduction term, FD the cross field particle diffusion terms, FS the parallel loss term for both the density equation and the temperature equation when the loss term of equation 6.23 is used. In both the density and temperature equations, the characteristic velocity in the loss term is the ion acoustic velocity and separate multipliers aren't required. In the case that the loss term of equation 6.22 is used, a factor FSI multiplies the parallel loss term in the density equation, and FSE the parallel loss term in the temperature equation. Here, unlike the previous case, the parallel velocity is not the same in both equations and a separate multiplier is appropriate. The actual values of the transport coefficients used in the program, are calculated with the local self-consistent values of density and electron temperature. When any of the multipliers are one, the transport coefficient is one times the theoretical value. For example, for assumed classical neutral dominated transport, FD=1 means $D_i = kT_i \nu / m \omega_c^2$, where T_i is assumed uniform at .1 eV, ν is the collision frequency of ions on neutrals and the neutral density is the the same as the experimental neutral density, and ω_c is the ion cyclotron frequency with the local magnetic field value of the experiment. FS=1 means the parallel loss velocity is the local ion acoustic velocity $(kT_e/m_i)^{1/2}$. Bohm transport scaling does not seem to occur in our experiment based on the results of the steady state program, and as a result was not tried in the time dependent case. Recall too that only the ratios of the constant multipliers is relevant, and so only the ratios will be displayed when the results are given, normalized to FC. The values given in each case are the values for which the program most closely agrees with the experimental data, which is also shown for comparison.

One last topic is in order before the discussion of the numerical solutions, that relates to the choice of the transport coefficients in the energy equation. In the particle diffusion equation both the steady state numerical results and the theory of Simon support the choice of ion-neutral collision dominated scaling for D_i. If one takes the theory of Simon literally and assumes that the ambipolar electric field is completely "shorted out" by the divertor plate, then because there is therefore no coupling between ions and electrons, the cross field conductivity and convection should have the classical

electron-neutral collision dominated values. This scaling will certainly be tried in the energy equation. However, if the divertor plate doesn't completely eliminate the ambipolar electric field, coupling between ions and electrons through this field will exist to some extent, and the appropriate diffusion coefficient scaling in the convective term may be the ion classical value or some fraction thereof. Intuitively this seems to be the most likely case. Because of the finite sheath potential drop (or parallel conductivity), there has to be some radial ambipolar electric field that isn't shorted out. There is also, however, an electric field due to the temperature gradient. The divertor plate is an equipotential, so unless the sheath drop is a constant (which it is manifestly not experimentally) then the there will also be a field due to the temperature gradient. Thus the field due only to the differing diffusion coefficients will be hard to sort out. (In fact, from the experimental measurements of the electric field, we infer that the contribution due to the temperature gradient and finite sheath potential drop dominates in determining the electric field.) For completeness, ion classical scaling will also be tried in the conductivity term in the energy equation, although it is not theoretically supportable within the context of our model.

Coefficients appropriate to ion-neutral collision dominated classical transport (henceforth called ion classical transport) in both the density and temperature equations, and the loss term of equation 6.23 (to be referred to as the ambipolar loss term) in the temperature equation were tried first. The loss velocity in the density equation in this entire section is the ion acoustic velocity. The best fit results are shown for a high pressure helium case (P_10^{-3} torr) and for a low pressure hydrogen case (P_5x10^{-5} torr) in Figs. 6.5 and 6.6. In both cases good agreement is obtained for values of the multipliers of less than 5. The data to which the numerical results are compared is the unshorted array case. As was seen in Chap. 5, in no case do we have data that one could say is truly ambipolar, but this data is nearer to ambipolar than the shorted array case.

Figure 6.7 shows the case of the program with the same coefficients as the last case, compared to the shorted array case. Again good agreement is obtained with multipliers of less than 5. It is interesting that using the "ambipolar" program (i.e. that is with loss terms that should be appropriate to truly ambipolar flow) one can still obtain agreement with the shorted array case.

Figure 6.8 displays the case where only the loss term in the temperature equation is changed to the loss term of equation 6.22, which we will call the non-ambipolar loss term. The program solution is compared to the shorted array data. The agreement is again good for this combination of coeffients for values of the multipliers of less than 5. Similarly to the previous case, the non-ambipolar loss term can yield good agreement with the array unshorted case.

Fig. 6.5: The steady-state solution to the time dependent transport equation compared to the high pressure experimental density (upper curve),and temperature profiles. The data is unshorted strips, and ion-neutral scaling in K and $D_{\perp}$, with the ambipolar loss term. (FD/FC=3.75, FS/FC=.167)

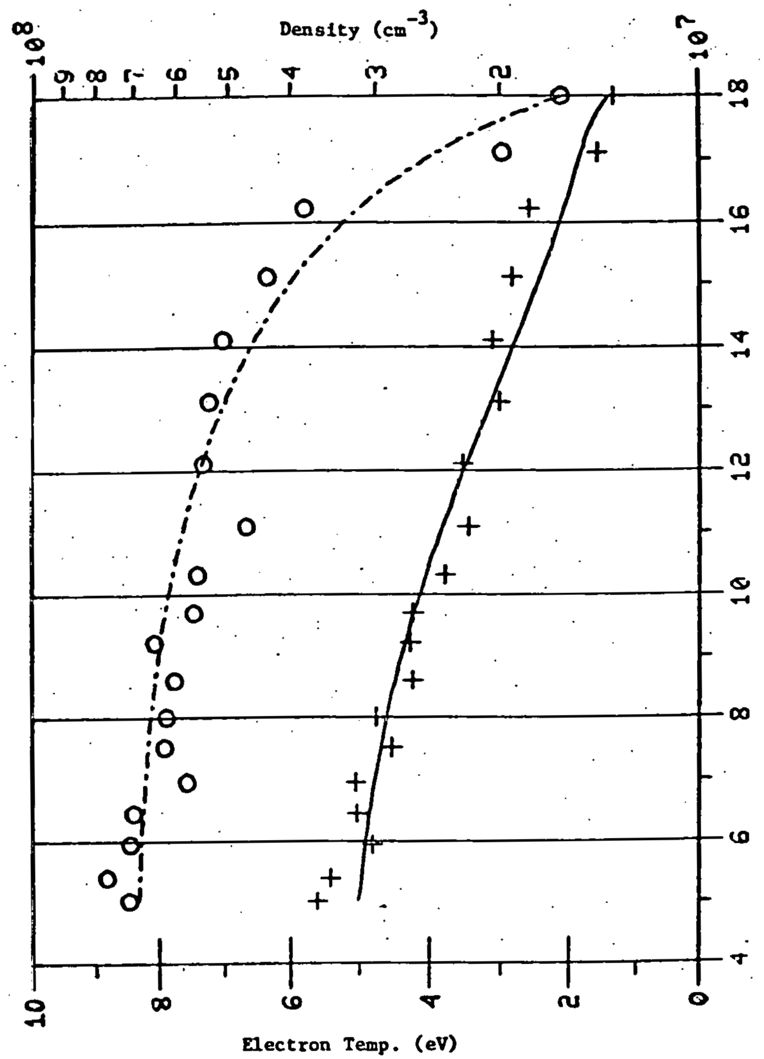

Fig. 6.6: The steady-state solution to the time dependent transport equation compared to the low pressure experimental density (upper curve), and temperature profiles. The data is unshorted strips, and ion-neutral scaling in K and $D_\perp$, with the ambipolar loss term. (FD/FC=.33, FS/FC=.67)

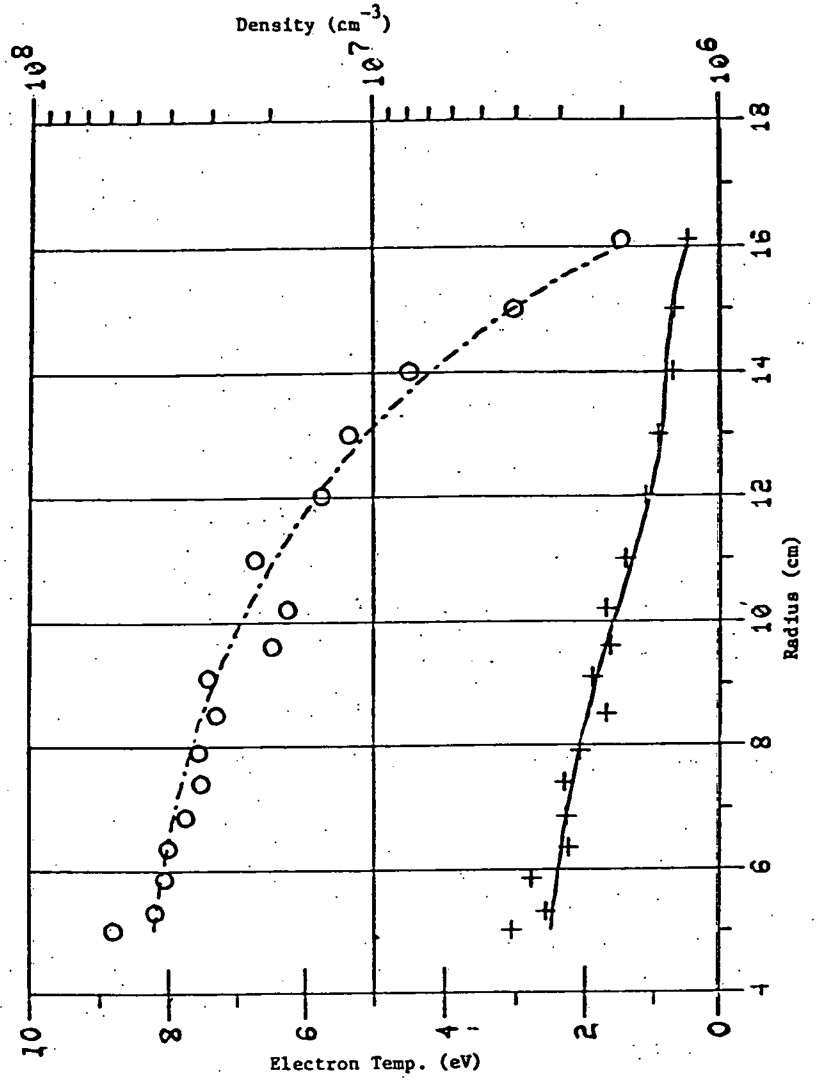

Fig. 6.7: The steady-state solution to the time dependent transport equation compared to the high pressure experimental density (upper curve), and temperature profiles. The data is for shorted strips, and ion-neutral scaling in K and $D_\perp$, with the ambipolar loss term. (FD/FC=.33, FS/FC=.167)

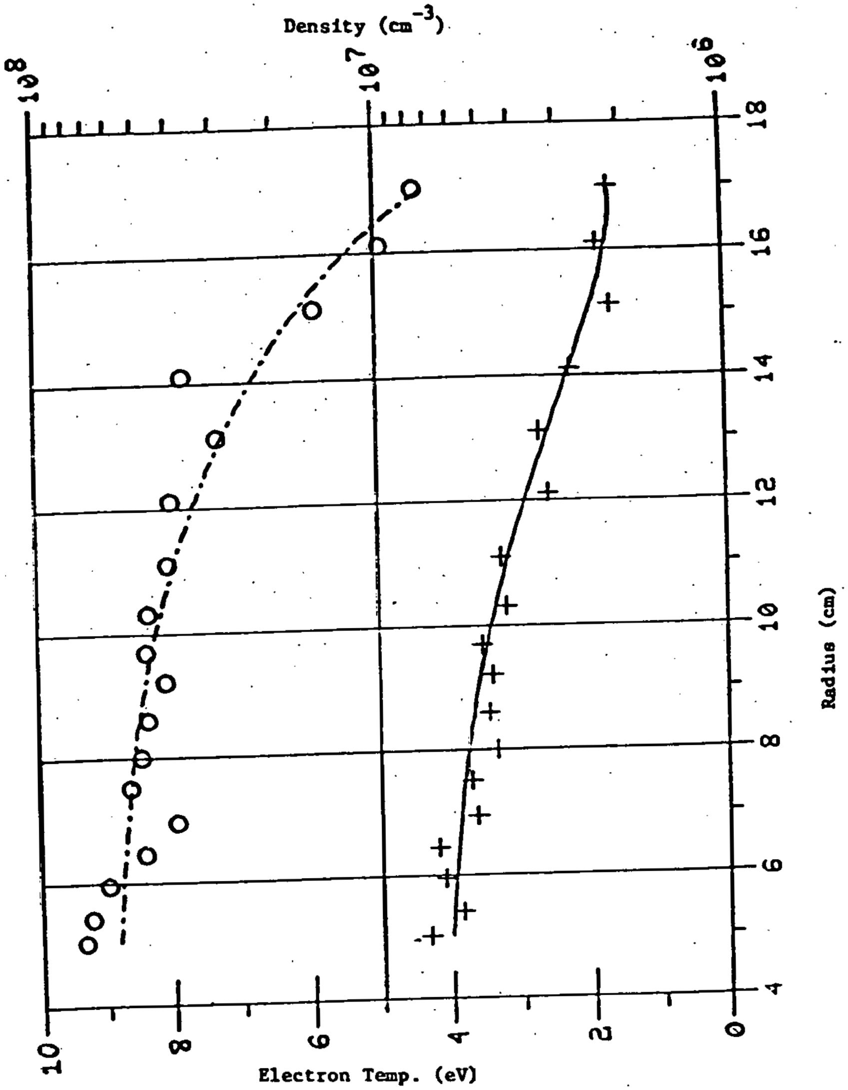

Fig. 6.8: The steady-state solution to the time dependent transport equation compared to the high pressure experimental density (upper curve), and temperature profiles. The data is shorted strips, ion-neutral scaling in K and $D_\perp$, and the non-ambipolar loss term. (FD/FC=.33, FSI/FC=.33, FSE/FC=.33)

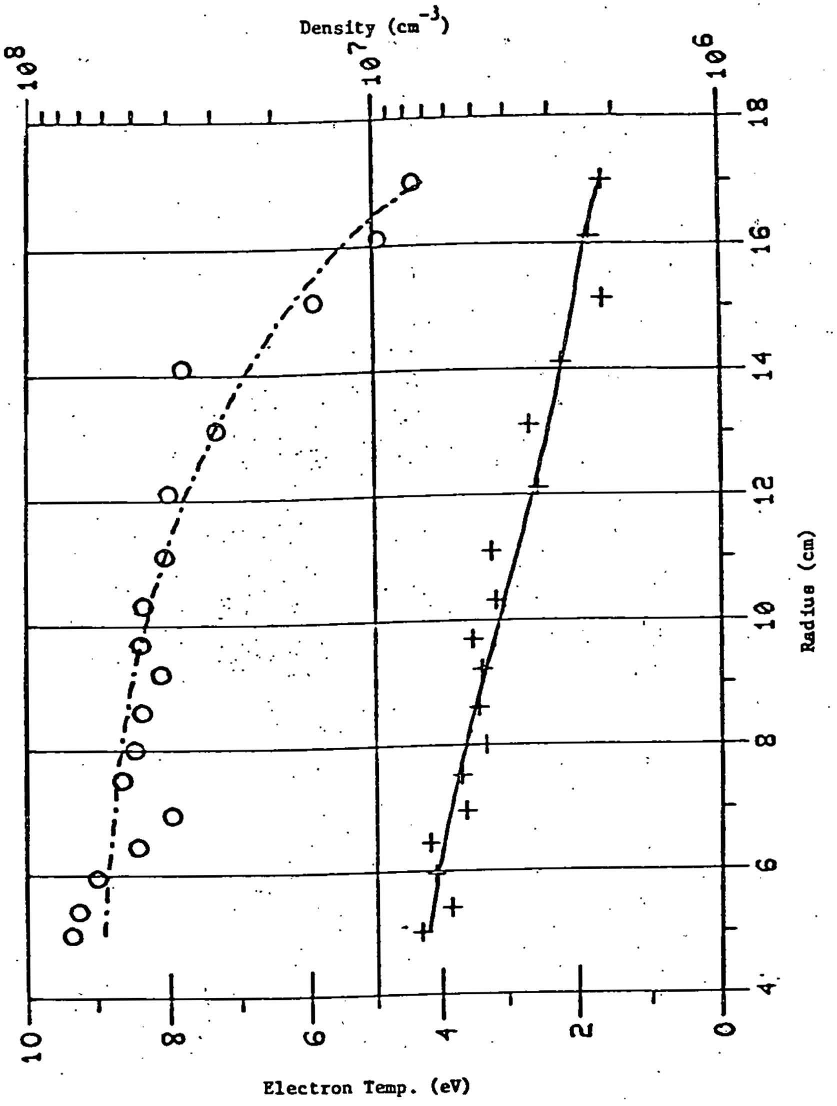

As a test of the extension of Simon's theory that was described earlier, scaling of the transport coefficients for electron-neutral dominated transport was inserted in the temperature equation, for both convection and conduction terms, with the parallel loss term chosen to be non-ambipolar. Good agreement for this case could only be obtained by multiplying the cross field thermal conductivity by a factor of 20, as shown in Fig. 6.9. The same effect could be obtained by "enhancing" the neutral density in the program by a factor of 12, as shown in Fig. 6.10. In all cases the electron scaling in the temperature equation seems to be too small.

If now only the convective part of the temperature equation has ion classical scaling as discussed, good agreement can again be obtained for reasonable multipliers (i.e. less than five) as is shown in Fig. 6.11. This scaling is also capable of yielding good agreement with all of the experimental profiles, except one taken at low source gas pressure. The program is subject to numerical instabilities for the boundary conditions (i.e. very low density) appropriate to this case. This is believed to be a result of our choice for handling the transport coefficients in the program, and not a failure of the model.

As a final example, the sheath potential drop was calculated self-consistently from the electron temperature, using the condition of ambipolarity at all radii. The program still converged to a steady state solution which, for appropriate coefficients, could be made to look like the experimental profiles when the ion classical scaling was used. This is shown in Fig. 6.12.

Fig. 6.9: The steady-state solution to the time dependent transport equation compared to the high pressure experimental density (upper curve), and temperature profiles. The data is for strips shorted, electron-neutral scaling in K and $D_{\perp}$, with the non-ambipolar loss term. (FD/FC=.05, FSI/FC=.05, FSE/FC=.05)

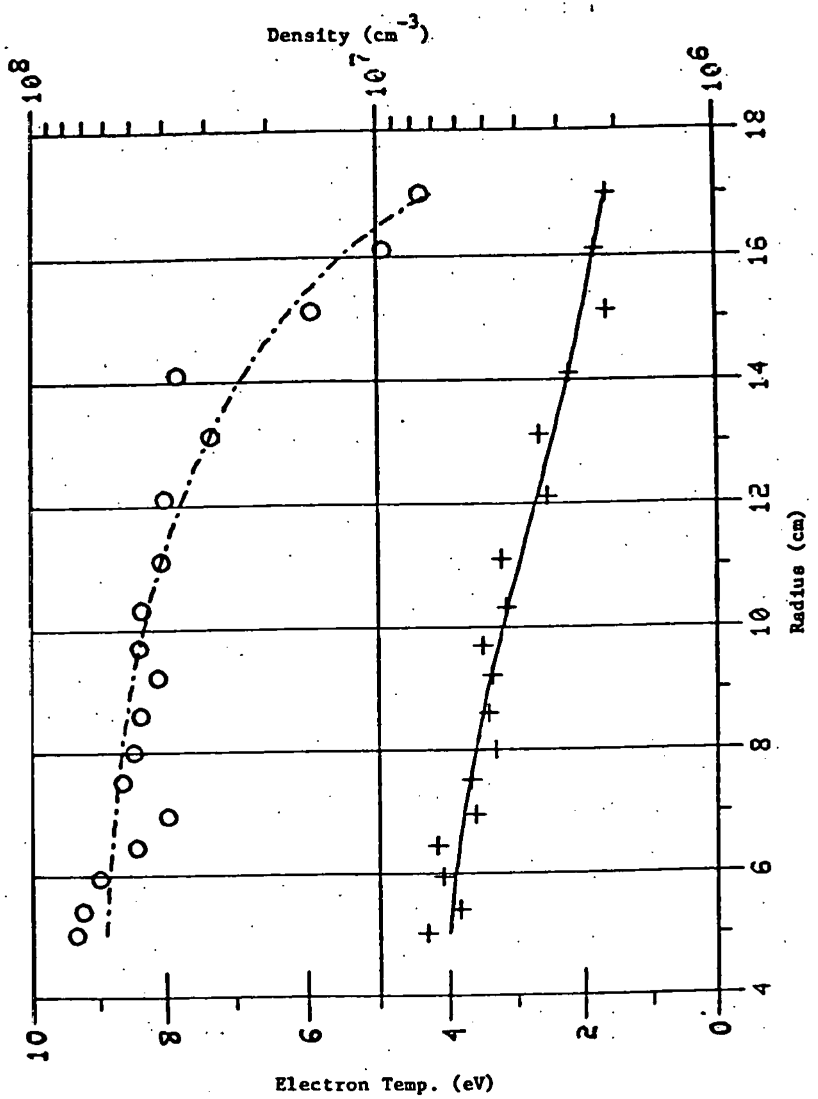

Fig. 6.10: The steady-state solution to the time dependent transport equation compared to the high pressure experimental density (upper curve), and temperature profiles. The data is for strips shorted, with electron-neutral scaling in K and $D_\perp$, and the non-ambipolar loss term. (All coefficients=1, neutral density a factor of 12 above the experimental neutral density.)

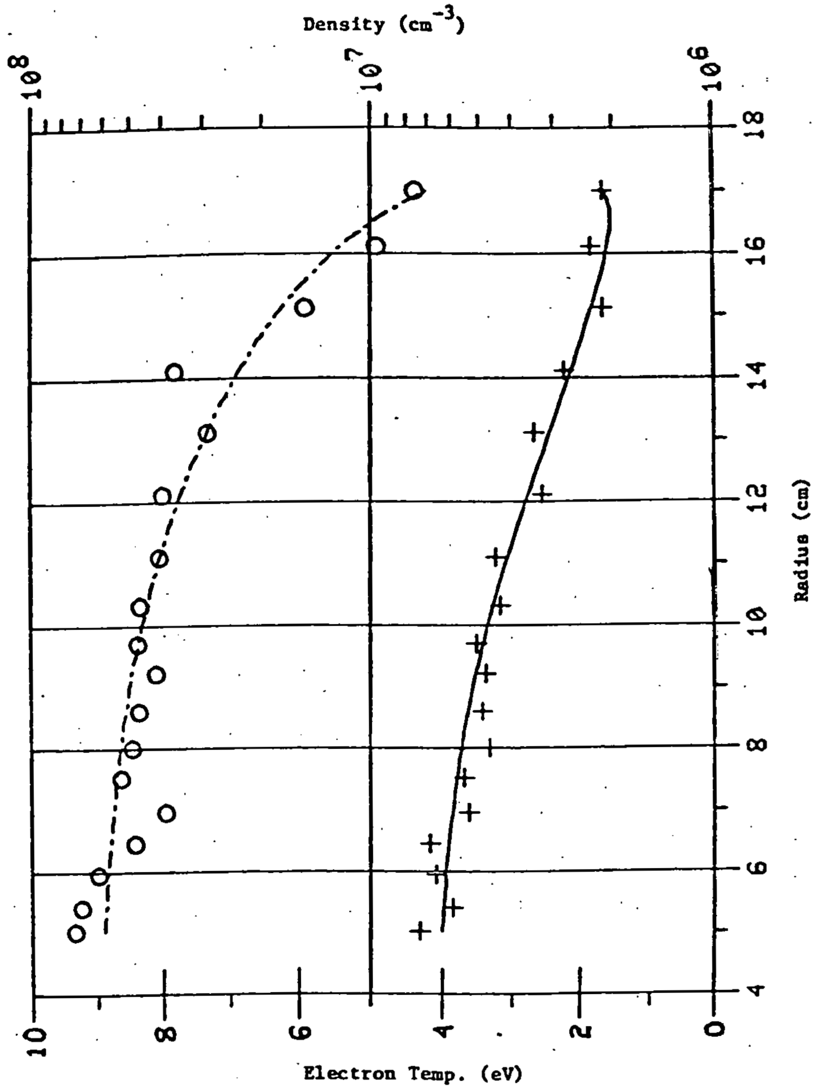

<u>Fig. 6.11</u>: The steady-state solution to the time dependent transport equation compared to the high pressure experimental density (upper curve), and temperature profiles. The data is for strips shorted, and ion-neutral scaling in $D_\perp$ and electron-neutral scaling in K, with the ambipolar loss term. (FD/FC=.86, FS/FC=.167)

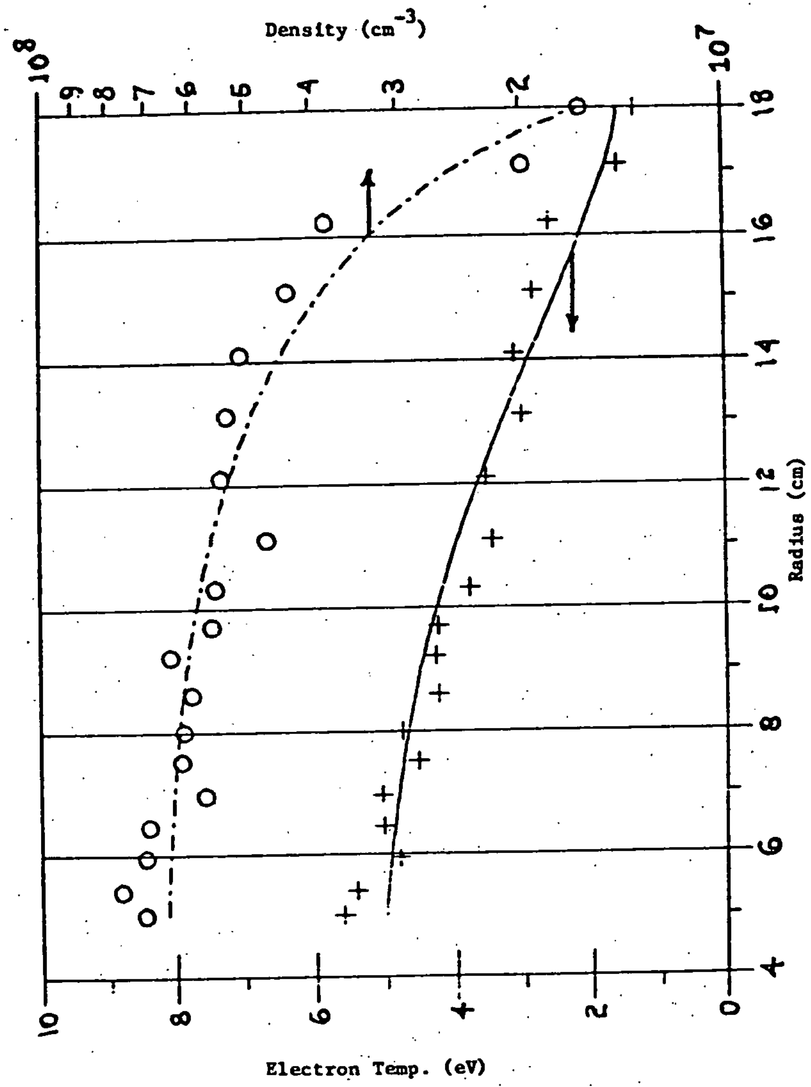

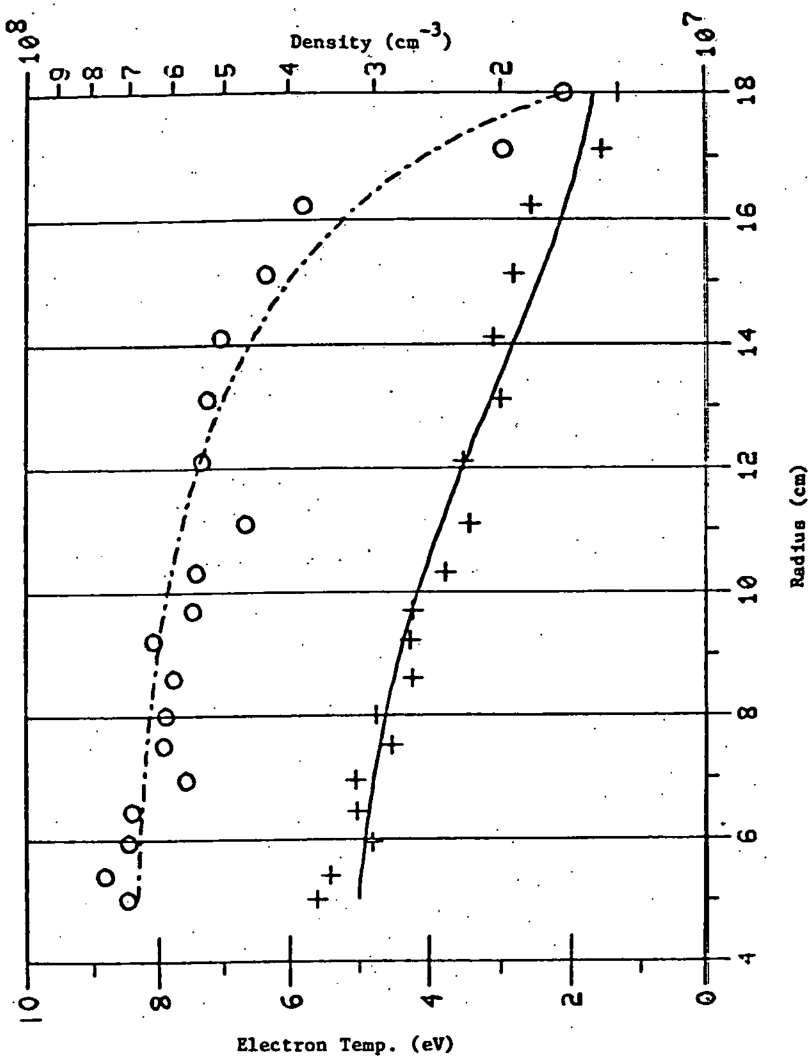

Fig. 6.12: The steady-state solution to the time dependent transport equation compared to the high pressure experimental density (upper curve), and temperature profiles. The data is for strips unshorted, ion-neutral scaling in K and $D_\perp$, with the ambipolar loss term, where $e\phi = \alpha T_e$ at all points. (FD/FC=.5, FS/FC=.167)

In conclusion, it seems that the correct scaling for the cross field diffusion coefficient in the density equation and the convective part of the cross field energy transport is the ion classical value. Electron classical scaling works well in the conduction term. This choice of transport coefficients is supported by the existence of a coupling electric field between the ions and the electrons. Electron scaling in the temperature equation is far too small. Both forms of the energy loss term are capable of yielding good agreement with the experimental data for reasonable values of the multiplicative factors. Unfortunately this also makes it difficult to choose between the loss terms. However, it does seem clear that the one dimensional flow model is acceptable for describing the transport in a divertor, at least within the context of the parameter range of our experiment.

References-Chapter 6

1. A.T. Mense, G.A. Emmert, Nuc. Fus. 19, 361 (1979).
2. A.H. Boozer, Phys. Fluids 19, 1210 (1976).
3. M.C. Zarnstorff, J.R. Greenwood, University of Wisconsin Dept. of Physics P.L.P. 662, (1973).
4. D. Meade, R. Fonck, Phys. Fluids 16, 1645 (1973).
5. A.T. Mense, University of Wisconsin Dept. of Nuclear Engineering, Ph.D. Thesis (1977).
6. F. Reif, "Fundamentals of Statistical and Thermal Physics", McGraw Hill Book Co., New York, Chap. 12 (1965).
7. R.L. Freeman, E.M. Jones, "Atomic Collision Processes in Plasma Physics Experiments", Culham Lab. Report CLM-R137, Culham Lab., Abingdon Berkshire, England (1974).
8. J.R. Patau, University of Wisconsin Dept. of Physics P.L.P. 558, (1974).
9. W.A. Houlberg, R.W. Conn, Nuclear Science and Engineering 64, 141 (1977).
10. W.E. Milne, "Numerical Solution to Differential Equations", New York, Wiley (1953).
11. F.S. Acton, "Numerical Methods That Work", New York, Harper and Row, Chap. 16 (1970).

Chapter 7

Summary and Conclusions

Certain of the physical phenomena that will occur in a tokamak divertor have been simulated in the divertor experiments carried out in the D.C. machine. The density and electron temperature show an anticipated fall off with radius due to the particle and energy sink that the divertor plate provides, in comparison with the profiles before the plate was installed. On those field lines that do intersect the conducting divertor plate, we have observed by a variety of means that the transport along the magnetic field, and thus also across the magnetic field, is non-ambipolar. This is contrary to the assumption of ambipolarity in most theoretical divertor models. We further expect the phenomena of non-ambipolar flow to exist is a real tokamak divertor if the cross field transport is dominated by charged particle-neutral collisions. Divertor plasma parameters and neutral pressures in present day experiments are, except for higher ion temperatures, not unlike those in our experiment. Therefore, non-ambipolar transport may exist in them. Expected conditions in future tokamak divertors may also allow the existence of non-ambipolar transport.

We observe a variation in the parameter η ($\eta = e\phi_s/kT_e$ where ϕ_s is the experimentally measured sheath potential drop and T_e the electron temperature at the same point) that causes the electrons to leave the plasma over a narrow width near the divertor plate edge, and the ions over a much broader width. This can strongly affect the heat loading distribution on the divertor plate, causing an electron "hot spot" where the electrons hit the plate.

By mounting a radially segmented array on the divertor plate, we tried to remove the non-ambipolar flow by isolating each segment electrically from the rest of the segments. In effect each segment was allowed to electrically "float" to its own local potential. Our attempts to force ambipolarity were only partially successful, although the mechanism that allows shorting in the floating array case is not clear. An interesting extension of this research would answer the question of the existence of non-ambipolar flow in a fully ionized plasma. Furthermore, understanding the physical mechanism that allows some shorting between array strips when the external short is removed could be relevant to the transport in all devices that have magnetic field lines that terminate on a wall. If it does prove advantageous to be able to eliminate the effects of non-ambipolar flow entirely, the mechanism of this shorting must be better understood.

Our efforts to measure the plasma flow velocity along the magnetic field and into the divertor plate met only with a measure of success. By placing a striped particle collector on the divertor plate to measure $\Gamma_{\parallel}$, the particle flux incident on the plate, and dividing by n, the density measured at the same point, we hoped to get the plasma flow velocity. Within large error bars, the flow velocity does seem to be always near the ion acoustic velocity. The behaviour of the striped particle collector when the magnetic field is perpendicular to the stripes is another potential area of research if it is to be of diagnostic utility in a situation such as ours.

The theories of Boozer and Simon predict ion density fall off scale lengths across the field that agree quite well with the measured local ion density scale length. Boozer's scale length seems to be a factor of two too large, and Simon's scale length a factor of three too small.

The numerical solutions to the transport equations are very close to the observed experimental profiles for the correct choice of transport coefficients. Ion classical scaling (i.e. due to ion-neutral collisions) works best for $D_\perp$ in the particle equation and the convective term in the energy equation. The thermal conductivity characteristic of electron-neutral collisions seems to be the correct one for our experiment. The fact that ion classical scaling works best in the convective term means that the divertor plate doesn't completely "short out" the ambipolar electric field, and thus the electron and ion transport are still coupled through this field. The ambipolar and non-ambipolar loss terms work equally well in the transport equations. Despite these successes, the change in the scaling of the transport from the shorted array case to the unshorted case is not clear. Further study of all the mechanisms that could explain the observed change that removing the short has on the profiles, is also indicated for extensions of this work. However, the flow model does seem to be appropriate for our divertor experiment, over the whole of its operating range.

EXTERNAL DISTRIBUTION IN ADDITION TO UC-20

R.W. Conn, University of California, Los Angeles
J.W. Flowers, University of Florida
H.S. Robertson, University of Miami, FL
M. Kristiansen, Texas Technical University
Plasma Research Laboratory, Australian National University
P.E. Vandenplas, Association Euratom-Etat Belge, Belgium
P. Sananaka, Institute de Fisica-Unicamp, Brazil
A.M. Dupas, C.E.N.G., Dph-PFG-SIG, France
M.A. Loyau, Centre d'Etudes Nucleaires, France
G. VonGierke, Max-Planck-Institut Für Plasma Physic, Germany
R. Toschi, Associazione Euratom-Cnen Sulla Fusion, Cento Gas Ionizzati, Italy
K. Takayma, IPP Nagoy Imoversotu, Japan
K. Uo, Kyote University, Japan
K. Yamanto, JAERI, Japan
B. Lehnert, Royal Institute of Technology, Sweden
E.S. Weibel, CRPP, Ecole Polytechnique Federale de Lausanne, Switzerland
A. Gibson, Culham Laboratory, UK
R.S. Pease, Culham Laboratory, UK
D.R. Sweetman, Culham Laboratory, UK
J.B. Taylor, Culham Laboratory, UK
M.H. Hellberg, University of Natal, Durban, South Africa
Cheng-chung Yang, Chinese Academy of Sciences, Lanchow, Peoples Republic of China
Chi-shis Li, Chinese Academy of Sciences, Peking, Peoples Republic of China
Hsiao-wu Chěng, Chinese Academy of Sciences, Shanghai, Peoples Republic of China
Yi-chung Cho, Chinese Academy of Sciences, Peking, Peoples Republic of China
Fu-chia Yang, Futan University, Peoples Republic of China
Mei-ling Yeh, Chinese Academy of Sciences, Lanchow, Peoples Republic of China
Wei-chung Change, Chinese Academy of Sciences, Shanghai, Peoples Republic of China
Kuei-wu Wang, Chinese Academy of Sciences, Loshan County, Peoples Republic of China
Chŭn-hsien Chěn, Chinese Academy of Sciences, Peking, Peoples Republic of China
Li-tsien Chiu, Chinese Academy of Sciences, Peking, Peoples Republic of China
Miao-sun Chen, Chinese Academy of Sciences, Peking, Peoples Republic of China

6 for Chicago Operations Office
10 for individuals in Washington Offices

INTERNAL DISTRIBUTION IN ADDITION TO UC-20

100 for local group and file